

INVESTIGATING THE EFFECTS OF RbF POST-DEPOSITION TREATMENTS IN $\text{Cu}(\text{In}_x\text{Ga}_{1-x})\text{Se}_2$
SOLAR CELLS

by
Jake W. Wands

© Copyright by Jake W. Wands, 2023

All Rights Reserved

A thesis submitted to the Faculty and the Board of Trustees of the Colorado School of Mines in partial fulfillment of the requirements for the degree of Doctor of Philosophy (Materials Science).

Golden, Colorado

Date _____

Signed: _____

Jake W. Wands

Signed: _____

Dr. Angus A. Rockett
Thesis Advisor

Golden, Colorado

Date _____

Signed: _____

Dr. Eric Toberer
Director of Materials Science Program
Department of Metallurgical and Materials Engineering

ABSTRACT

In order to meet global energy demand while reducing carbon emissions, large-scale deployment of renewable energy technologies is needed. Solar photovoltaics (PV) are a key technology and have become one of the cheapest options for new energy installations. $\text{Cu}(\text{In}_x\text{Ga}_{1-x})\text{Se}_2$ (CIGS) based PV is a thin-film technology with potential benefits over market-leading silicon. Alkali halide post-deposition treatments (PDTs) have become an essential tool in maximizing the efficiency of CIGS solar cells. While Na and K have received the most research as the alkali choice, Rb has been shown to further improve performance, largely through open-circuit voltage (V_{OC}) increases.

This thesis studies the effects of RbF based PDTs on the performance of CIGS solar cells. In all samples studied the RbF PDT increased V_{OC} over an untreated reference sample. Device modeling and temperature-dependent current-voltage (JVT) experiments found that reduced recombination and bandtail width may be key factors in V_{OC} improvements. An aging study also found a smaller decrease in V_{OC} after aging in the RbF PDT device compared to the reference.

Despite the benefits of RbF, there are still some drawbacks. After aging, the RbF PDT device experienced a larger decrease in short-circuit current and fill factor (FF). Additionally, the RbF PDT device suffered from larger voltage-dependent collection efficiency (η_C) losses. Low η_C led to large reductions in FF and maximum power. It is theorized that low depletion width and the Ga/(Ga+In) gradient near the heterojunction are contributors to low η_C .

Preliminary research on defect signatures suggests that the dominant trap state changes after RbF PDT. While the identity of the dominant defects is not known, this research identifies an important area of future research.

TABLE OF CONTENTS

ABSTRACT	iii
LIST OF FIGURES	vii
LIST OF TABLES	x
LIST OF SYMBOLS	xi
LIST OF ABBREVIATIONS	xiii
ACKNOWLEDGMENTS	xiv
DEDICATION	xv
CHAPTER 1 INTRODUCTION	1
1.1 Motivation	1
1.2 Thesis Outline	3
1.3 Relevant Publications	4
CHAPTER 2 BACKGROUND INFORMATION	7
2.1 P-N Junction Basics	7
2.2 Current in a Photovoltaic Device	9
2.3 Performance Characteristics of Solar Cells	10
2.4 Defects and Recombination	11
CHAPTER 3 $\text{Cu}(\text{In}_x\text{Ga}_{1-x})\text{Se}_2$ PHOTOVOLTAIC DEVICES	15
3.1 Material Structure	15
3.2 PV Device Structure	16
3.3 Effect of Alkali Metals	17
3.3.1 Light Alkalis	17
3.3.2 Rubidium	17
CHAPTER 4 EVALUATING RECOMBINATION MECHANISMS IN RbF TREATED $\text{Cu}(\text{In}_x\text{Ga}_{1-x})\text{Se}_2$ SOLAR CELLS	19
4.1 Abstract	19

4.2	Introduction	19
4.3	Experimental Methods	20
4.4	Measured Devices	22
4.5	Device Model	23
4.6	Results	24
4.7	Conclusion	28
4.8	Acknowledgment	29
4.9	Appendix	30
CHAPTER 5 STABILITY OF $\text{Cu}(\text{In}_x\text{Ga}_{1-x})\text{Se}_2$ SOLAR CELLS UTILIZING RbF POST-DEPOSITION TREATMENT UNDER A SULFUR ATMOSPHERE		33
5.1	Abstract	33
5.2	Introduction	33
5.3	Experimental Methods	34
5.4	Results and Discussion	35
5.5	Conclusion	43
5.6	Acknowledgements	44
5.7	Appendix	45
CHAPTER 6 VOLTAGE-DEPENDENT COLLECTION EFFICIENCY LOSSES IN RbF TREATED $\text{Cu}(\text{In}_x\text{Ga}_{1-x})\text{Se}_2$		49
6.1	Abstract	49
6.2	Introduction	49
6.3	Experimental Methods	50
6.4	Results and Discussion	51
6.5	Conclusions	58
6.6	Acknowledgments	58
CHAPTER 7 DEFECT ANALYSIS OF RbF BASED POST-DEPOSITION TREATMENTS IN $\text{Cu}(\text{In}_x\text{Ga}_{1-x})\text{Se}_2$ SOLAR CELLS		59
7.1	Introduction	59
7.2	Experimental Methods	60

7.3	Results and Discussion	61
7.4	Conclusions	64
CHAPTER 8 CONCLUSIONS		65
8.1	Conclusions	65
8.2	Future Work	65
REFERENCES		67
APPENDIX A AUTOMATED JVT ANALYSIS CODE		75
APPENDIX B COPYRIGHT PERMISSIONS		76
B.1	Figure 1.1 Copyright Permission	76
B.2	Figure 1.2 Copyright Permission	76
B.3	Chapter 4 Copyright Permission	77
B.4	Chapter 5 and 6 Copyright Permission	78

LIST OF FIGURES

Figure 1.1	Historical and projected energy consumption under three financial growth models. Projected consumption is split between Organization for Economic Cooperation and Development (OECD) and non-OECD countries and highlights the large growth expected as non-OECD countries develop their economies. Reprinted from the U.S. Energy Information Administration’s International Energy Outlook 2021.	1
Figure 1.2	Historical cost and adoption of select renewable energy technologies from 2000-2020. Massive declines in PV cost have contributed to increased adoption. Note that PV costs are now at or below the cost of fossil fuel energy sources. Reprinted from the International Panel on Climate Change’s Sixth Assessment Report.	2
Figure 2.1	Equivalent circuit diagram of a solar cell including the parasitic series and shunt resistances.	10
Figure 2.2	Comparison of dark and light JV curves in an ideal solar cell.	11
Figure 2.3	Band diagram depicting midgap and bandtail states existing within the bandgap. A density of states sketch is included to display the exponential decay of states which leads to bandtails.	12
Figure 2.4	Sketch showing how midgap defects lead to Shockley-Read-Hall recombination in a solar cell.	14
Figure 3.1	Unit cell for the CIGS absorber material. Cu is shown in blue, Se in light green, and the group III elements, In and Ga, occupy the same lattice sites and are depicted by spheres which are split between dark green and pink.	15
Figure 3.2	Structural diagram of a typical CIGS solar cell such as those presented in the following chapters.	16
Figure 4.1	Simulated and experimental plots of $J-J_{SC}$ as a function of voltage for the as-deposited and RbF PDT samples. The scatter in the experimental (dotted) data is due to experimental noise near J_{SC}	23
Figure 4.2	SCAPS simulations of V_{OC} as a function of defect concentration for a) as-deposited (shown in red) and b) RbF PDT (shown in blue) samples. Simulated defects include point defects at $E_V+0.58eV$ (circles) and $E_V+0.98eV$ (triangles) as well as bandtails (squares). The dotted lines represent the experimentally measured V_{OC} for each device. The black circles and triangles indicate the experimental values of the $E_V+0.58eV$ and $E_V+0.98eV$ defects respectively.	24
Figure 4.3	SCAPS simulations of V_{OC} as a function of bandtail characteristic energy for as-deposited (red) and RbF PDT (blue) devices.	25
Figure 4.4	TRPL measurements demonstrating the increased lifetime of the RbF PDT sample (blue) compared to the as-deposited sample (red).	26
Figure 4.5	V_{OC} vs temperature plots with linear extrapolation to 0 K. The linear extrapolations are taken from the linear region above 230 K.	27

Figure 4.6	J_0 as a function of temperature highlighting the decrease in recombination after RbF PDT.	28
Figure 4.7	Inverse ideality factor vs temperature with the tunneling enhanced recombination model represented by the solid lines. The dotted lines represent the same model with the effect of tunneling removed to highlight the impact of tunneling on recombination.	29
Figure 4.8	TOF-SIMS depth profiles for the as-deposited sample. O+ and Mo+ signals are included to provide boundaries for the absorber layer. Notice the two Ga isotopes track each other closely.	31
Figure 4.9	TOF-SIMS depth profiles for the RbF PDT sample. The Rb isotopes track each other well and have a different shape than the Ga signal. This indicates that the signal truly is Rb and not the possible GaO mass interference.	32
Figure 4.10	Comparison of the TOF-SIMS profiles for the as-deposited (red) and RbF PDT (blue) samples. Na appears to be partially displaced by Rb near the junction while K is relatively untouched.	32
Figure 5.1	EQE measurements show reduction at low energies (Ref) and high energies (RbS PDT), respectively after aging.	36
Figure 5.2	Semi-log JV curves measured at a) 200 K and b) 300 K for each device before and after aging.	37
Figure 5.3	a) Equivalent circuit diagram depicting the reverse polarity rear diode and b) JV curves for the reverse polarity back diode in the aged devices at 200 K.	38
Figure 5.4	Ideality factor as a function of temperature for each device.	39
Figure 5.5	Arrhenius plot of $n \cdot \ln(J_0/J_{00})$ vs $1/kT$ with linear fits to the data. The activation energy is calculated from the slope of the fit (dashed lines).	40
Figure 5.6	Modified Arrhenius plot to determine whether ideality factor is the only temperature-dependent variable. The slope of the linear fits results in activation energies that don't match those of Figure 5.5.	41
Figure 5.7	Arrhenius plot using the temperature-dependent activation energy model. Activation energies calculated from the slope of the linear fits agree well with Figure 5.5.	42
Figure 5.8	Comparison of experimental data (dots) with modeled (dashed lines) J_0 vs T plots using Eq. 9 and data from Table 5.2. The modeled data agrees well with experimental results.	43
Figure 5.9	V_{OC} vs T plots with linear extrapolation to 0 K to calculate the activation energy. Linear fits were applied to data above 250 K to account for the low-temperature roll-over effect.	44
Figure 5.10	Example dV/dJ curve for the Ref device at 300 K. The highlighted portion of the curve is the linear region which was fit to produce the dV/dJ behavior of the main diode.	45
Figure 5.11	Dark JVT curves from 180 K to 350 K for the a) fresh Ref, b) aged Ref, c) fresh RbS PDT, and d) aged RbS PDT devices.	46

Figure 5.12	Voltage split between the main diode and the reverse polarity back diode for each aged device.	46
Figure 5.13	TOF-SIMS depth profiles for the Ref device. All measurements used a 1 keV Cs sputter beam was used at 90 nA of current along with a 30 keV Bi ₃ primary beam run at 0.7 pA.	47
Figure 5.14	TOF-SIMS depth profiles for the RbS PDT device.	47
Figure 5.15	TOF-SIMS comparison of alkali elements between the two devices. There is a noticeable drop in Na ⁺ and K ⁺ signal in the RbS PDT sample suggesting that Rb is reducing the concentration of other alkalis.	48
Figure 6.1	Illuminated and J _{dark} -J _{SC} JV curves for the RbS PDT device demonstrates that the superposition principle is not followed. Noise is present in the illuminated curve although it does not affect the following analysis.	52
Figure 6.2	Voltage-dependent collection efficiency (η_C) as a function of junction voltage (V').	53
Figure 6.3	Measured and corrected JV curves for the a) Ref, b) RbS PDT, and c) RIS PDT devices.	54
Figure 6.4	Measured and corrected power vs voltage curves for the a) Ref, b) RbS PDT, and c) RIS PDT devices.	55
Figure 6.5	TRPL decay curves for each device displaying increased lifetime after PDT.	56
Figure 6.6	TOF-SIMS depth profiles showing the relative difference in GGI ratio within the CIGS absorber layer.	57
Figure 6.7	Variable C-V measurements providing a) carrier concentration vs depletion width and b) depletion width vs voltage for each device.	57
Figure 7.1	Exponential decay curves for capacitance transients featuring majority carrier emission (solid line) and minority carrier emission (dotted line). $t=0$ represents the point when the sample is put into reverse bias and the traps begin to depopulate. This figure is inspired by Fig. 5.8 in	60
Figure 7.2	TPC spectra normalized to the intensity at 1.30 eV. A defect centered at 0.8 eV is present in all samples with reduced intensity in the RbF PDT samples.	61
Figure 7.3	Dark (left) and light (right) capacitance transients for each sample. 1.30 eV light was used in the illuminated transients.	62
Figure 7.4	DLTS spectra for a) Ref, b) RbS PDT, and c) RIS PDT at rate windows from 1.9 Hz to 25.5 Hz. The arrows indicate increasing rate window frequency. The PDT samples show the formation of a possible shoulder peak at high frequencies.	63
Figure 7.5	Arrhenius plots calculating the activation energy of the DLTS peaks. The activation energies are higher than typical DLTS measurements and may indicate non-ideal behavior.	64

LIST OF TABLES

Table 4.1	Summary of experimental and SCAPS model device parameters at 300 K	22
Table 4.2	SCAPS parameters used to simulate the reference devices.	30
Table 4.3	SCAPS parameters used to simulate the RbF PDT devices.	30
Table 4.4	Additional SCAPS parameters. Values for the reference device are shown without parenthesis while RbF PDT values are within parenthesis.	31
Table 5.1	JV parameters, R_s , and its impact on FF before and after aging for each device.	35
Table 5.2	Calculated values from the temperature-dependent activation energy model.	42
Table 6.1	Device performance parameters for the measured and corrected JV curves. The change in V_{OC} , FF, and P_{max} after corrections is also included.	54

LIST OF SYMBOLS

Acceptor Concentration	N_A
Activation Energy	E_a
Applied Voltage	V_{applied}
Bandgap Energy	E_g
Boltzmann Constant	k_B
Built-In Voltage	V_{BI}
Cell Area	A
Characteristic Tunneling Energy	E_{00}
Conduction Band Energy	E_C
Current Density at Maximum Power	J_{mp}
Dielectric Constant	<i>epsilon</i>
Dielectric Thickness	d
Diode Activation Energy Temperature Coefficient	α
Donor Concentration	N_D
Electron Concentration in p-type Semiconductor	p_n
Electron Diffusion Length	L_n
Electron Diffusivity	D_n
Electron Quasi-Fermi Energy	E_{Fn}
Electronic Charge	q
Fermi Energy	E_F
Fill Factor	FF
Hole Concentration in n-type Semiconductor	n_p
Hole Diffusion Length	L_p
Hole Diffusivity	D_p
Hole Quasi-Fermi Energy	E_{Fp}

Ideality Factor	n
Intrinsic Carrier Concentration	n_i
Minority Carrier Lifetime	τ
Open-Circuit Voltage	V_{OC}
Photocurrent	J_L
Power Conversion Efficiency	η
Reverse Saturation Current Density	J_0
Reverse Saturation Current Sensity Prefactor	J_{00}
Series Resistance	R_S
Short-Circuit Current Density	J_{SC}
Shunt Resistance	R_{SH}
Temperature	T
Trap Energy	E_t
Valence Band Energy	E_V
Voltage at Maximum Power	V_{mp}
Voltage-Dependent Collection Efficiency	η_C

LIST OF ABBREVIATIONS

Zentrum für Sonnenenergie- und Wasserstoff-Forschung Baden-Württemberg	ZSW
Cadmium Sulfide	CdS
Capacitance-Voltage	CV
$\text{Cu}(\text{In}_x\text{Ga}_{1-x})\text{Se}_2$	CIGS
CuInSe_2	CIS
Current-Voltage	JV
Deep-Level Optical Spectroscopy	DLOS
Deep-Level Transient Spectroscopy	DLTS
External Quantum Efficiency	EQE
$\text{Ga}/(\text{Ga}+\text{In})$	GGI
Levelized Cost of Electricity	LCOE
Photovoltaic	PV
Post-Deposition Treatment	PDT
Rubidium Fluoride	RbF
Shockley-Read-Hall	SRH
Soda-Lime Glass	SLG
Solar cell CAPacitance Simulator	SCAPS
Temperature-Dependent Current-Voltage	JVT
Time Resolved Photoluminescence	TRPL
Time-of-Flight Secondary Ion Mass Spectroscopy	TOF-SIMS
Transient Photocapacitance	TPC

ACKNOWLEDGMENTS

I would like to thank my advisor, Dr. Angus Rockett, for his advice and guidance throughout this process. It would be difficult to find a better source of knowledge than the person who wrote the book on the Materials Science of Semiconductors.

Thank you to my committee, Dr. Colin Wolden, Dr. Brian Gorman, and Dr. David Diercks for your help and advice along the way.

I would like to thank the collaborators who have assisted me over the years. The teams at The Ohio State University, Université de Nantes, Zentrum fuer Sonnenenergie- und Wasserstoff-Forschung Baden-Wuerttemberg, and the National Renewable Energy Laboratory were essential to my success. I especially appreciate the help of Mr. Michael Walker, Dr. Alex Bothwell, Dr. Ryan France, and Dr. Steve Johnston who went out of their way to provide advice and mentorship.

I would also like to thank my friends and family. I can't state enough how much their help and support along the way meant to me. Most of all I would like to thank Laura. Without your support I would not have stayed until the end.

To everyone working to create a more sustainable society for future generations.

CHAPTER 1
INTRODUCTION

This chapter outlines the motivation for the work presented in this thesis. It also includes an outline and summary of the following chapters along with a list of relevant publications produced over the course of this PhD.

1.1 Motivation

According to the Energy Information Administration, global energy demand in 2050 will exceed 2020 levels by 47% [1]. As seen in Figure 1.1, of the 886 quadrillion BTU total projected energy demand, 618 quadrillion BTU is predicted to be supplied by fossil fuel resources in the reference scenario [1]. The result is a continued rise in atmospheric greenhouse gas emissions without massive intervention [2].

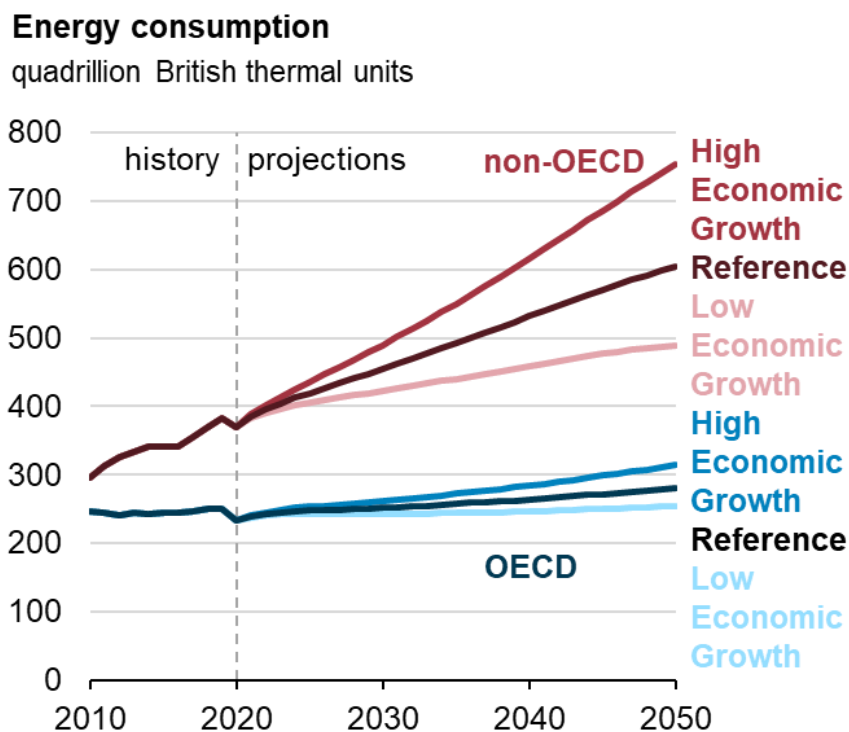


Figure 1.1 Historical and projected energy consumption under three financial growth models. Projected consumption is split between Organization for Economic Cooperation and Development (OECD) and non-OECD countries and highlights the large growth expected as non-OECD countries develop their economies. Reprinted from the U.S. Energy Information Administration’s International Energy Outlook 2021.

In the past decade several renewable energy technologies have seen dramatic cost reductions to become competitive with traditional fossil fuel resources. From 2010-2019 solar energy costs have decreased 85% [3], while wind and battery costs have decreased 55% and 85% respectively (Figure 1.2) [4]. The levelized cost of electricity (LCOE) for both solar and wind energy is now below that of coal and gas power sources [5]. This occurred in conjunction with a >10x increase in solar energy capacity, a >3x increase in wind energy capacity, and a >100x increase in electric vehicles [4].

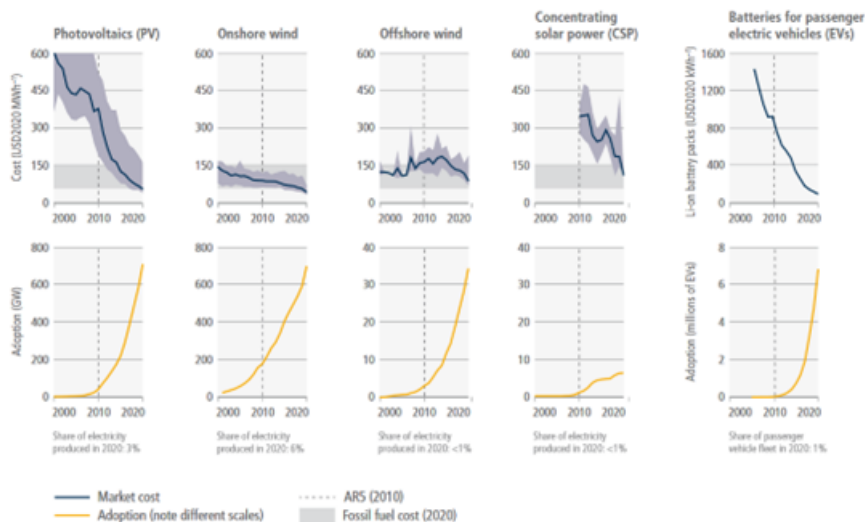


Figure 1.2 Historical cost and adoption of select renewable energy technologies from 2000-2020. Massive declines in PV cost have contributed to increased adoption. Note that PV costs are now at or below the cost of fossil fuel energy sources. Reprinted from the International Panel on Climate Change’s Sixth Assessment Report.

The most readily available energy source on Earth is the solar radiation which arrives free of charge each day. 173,000 TW of energy is continuously hitting the Earth which amounts to 10,000 times the total world energy use [6]. While there are several methods of capturing this energy for use in society, solar photovoltaics (PV) have emerged as the leading technology. Extensive research and development led silicon to dominate the PV market with high efficiency and low costs [7]. Economies of scale have played a large role in driving down the cost of silicon PV, and helped maintain its place as the market leader. However, thin-film photovoltaics have the potential to compete with silicon due to high-throughput manufacturing techniques and lower material requirements.

One of the leading thin-film technologies is based on the $\text{Cu}(\text{In}_x\text{Ga}_{1-x})\text{Se}_2$ (CIGS) chemistry [7]. Thin-film PV based on CIGS has achieved a champion small device efficiency of 23.4% which is among the highest for single-junction devices [8]. CIGS can also be produced using vapor transport methods with roll-to-roll manufacturing offering significant cost saving potential [9]. Another benefit of CIGS over silicon

is the high absorption coefficient which requires much less active material to collect light, leading to another potential reduction in cost [10]. Despite these benefits, CIGS has had relatively little market share to this point. CIGS modules perform well below the theoretical limit and the efficiency can vary significantly when manufacturing large quantities.

1.2 Thesis Outline

The goal of this thesis is to identify loss mechanisms in CIGS solar cells, and to provide steps for mitigating those losses. A specific focus is placed on how RbF post-deposition treatments (PDTs) impact device performance and stability. RbF PDTs have become a promising method of improving CIGS devices, largely by increasing open-circuit voltage (V_{OC}) [1], [2]. Despite the potential benefits of RbF, there is still debate about the mechanisms by which it improves performance. This thesis aims to shed light on how RbF benefits CIGS, as well as the ways in which it may harm solar cell efficiency.

In Chapter 4, the 1-D simulation software SCAPS is combined with temperature-dependent current-voltage (JVT) characterization to investigate defect and recombination mechanisms in RbF treated CIGS. Modeling results predict that two commonly detected defect levels, along with bandtails, can have a strong influence on V_{OC} . JVT measurements suggest that tunneling enhanced recombination via bandtail states is a dominant loss mechanism. The RbF PDT reduced the bandtail width which may contribute to the improvement in V_{OC} .

Chapter 5 utilizes JVT measurements to investigate a unique RbF PDT technique performed in a sulfur atmosphere rather than the typical selenium atmosphere. The stability of the samples was also tested by comparing measurements of fresh samples with those taken after six months in a desiccator. The PDT improved V_{OC} , however the FF suffered from series resistance losses. A reference sample and the RbF+S PDT both developed a blocking contact after aging which limits device performance. A temperature-dependent diode activation energy model was found to fit the data more appropriately than commonly used techniques. Activation energies for both samples suggest that Shockley-Read-Hall (SRH) recombination in the bulk absorber is the dominant loss mechanism.

Voltage-dependent collection efficiency was compared between a reference, a RbF+S PDT, and a RbF+In+S PDT in Chapter 6. Again the V_{OC} was found to improve after PDT, but lower collection efficiency led to higher FF losses. Several potential sources of low voltage-dependent collection efficiency were investigated. The Ga/(Ga+In) gradient near the heterojunction may be a contributing factor and poses a trade off between collection efficiency and interface recombination. Low depletion width in the PDT devices fit the results most closely and may explain the large loss in maximum power.

Finally, in Chapter 7 preliminary defect characterization results are presented on the same sample set used in Chapter 6. Transient photocapacitance (TPC) and deep-level transient spectroscopy (DLTS) were used to measure defect behavior. An $E_V+0.8$ eV defect level was identified in the TPC spectra for all samples, although the concentration was reduced after PDT. A closer look at the capacitance transients revealed that the trap type transitioned from majority carrier to minority carrier after PDT. DLTS spectra produced trap levels that should not be possible based on DLTS theory. It is hypothesized that non-exponential transients violate key assumptions, although the source of this behavior is not identified. This work highlights the difficulty of acquiring high quality data in polycrystalline CIGS.

1.3 Relevant Publications

The following is a list of relevant lead authored and co-authored publications produced during this thesis.

Evaluating Recombination Mechanisms in RbF Treated $Cu(In_xGa_{1-x})Se_2$ Solar Cells

J. Wands, A. Kanevce, A. Bothwell, M. Miller, S. Paetel, A. Arehart, A. Rockett, "Evaluating Recombination Mechanisms in RbF Treated $Cu(In_xGa_{1-x})Se_2$ Solar Cells," IEEE J. Photovolt., pp. 1–6, 2022, doi: 10.1109/JPHOTOV.2022.3197926.

Contributions: Performed temperature-dependent current-voltage experiments, data analysis, model development, document writing, interpretation and development of conclusions.

Stability of $Cu(In_xGa_{1-x})Se_2$ Solar Cells Utilizing RbF Post-Deposition Treatment Under a Sulfur Atmosphere

J. Wands, A. Bothwell, P. Tsoulka, T. Lepetit, N. Barreau, A. Rockett, "Stability of $Cu(In_xGa_{1-x})Se_2$ Solar Cells Utilizing RbF Post-Deposition Treatment Under a Sulfur Atmosphere," Advanced Energy and Sustainability Research, Submitted.

Contributions: Performed temperature-dependent current-voltage experiments, data analysis, model development, document writing, interpretation and development of conclusions.

Voltage-Dependent Collection Efficiency Losses in RbF Treated $Cu(In_xGa_{1-x})Se_2$

J. Wands, A. Bothwell, P. Tsoulka, T. Lepetit, N. Barreau, A. Rockett, "Voltage-Dependent Collection Efficiency Losses in RbF Treated $Cu(In_xGa_{1-x})Se_2$," Progress in Photovoltaics: Research and Applications, Submitted.

Contributions: Performed current-voltage experiments, capacitance-voltage experiments, data analysis, document writing, interpretation and development of conclusions.

Investigation of the Electrical Properties of Grain Boundaries in $(Ag_xCu_{1-x})(In_yGa_{1-y})Se_2$

J. Wands, S. Soltanmohammad, W. Shafarman, and A. Rockett, "Investigation of the Electrical Properties of Grain Boundaries in $(\text{Ag}_x\text{Cu}_{1-x})(\text{In}_y\text{Ga}_{1-y})\text{Se}_2$," in 2019 IEEE 46th Photovoltaic Specialists Conference (PVSC), Jun. 2019, pp. 0962–0964. doi: 10.1109/PVSC40753.2019.8981173.

Contributions: Performed scanning microwave impedance spectroscopy experiments, data analysis, document writing, interpretation and development of conclusions.

Effects of Novel In + RbF Post-Deposition Treatment on $\text{Cu}(\text{In}_x\text{Ga}_{1-x})\text{Se}_2$ Solar Cells

J. Wands, P. Tsoulka, T. Lepetit, N. Barreau, and A. Rockett, "Effects of Novel In+RbF Post-Deposition Treatment on $\text{Cu}(\text{In}_x\text{Ga}_{1-x})\text{Se}_2$ Solar Cells," in 2022 IEEE 49th Photovoltaics Specialists Conference (PVSC), Jun. 2022, pp. 0415–0417. doi: 10.1109/PVSC48317.2022.9938855.

Contributions: Performed temperature-dependent current-voltage experiments, data analysis, document writing, interpretation and development of conclusions.

Large-Area $(\text{Ag,Cu})(\text{In,Ga})\text{Se}_2$ Thin-Film Solar Cells with Increased Bandgap and Reduced Voltage Losses Realized with Bulk Defect Reduction and Front-Grading of the Absorber Bandgap

A. M. Bothwell, S. Li, R. Farshchi, M. Miller, J. Wands, C. Perkins, A. Rockett, A. Arehart, D. Kuciauskas, "Large-Area $(\text{Ag,Cu})(\text{In,Ga})\text{Se}_2$ Thin-Film Solar Cells with Increased Bandgap and Reduced Voltage Losses Realized with Bulk Defect Reduction and Front-Grading of the Absorber Bandgap," Sol. RRL, vol. 6, no. 8, p. 2200230, 2022, doi: <https://doi.org/10.1002/solr.202200230>.

Contributions: Time-of-flight secondary ion mass spectroscopy analysis.

Non-Radiative Recombination Dominates Voltage Losses in $\text{Cu}(\text{In,Ga})\text{Se}_2$ Solar Cells Fabricated Using Different Methods

A. M. Bothwell, J. Wands, M. Miller, A. Kanevce, S. Paetel, P. Tsoulka, T. Lepetit, N. Barreau, N. Valdes, W. Shafarman, A. Rockett, A. Arehart, D. Kuciauskas, "Non-Radiative Recombination Dominates Voltage Losses in $\text{Cu}(\text{In,Ga})\text{Se}_2$ Solar Cells Fabricated Using Different Methods," Sol. RRL, vol. n/a, no. n/a, doi: 10.1002/solr.202300075.

Contributions: Performed current-voltage experiments, capacitance-voltage experiments, data analysis.

The existence and impact of persistent ferroelectric domains in MAPbI_3

L. M. Garten, D. Moore, S. Nanayakkara, S. Dwaraknath, P. Schulz, J. Wands, A. Rockett, B. Newell, K. Persson, S. Trolier-McKinstry, D. Ginley, "The existence and impact of persistent ferroelectric domains in MAPbI_3 ," Sci. Adv., vol. 5, no. 1, p. eaas9311, Jan. 2019, doi: 10.1126/sciadv.aas9311.

Contributions: Performed scanning microwave impedance spectroscopy, data analysis.

Structure and phase composition of sputter deposited $(\text{Ag,Cu})(\text{In,Ga})\text{Se}_2$ thin film solar cells

S. Soltanmohammad, J. Wands, R. Farshchi, D. Poplavskyy, and A. Rockett, “Structure and phase composition of sputter deposited (Ag,Cu)(In,Ga)Se₂ thin film solar cells,” in 2018 IEEE 7th World Conference on Photovoltaic Energy Conversion (WCPEC) (A Joint Conference of 45th IEEE PVSC, 28th PVSEC 34th EU PVSEC), Jun. 2018, pp. 0852–0855. doi: 10.1109/PVSC.2018.8547999.

Contributions: Assisted with experiments and data analysis.

Efficient CdTe photovoltaics by co-passivating grain boundaries

F. G. Sen, A. Mannodi-Kanakkithodi, T. Paulauskas, C. Sun, J. Guo, L. Wang, J. Wands, A. Rockett, M. Kim, R. Klie, M. Chan, “Efficient CdTe photovoltaics by co-passivating grain boundaries,” in 2018 IEEE 7th World Conference on Photovoltaic Energy Conversion (WCPEC) (A Joint Conference of 45th IEEE PVSC, 28th PVSEC 34th EU PVSEC), Jun. 2018, pp. 3880–3883. doi:

10.1109/PVSC.2018.8547464.

Contributions: Assisted with experimental data and discussion.

CHAPTER 2

BACKGROUND INFORMATION

This chapter describes the basic mechanics of p-n junctions with an emphasis on how current behaves in a photovoltaic device.

2.1 P-N Junction Basics

The core operation of a PV device relies on a structure called the p-n junction [1, 2]. By contacting an n-type semiconductor with a p-type semiconductor a p-n junction is formed. If the n-type and p-type sides of the junction are made from the same material, it is called a homojunction. Alternatively, two different semiconductors can be used to form a heterojunction. Most thin-film devices, such as CIGS, are made with a heterojunction structure [2].

Before contact the two materials have different Fermi energies, with the n-type material having a higher Fermi energy than the p-type side. Once the two sides are brought together electrons flow from the high Fermi energy n-type material into the lower energy p-type material [1, 2]. The resulting equilibrium state maintains a constant Fermi energy throughout the entire device. To accommodate a constant Fermi energy throughout the device the valence and conduction bands bend near the junction. While the band bending in homojunctions produces a smooth transition from n-type to p-type, heterojunctions are often more complex. If two materials have different bandgaps and electron affinities the p-n junction can have offsets in the conduction and valence bands. This can result in barriers forming at the interface which can change current flow through the device [1, 2].

Due to the flow of electrons out of the n-type material a net-positive charge is formed near the junction. Likewise, the influx of electrons on the p-type side results in a net-negative charged region near the junction. This region is called the depletion or space-charge region and its width is defined by [1]:

$$W = (2\epsilon(V_{BI} - V_{applied})/q((N_A + N_D)/(N_A N_D)))^{1/2} \quad (2.1)$$

where ϵ is the dielectric constant, V_{BI} is the built in voltage, $V_{applied}$ is the external voltage, and N_A and N_D are the concentrations of acceptor and donor states respectively. An electric field forms within the depletion region which resists additional electron flow from the n-type to the p-type region. The magnitude of this electric field, known as the built-in potential, is determined by [1]:

$$V_{BI} = (k_B T)/q * \ln(n_n/n_p) \quad (2.2)$$

where k_B is the Boltzmann constant, T is temperature, q is the electronic charge, n_n is the electron concentration on the n-type side of the junction, and n_p is the electron concentration on the p-type side of the junction. The built-in potential is an essential feature of a p-n junction as it creates a potential field to separate charge carriers. Separating charge carriers is an important component of power generation and will be discussed further in Section 2.3.

A p-n junction also has capacitive properties due to the dielectric behavior of the depletion region. The junction region can be modeled well by a classic parallel plate capacitor whose capacitance is given by [1, 3]:

$$C = (\epsilon A)/d \quad (2.3)$$

where A is the area of the plates and d is the separation of the two plates. In the case of a p-n junction the plate spacing is defined by the width of the depletion region. Since the depletion width is dependent on the external voltage the junction capacitance is as well. The bias-dependent junction capacitance can be calculated by [1]:

$$(2C)/A = \sqrt{(2q\epsilon N_{net})/(V_{BI} - V_{applied})} \quad (2.4)$$

where N_{net} is the difference between majority and minority carrier dopants on the lightly-doped side of the p-n junction. Eq. 2.4 assumes that one side of the junction is more heavily doped which is a common situation in thin-film PV such as CIGS.

Another important feature of p-n junctions is the quasi-Fermi energy. The Fermi energy is an equilibrium property which applies when $np=n_i^2$ (where n_i is the intrinsic carrier concentration) [1, 2]. In a forward biased diode diffusion of electrons and holes outpaces the recombination rate. This results in excess charge carriers and $np>n_i^2$. The Fermi energy for electrons and holes is no longer the same, creating separate electron and hole Fermi energies (E_{Fn} and E_{Fp} respectively) . These separate, non-equilibrium, values are known as quasi-Fermi energies [1, 2]:

$$E_{Fn} - E_i = k_B T \ln(n/n_i) \quad (2.5)$$

$$E_i - E_{Fp} = k_B T \ln(p/n_i) \quad (2.6)$$

where E_i is the intrinsic Fermi energy.

The quasi-Fermi energy separation, $E_{Fn}-E_{Fp}$, defines the maximum achievable voltage across the contacts of a diode. In solar cells, where higher voltages lead to increased efficiency, the quasi-Fermi energy separation is an important quantity. While the quasi-Fermi energy separation defines the maximum voltage, there are often parasitic effects which result in real-world devices producing lower voltages. It is still beneficial to increase quasi-Fermi energy separation as much as possible which can be achieved by

increasing excess carrier generation as seen in Eq. 2.5 and Eq. 2.6. In a solar cell, excess carriers generated by absorbing photons create the quasi-Fermi energy separation necessary for power output.

2.2 Current in a Photovoltaic Device

In a diode there are two primary chemical potential gradients that can lead to current: charge carrier concentration and electrical potential. These driving forces result in two distinct currents within the device. The difference in charge carrier concentration leads to a diffusion current while a change in electrical potential creates a drift current. Current in solar cells is often normalized by device area and reported as current density. The diffusion current density can be written as [1, 2]:

$$J_{diff} = J_0 \exp(qV)/(k_B T) \quad (2.7)$$

where J_{diff} is the diffusion current density, q is the charge of an electron, V is the applied bias, k_B is the Boltzmann constant and J_0 is the reverse saturation current density represented by:

$$J_0 = -q((D_p/L_p)p_n + (D_n/L_n)n_p) \quad (2.8)$$

The drift current density is described as:

$$J_{drift} = q((D_p/L_p)p_n + (D_n/L_n)n_p) \quad (2.9)$$

where J_{drift} is the drift current density, D_n and D_p are the electron and hole diffusivities respectively, L_n and L_p are the carrier diffusion lengths for holes in the n-type and p-type materials respectively, n_p is the electron concentration on the p-type side of the junction, p_n is the hole concentration on the n-type side of the junction. The total current density in the device is the sum of the drift and diffusion currents:

$$J = J_0(\exp(qV)/(k_B T) - 1) \quad (2.10)$$

Eq 2.10 describes the current in an ideal diode without the effects of recombination. These conditions are rarely achieved and therefore the equation is modified to account for recombination currents [1, 2]:

$$J = J_0(\exp(qV)/(nk_B T) - 1) \quad (2.11)$$

where n is the diode ideality factor which ranges from one in an ideal diode to two in diodes with large recombination currents. It is possible for the diode ideality factor to rise above two under the influence of tunneling currents or a significant series resistance.

An additional modification to the ideal diode equation is needed to account for series and shunt resistances. These deviations from the ideal diode are depicted in the circuit diagram shown in Figure 2.1. Series resistance originate from material resistivity, poor contacts, and interface effects, while shunt resistance may affect a device through pinholes that create a current pathway through the junction.

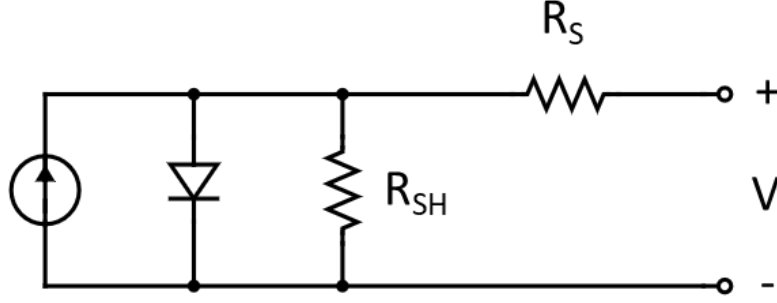


Figure 2.1 Equivalent circuit diagram of a solar cell including the parasitic series and shunt resistances.

Mathematically these resistances can be represented as [1, 2]:

$$J = J_0(\exp(q(V + JR_S)/(nk_B T)) - 1) + (V + JR_S)/R_{SH} \quad (2.12)$$

where R_S is series resistance and R_{SH} is shunt resistance.

A key assumption made in Eq. 2.12 is that the diode is operating in the dark, which does not represent the standard operating conditions of a solar cell. A final modification is made by subtracting the photocurrent to arrive at the final equation for current in a solar cell [1, 2]:

$$J = J_0(\exp(q(V + JR_S)/(nk_B T)) - 1) + (V + JR_S)/R_{SH} - J_L \quad (2.13)$$

where J_L is the light induced photocurrent. In an ideal solar cell, J_L acts by simply translating the dark JV curve downwards.

Several sources of temperature-dependent behavior exist in Eq. 2.13. Aside from the explicit temperature term in the exponent there are several temperature-dependent variables. The ideality factor can vary with temperature if the recombination mechanism is temperature-dependent [4]. Both the series and shunt resistance terms can be temperature-dependent in the case of an activation barrier [4]. Reverse saturation current density is also temperature-dependent and can be alternatively defined as [5]:

$$J_0 = J_{00} \exp(-E_a/(nk_B T)) \quad (2.14)$$

where J_{00} is the current density prefactor and E_a is the diode activation energy. The temperature-dependence of a solar cell's JV curve is a valuable tool in analyzing device performance and will be explored further in Chapters 4 and 5.

2.3 Performance Characteristics of Solar Cells

Figure 2.2 provides an example of the dark and light J-V curves of a solar cell. When operating in the fourth quadrant of the graph the solar cell is producing power which can be captured for use.

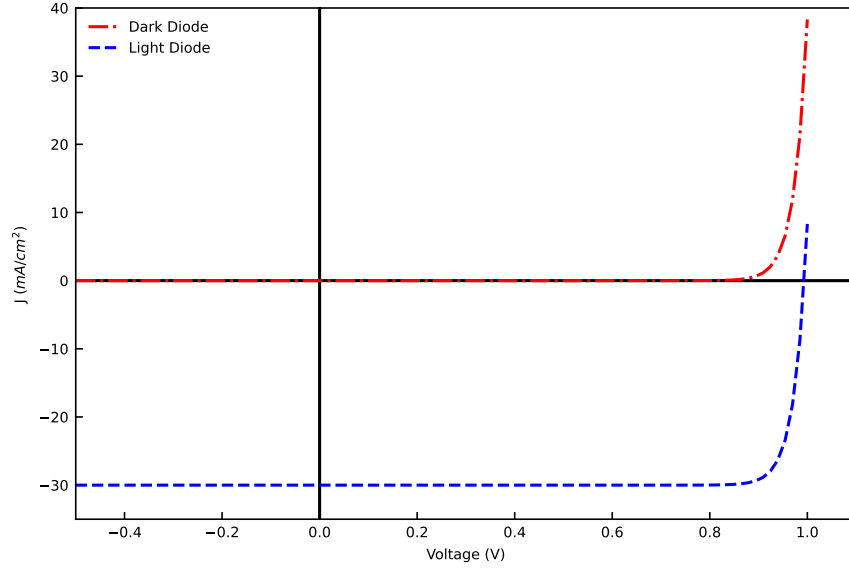


Figure 2.2 Comparison of dark and light JV curves in an ideal solar cell.

The complete J-V curve of a solar cell provides key parameters in evaluating the device's performance. The first is short-circuit current density (J_{SC}) which is defined as the current density at $V=0$. In an ideal cell this value is equal to J_L and represents the maximum current in the fourth quadrant. Open-circuit voltage (V_{OC}) is another key metric and is the voltage at $J=0$. The final parameter is fill factor (FF) which is defined as [1, 2]:

$$FF = (J_{mp}V_{mp})/(J_{SC}V_{OC}) \quad (2.15)$$

where J_{mp} and V_{mp} are the current and voltage at the maximum power point respectively. Combining these three values results in an equation for the overall device conversion efficiency [1, 2]:

$$\eta = (V_{OC}J_{SC}FF)/P_{in} \quad (2.16)$$

where P_{in} is the power of radiation incident on the surface of the device.

2.4 Defects and Recombination

In a perfect semiconductor there are no energy states between the conduction and valence bands, however in real devices, defects can create energy states in the bandgap (Figure 2.3). The properties of semiconducting materials are often dominated by defects that influence the behavior of charge carriers [1, 6]. Defects can take many forms, but their impact on a material is caused by variations in the local energy potential of the crystal [6]. In doing so, energy states are created within the bandgap that can trap carriers, causing non-radiative recombination. Intrinsic defects are present in a chemically pure material

and consist of interstitials, anti-sites, vacancies, dislocations, and grain boundaries. On the other hand, extrinsic defects originate from defect elements in the lattice which occupy lattice or interstitial sites.

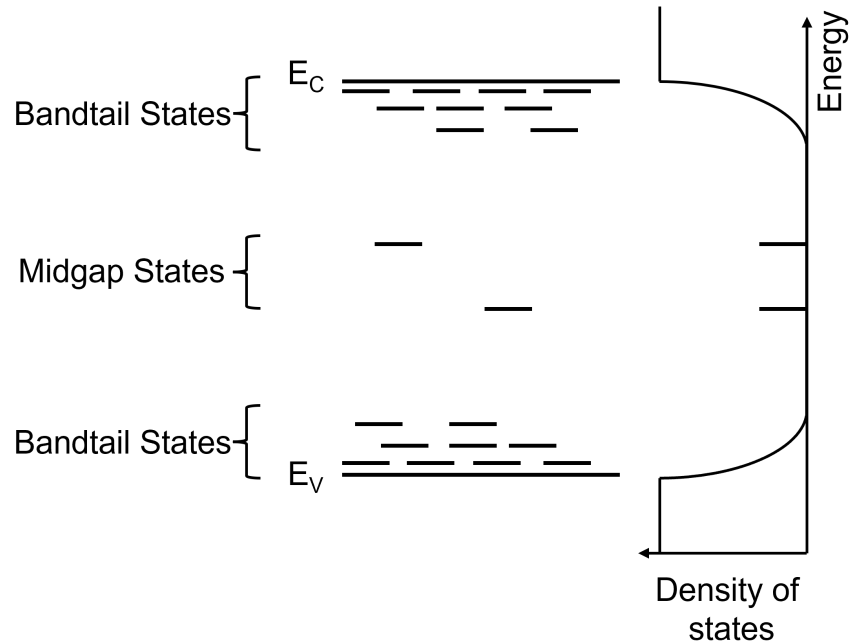


Figure 2.3 Band diagram depicting midgap and bandtail states existing within the bandgap. A density of states sketch is included to display the exponential decay of states which leads to bandtails.

The primary concern for photovoltaics is the behavior of minority carriers, which dictate many of the device properties [2]. Equal numbers of holes and electrons must be collected at the contacts to maintain charge neutrality. Because the majority carrier concentration is high, recombination processes will only affect a small percentage of majority carriers under most conditions. In contrast, minority carriers have much lower concentration and can be severely impacted by recombination. Reducing the minority carrier concentration will lower the quasi-Fermi level and therefore the V_{OC} , which is derived from the separation of the two quasi-Fermi levels [2]. As such, defects which primarily impact minority carriers are the most concerning in photovoltaics and are the focus of most studies.

Defect states can be located anywhere within the band gap and their location determines much of the resulting impact on a device. States near the band edges, known as shallow states, are generally created by defects that only perturb the electron potential energy by a small amount. Shallow states often act as primary donors or acceptors, which easily provide carriers in the adjacent bands through thermal excitation [1, 6]. In this way, defects can be beneficial, as many semiconductor devices rely on shallow dopants to function.

The band edges can also have more complicated structures such as bandtails, which are characterized by a high density of energy states near the valence or conduction bands [2]. Bandtails decay exponentially into the bandgap with the width of the bandtail defined by a characteristic energy. Bandtails result from localized variations in the chemistry or defect structure of the material, driven by entropy. Materials prone to disorder, like CuInSe₂, can have slightly different bandgap values throughout a film, which creates bandtails that extend into the gap [7]. This blurring of the band edges results in a lower effective bandgap, which can affect properties such as the absorption coefficient at sub-gap wavelengths. Reducing the effective bandgap also results in a drop in V_{OC} which will reduce the efficiency of a photovoltaic device [7].

States closer to mid-gap are deep states and often have negative effects on the device. Deep states can act as either a trap or a recombination center, depending on their position within the bandgap as well as their charge [1]. This mechanism of defect assisted recombination is known as Shockley Read Hall (SRH) recombination (Figure 2.4) and is a primary concern for semiconductor devices [1, 2, 6]. Minority carrier lifetime is reduced due to increased recombination rates.

Substitutional defects may consist of impurity atoms occupying a lattice site, or anti-site defects resulting from an intrinsic atom located on an incorrect lattice site. These defects can affect the crystal structure by introducing strain due to the size difference between the intrinsic atom and the defect atom. Additionally, the difference in electronic structure for the defect atom will disturb the local potential. The extent of the difference in size and electronic structure has a large effect on the depth of the defect state within the bandgap [1]. Point defects that are more localized in real space are delocalized in reciprocal space, making them effective at recombining charge carriers.

Polycrystalline thin films have the added complexity of grain boundaries, which present a unique challenge. Grain boundaries are significant sources of defect states as they interrupt the matrix periodicity during the transition from one grain to another. Dangling bonds that create states within the gap are common as the two grains may not match perfectly. Dangling bonds are a particular problem as they tend to pin the Fermi energy near midgap [1]. Fortunately, in polycrystalline materials with significant ionic character, dangling bond states are often near the band edge and also often compensate each other [1]. Grain boundaries also collect impurity atoms due to the additional space created by the mismatch. The wide range of impurity atoms concentrating in the grain boundary may result in defect states deep in the gap [2]. Trapping and recombination are a major concern with carriers in the grain boundary region. Despite the issues presented by grain boundaries some polycrystalline thin films still manage to produce high quality devices. CIGS are most common as polycrystalline absorbers. Passivation mechanisms in the grain boundaries of these materials are necessary to mitigate the impacts of defects.

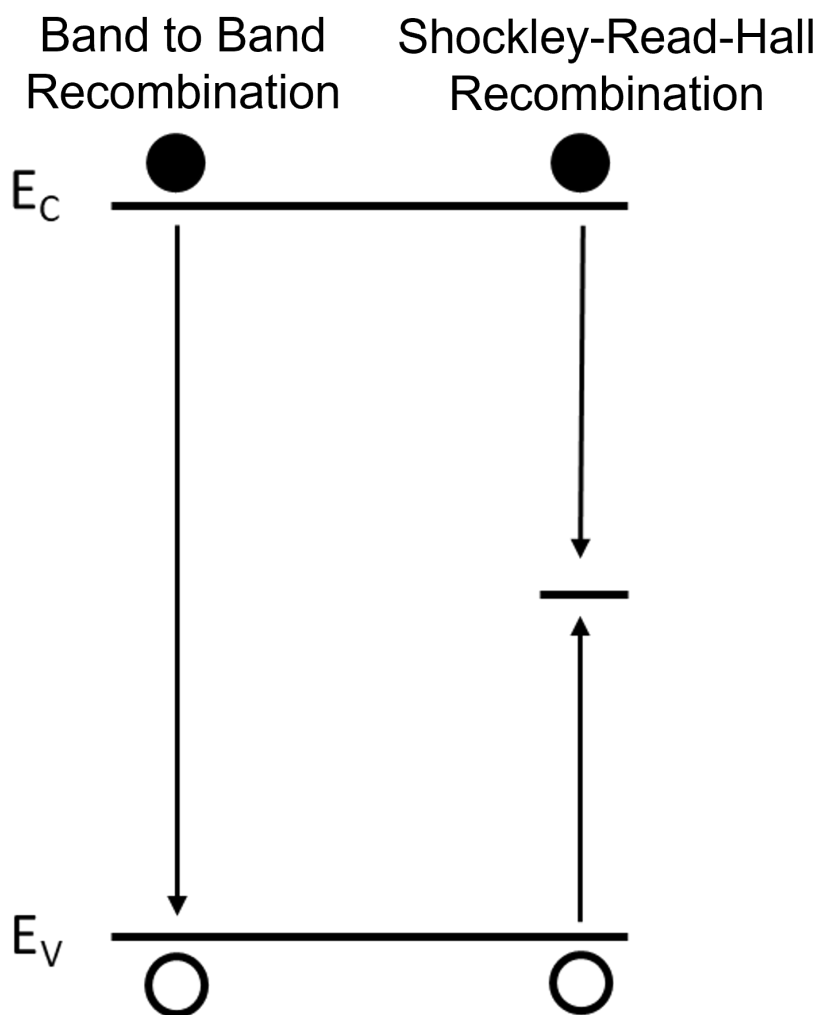


Figure 2.4 Sketch showing how midgap defects lead to Shockley-Read-Hall recombination in a solar cell.

The rate of recombination in a solar cell is proportional to the value of J_0 [2]. Higher J_0 values indicate greater rates of recombination. This property makes J_0 a valuable tool in analyzing the performance of a solar cell. By measuring J_0 from JV curves, the relative recombination rates can be compared between devices.

Another valuable tool in studying recombination is the diode activation energy (E_a). E_a is an indicator of where recombination is occurring within a device [2]. If $E_a \approx E_g$, recombination is primarily in the bulk absorber material. If $E_a < E_g$, recombination is dominated by the interfaces. Calculating E_a through temperature-dependent JV experiments is an important technique for diagnosing the primary recombination mechanisms within a solar cell.

CHAPTER 3

Cu(In_xGa_{1-x})Se₂ PHOTOVOLTAIC DEVICES

This chapter gives a brief overview of Cu(In_xGa_{1-x})Se₂ solar cells. An overview of alkali halide treatments is provided for context in the following chapters.

3.1 Material Structure

CuInSe₂ (CIS) is a ternary compound exhibiting a chalcopyrite structure as seen in Figure 3.1 [2, 8, 9]. CIS is a semiconductor with a direct bandgap of 1.04 eV, which is lower than the ideal value for maximizing photovoltaic efficiency predicted by Shockley and Queisser [10]. To increase the bandgap, CIS is often alloyed with CuGaSe₂ which has a bandgap of 1.68 eV. The resulting alloy, Cu(In_xGa_{1-x})Se₂ (CIGS), has a continuously tunable bandgap defined by the equation [11]:

$$E_g(x) = 1.04(1 - x) + 1.68x - 0.2x(1 - x) \quad (3.1)$$

Although the ideal bandgap for single-junction solar cells is around 1.4 eV which would correspond to $x=0.6$, CIGS films are often grown near $x=0.2-0.3$ resulting in a bandgap of around 1.15 eV [12]. Above $x=0.3$, CIGS devices often decrease efficiency despite the bandgap being closer to the ideal value. Several factors may contribute to the decreased efficiency including higher defect concentration, defects closer to midgap acting as recombination centers, and poor band alignment with the standard CdS buffer layer [12].

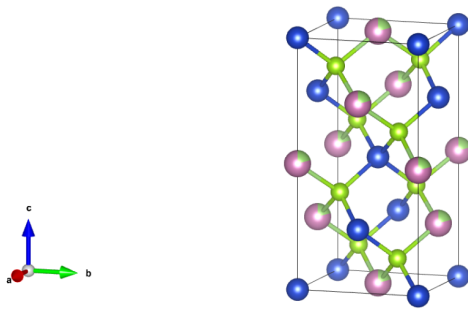


Figure 3.1 Unit cell for the CIGS absorber material. Cu is shown in blue, Se in light green, and the group III elements, In and Ga, occupy the same lattice sites and are depicted by spheres which are split between dark green and pink.

CIGS films are generally polycrystalline and are known to have excellent tolerance to defects and variations in stoichiometry [13]. A p-type CIGS absorber layer is generally used, which is intrinsically

doped, interpreted as due to V_{Cu} . The predicted low formation energy and shallow location (30 meV above the valence band maximum) make this defect an effective dopant [14].

3.2 PV Device Structure

The structure of a typical CIGS solar cell is shown in Figure 3.2. Due to the high absorption coefficient of CIGS, complete solar cells can be made to be very thin (CIGS layer is $\approx 1\text{-}2\ \mu\text{m}$) [15]. This opens the possibility of flexible solar panels by using a flexible substrate [16]. While soda-lime glass is the most common substrate for CIGS devices, flexible devices can be made using a polymer or steel foil as the substrate.

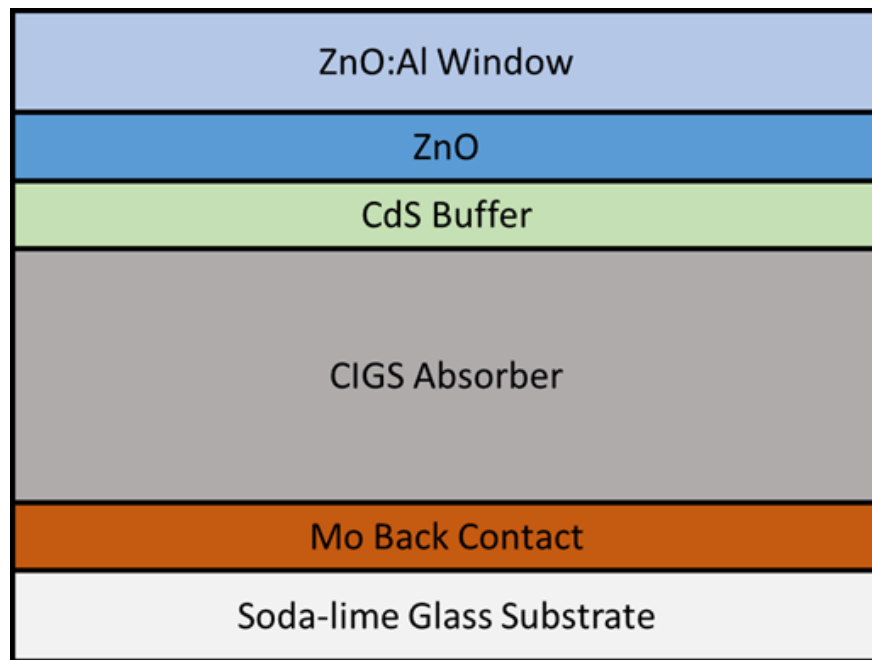


Figure 3.2 Structural diagram of a typical CIGS solar cell such as those presented in the following chapters.

The rear contact material plays an important role, due to the difficulty of forming an ohmic contact with CIGS. Most devices use molybdenum as the rear contact due to its favorable band alignment [17, 18]. Mo also has low miscibility with Cu, In, and Ga which limits diffusion of the back contact into the absorber layer [19, 20]. During deposition of the CIGS layer it is common for a MoSe_2 layer to form at the interface [21]. The formation of a MoSe_2 layer is generally thought to improve rear contact performance by improving band alignment between the CIGS and Mo layers [22].

High efficiency CIGS devices often incorporate a bandgap gradient by varying the Ga content through the depth of the film [23]. This is often achieved through a 3-stage co-evaporation process which results in a V-notch shape to the bandgap profile. The V-notch profile improves carrier collection by reducing

recombination at the interfaces [23].

CdS is the most common material used to form the heterojunction with CIGS, although other options exist [18]. CdS is typically deposited using chemical bath deposition, which produces consistent, high quality buffer layers. The band alignment with CIGS is also favorable, and CdS produced the highest efficiency devices for many years [24]. However, the toxicity of Cd, along with a relatively low bandgap which leads to parasitic losses in blue light, have led to research into alternatives. Zn(O,S) is a common choice due to its high bandgap which is tunable through the O:S ratio [25]. The current record efficiency CIGS solar cell uses a $\text{Zn}(\text{O,S,OH})_x/\text{Zn}_{0.8}\text{Mg}_{0.2}\text{O}$ double buffer layer [26]. An additional benefit to Zn(O,S) is the potential for vapor deposition which opens the possibility of roll-to-roll manufacturing.

3.3 Effect of Alkali Metals

3.3.1 Light Alkalis

Alkali metals, especially sodium and potassium, have long been known to provide performance benefits which are key to high-efficiency cells [27, 28]. Na has been shown to increase carrier concentration and may passivate defects at grain boundaries where it preferentially sits [29]. Na traditionally was sourced through diffusion from the soda-lime glass (SLG) substrate into the bulk, but modern processes can introduce alkali metals with post-deposition treatments (PDT) or by diffusion from the back contact [30].

3.3.2 Rubidium

Recently there has been more research into the effects of heavier alkali metals such as Rb and Cs on CIGS devices [31–33]. In particular, RbF PDT has gained attention as a promising method of increasing V_{OC} [25, 34]. Rb has shown the potential to outperform Na and K in improving cell efficiency.

Despite the observed benefits of RbF PDT there is still debate in the literature about the mechanisms by which RbF improves CIGS solar cells. Several studies have found Rb to concentrate at the grain boundaries and interfaces [35–37]. Atom probe tomography and time-of-flight secondary ion mass spectrometry have shown Rb atoms to diffuse along grain boundaries and replace lighter alkalis such as Na and K [35]. The result is a grain interior that is richer in light alkalis while the grain boundaries have high concentrations of Rb. Rb appears to passivate the grain boundaries which leads to reduced recombination and increased V_{OC} [35, 38]. Some studies suggest that Rb decreases the amplitude of potential fluctuations at the grain boundaries which leads to increased quasi-Fermi level splitting [39]. Kelvin probe microscopy has been used to observe a decrease in potential variations across grain boundaries following RbF PDT [35].

The heterojunction also appears to be affected by Rb, possibly through the formation of RbInSe_2 phases [40, 41]. Scanning transmission electron microscopy has been used to directly observe RbInSe_2 forming

between the CdS buffer and CIGS absorber layer [41]. It is theorized that the RbInSe₂ bandgap of ≈ 2 eV improves band alignment at the junction, leading to a reduction in interface recombination [33, 42].

CHAPTER 4

EVALUATING RECOMBINATION MECHANISMS IN RbF TREATED $\text{Cu}(\text{In}_x\text{Ga}_{1-x})\text{Se}_2$ SOLAR CELLS

Reproduced with the permission of the IEEE Journal of Photovoltaics.

Jake Wands¹, Ana Kanevce², Alexandra Bothwell³, Michael F. Miller⁴, Stefan Paetel², Aaron R. Arehart⁴,
Angus Rockett¹

4.1 Abstract

RbF post-deposition treatment (PDT) has been shown to improve the performance of $\text{Cu}(\text{In}_x\text{Ga}_{1-x})\text{Se}_2$ (CIGS) photovoltaic devices. In this study temperature-dependent current voltage (JVT) and time-resolved photoluminescence (TRPL) experiments were combined with modeling using the SCAPS computer code to investigate the effect of the RbF PDT. Two devices, one as-deposited and one with RbF PDT, were deposited by a three stage co-evaporation process. JVT measurements suggest the dominant recombination mechanism may be tunneling-enhanced recombination via bandtail states, but that defect states in the bandgap can also be important. RbF PDT is shown to decrease the characteristic energy of the bandtails. TRPL data show an increase in the minority carrier lifetime after RbF PDT, leading to an improved open-circuit voltage. SCAPS modeling indicates that the dominant recombination mechanism is dependent on the specific defect makeup of a device, suggesting that small changes in processing conditions can impact device behavior. This explains the observation that, for some devices, defect states in the gap dominate while others, as is the case here, appear to be dominated by bandtails.

4.2 Introduction

Among thin-film photovoltaics $\text{Cu}(\text{In}_x\text{Ga}_{1-x})\text{Se}_2$ (CIGS) is one of the most studied. Consequently, the champion small device efficiency has reached 23.4% [26]. Despite extensive research there is still debate about the mechanisms preventing further improvements. CIGS devices are often observed to have an open-circuit voltage (V_{OC}) well below the theoretical maximum, resulting in lower energy conversion efficiency [43]. Understanding the origin of this V_{OC} deficit is necessary to boost efficiency and keep CIGS as a leading thin-film technology. Two possible sources of V_{OC} loss in the bulk absorber have been proposed: point defects and bandtails. Commonly identified point defects include a midgap trap located

¹Colorado School of Mines, 1500 Illinois St, Golden, CO 80401 USA

²Zentrum fuer Sonnenenergie und Wasserstoff-Forschung Baden-Wuerttemberg, Stuttgart 70563, Germany

³National Renewable Energy Laboratory, 15013 Denver West Parkway, Golden, CO 80401 USA

⁴The Ohio State University, 281 W Lane Ave, Columbus, OH 43210 USA

approximately 580 meV above the valence band edge ($E_V+0.58\text{eV}$) and an $E_V+0.98\text{eV}$ defect, proposed to be associated with a $V_{\text{Cu}}-V_{\text{Se}}$ divacancy complex [31, 44, 45]. Bandtails can be caused by impurities as well as structural disorder within a crystal lattice [35, 38, 46]. Structural disorder is often observed in CIGS and results in bandgap fluctuations as the Ga/III ratio changes [47].

One focus of research is alkali-halide post-deposition treatment (PDT) of the material. RbF is a popular choice for PDT of CIGS thin films and has shown improvement in photovoltaic device performance, in part by increasing the V_{OC} [48]. While several mechanisms have been used to explain device improvements there is still debate in the literature [33, 49, 50]. To maximize the benefit of RbF PDT it is necessary to understand how the process acts to increase V_{OC} . Relatively small changes in processing conditions can have significant impacts on the defects discussed in this study, which further complicates analysis. A RbF PDT may have different influences depending on the processing conditions by which the material was produced, which motivates robust study across a variety of samples.

This study aims to contribute additional information to the literature covering RbF PDT CIGS devices made at Zentrum für Sonnenenergie- und Wasserstoff-Forschung Baden-Württemberg (ZSW). Previous work has shown that a variety of factors coupled with RbF PDT may be present. Kanevce et al. used current-voltage measurements to show that RbF can change interface recombination, which may be a dominant problem [25]. Siebentritt et al. used atom probe tomography and kelvin probe force microscopy to suggest that Rb accumulation at grain boundaries may reduce potential fluctuations and therefore decrease the impact of bandtails [35]. Wolter et al. used photoluminescence to find that RbF increases the quasi-Fermi level separation which leads to improved V_{OC} [38]. In this work temperature dependent current-voltage (JVT) and time-resolved photoluminescence (TRPL) experiments are combined with SCAPS (Solar cell CAPacitance Simulator) modeling to gain a better understanding of the recombination effects of RbF PDT on CIGS for the industrial fabrication process used for the devices presented here.

4.3 Experimental Methods

To better understand the recombination mechanisms present in the samples used in this study, JVT experiments were conducted. Measurements were performed with a solar simulator calibrated to 100 mW/cm^2 , and the temperature was lowered from 350 K to 150 K in 10 K increments. Saturation current density, ideality factor, series resistance, and shunt resistance were extracted using the methods outlined in [4]. The parameters were calculated from dark JV curves to minimize possible impacts of voltage-dependent carrier collection.

JVT experiments can provide valuable insight into recombination dynamics by determining the diode activation energy (E_A) and applying recombination models to measured data. A common method for

determining the diode activation energy is to analyze V_{OC} as a function of temperature [5]. For a diode with a thermally activated transport mechanism the temperature dependence of V_{OC} can be modeled as:

$$V_{OC} = E_A/q - (n(T)kT)/q * \ln(J_{00}/J_L) \quad (4.1)$$

where $n(T)$ is the ideality factor, J_L is the light-induced photocurrent density, and J_{00} is the reverse saturation current density prefactor which is related to the reverse saturation current by:

$$J_0 = J_{00} \exp(-E_A/(n(T)kT)) \quad (4.2)$$

Using (4.1) the diode activation energy (E_A) can be calculated from the 0K intercept of a V_{OC} vs T plot. If $E_A = E_g$ the dominant recombination mechanism is expected to be in the bulk of the absorber, while $E_A < E_g$ is associated with interface recombination.

Recombination in a diode can be better understood by fitting $n(T)$ to a theoretical model. Rau proposed a method of tunneling assisted recombination via an exponential distribution of trap states near the band edge [51, 52]. In this model carriers tunnel from the conduction and valence bands into bandtail states where recombination can occur. The result is an increase in the recombination rate due to the tunneling process. These trap states can be caused by bandtails or potential fluctuations due to composition changes and charged defects. In this scenario the ideality factor is determined by:

$$1/n = 1/2 * (1 - E_{00}^2/(3(kT)^2) + T/T^*) \quad (4.3)$$

Where E_{00} is the characteristic tunneling energy and kT^* represents the characteristic energy of the trap state distribution. This model has been used to describe CIGS devices and provides valuable information about bandtails and tunneling characteristics.

TRPL was measured with pulsed laser excitation at 640 nm with a 1.1 MHz repetition rate and 300-fs pulses. To ensure photogenerated carriers did not screen electric fields in the material the incident excitation was minimized to fluences of 1.2×10^{11} and 1.0×10^{11} photons/(cm²pulse) for the as-deposited and RbF-treated devices respectively. Time-correlated single photon counting was employed, and a silicon avalanche photodiode and band pass filter were used for detection.

The Ga/III ratio was calculated based on Time-of-Flight Secondary Ion Mass Spectroscopy (TOF-SIMS) depth profiles. The Ga and In signals were first normalized to total counts, then the ratio was scaled in order to match the composition at the minimum point with the 1.15 eV bandgap determined by EQE. The composition was determined from bandgap using the relationship [11]:

$$E_g(x) = 1.04 * (1 - x) + 1.68x - 0.2x(1 - x) \quad (4.4)$$

TOF-SIMS depth profiles for each sample are provided in the Appendix Figures 4.8-4.10. Due to a possible mass interference between Rb+ and GaO+ the signals for ⁶⁹Ga and ⁷¹Ga were compared with ⁸⁵Rb and

^{87}Rb . The Ga isotope signals follow each other at the expected ratio throughout the bulk. The Rb isotopes track a different path in the expected ratio confirming interference is not occurring. In addition the O signal is low throughout the bulk, further supporting that the Rb signal is representative of the true Rb content. The RbF PDT sample shows evidence of Rb displacing Na near the front junction as there is a decrease in the Na signal between 8000-15000 seconds of sputter time which is not present in the as-deposited sample.

Deep level transient spectroscopy (DLTS) and deep level optical spectroscopy (DLOS) measurements were performed on the devices to provide full-bandgap defect characterization. Full solar cells were scribed to isolate 1 mm^2 devices for capacitance measurements, which were performed using a Boonton 7200 capacitance meter and a measurement setup described in [53]. The concentrations of the traps observed with DLTS were calculated using the lambda corrected peak height of the DLTS signal [54], and the concentrations of the traps observed with DLOS were calculated using the step height of the steady-state photocapacitance signal [54].

4.4 Measured Devices

The samples are grown by a 3-stage co-evaporation method in an inline deposition chamber. More details are described in Ref. (14). Device performance parameters for the measured samples at 300K are listed in Table 4.1. The as-deposited sample had a V_{OC} of 658mV and fill factor (FF) of 61.1%. After RbF PDT the V_{OC} is increased by 75 mV, a relative improvement of 11.4%. Additionally, the FF rises from 61.1% to 64.9% which results in the overall efficiency improving from 13.1% to 15.3%. The J_{SC} is notably stable at about 32 mA/cm^2 . The series resistance was measured to be $2.5\ \Omega\cdot\text{cm}^2$ and $3.8\ \Omega\cdot\text{cm}^2$ for the as-deposited and RbF PDT samples, respectively. Shunt resistance was measured at $920\ \Omega\cdot\text{cm}^2$ and $1960\ \Omega\cdot\text{cm}^2$ for the as-deposited and RbF PDT samples respectively. While better performing devices are produced at ZSW routinely, these were selected because they provide the ability to simulate the dominant defect here. We note that the best devices may be limited by different effects than those studied here, however, consistency is important to the commercial success of CIGS photovoltaics, so it is valuable to study why some devices underperform even when created on the same tooling.

Table 4.1 Summary of experimental and SCAPS model device parameters at 300 K

		V_{OC} (mV)	J_{SC} (mA/cm ²)	FF (%)	η (%)
As-deposited	Experimental	658	32.5	61.1	13.1
	Model	656	32.6	64.0	13.7
RbF PDT	Experimental	730	32.3	64.9	15.3
	Model	728	32.6	65.1	15.4

4.5 Device Model

To investigate the impact of defects on CIGS devices the simulation software SCAPS was used to create a model for samples with and without RbF PDT [55]. Experimental data were used where possible to improve the model's accuracy and minimize fitting parameters. DLTS and DLOS provided defect concentrations and cross-sections for both the $E_V+0.58\text{eV}$ and the $E_V+0.98\text{eV}$ trap, which have been the dominant defects observed across many CIGS suppliers [31, 44, 56]. In addition to these two defect states, the model utilizes bandtails for both the conduction and valence bands. Bandtails are modeled using a density of states, which decays exponentially from the band edge value with a characteristic energy. The full set of SCAPS model parameters are provided in the Appendix Tables 4.2-4.4.

To verify the model, simulated JV curves were compared with measured JV device data (Figure 4.1). The model shows a close fit to experimental results and is within 5% of each device performance metric. The parameters of the model not specified experimentally were varied and the results compared with experimental behaviors. The experimental data could not be fit effectively with other values, as described below, indicating that the model is a robust representation of the experiments. In other words, the fit is necessary, not merely sufficient.

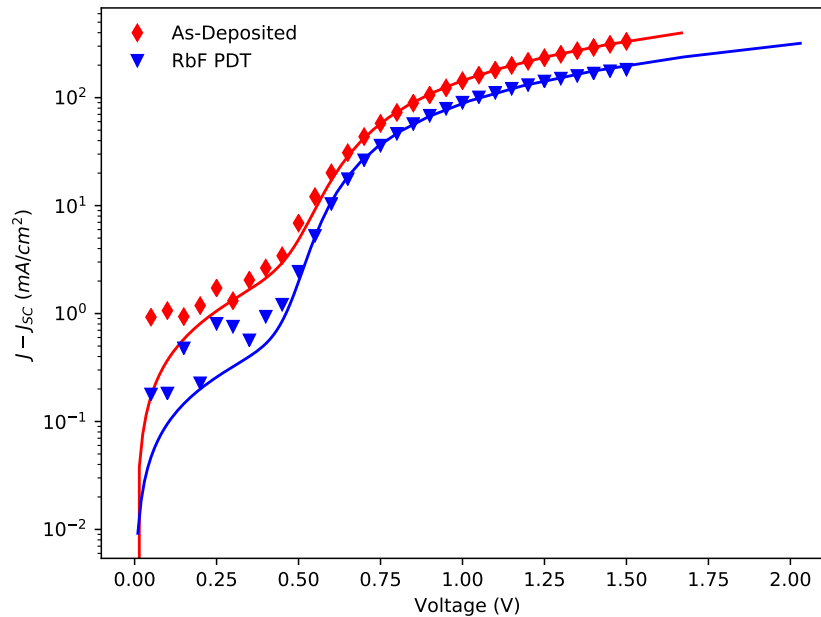


Figure 4.1 Simulated and experimental plots of $J - J_{sc}$ as a function of voltage for the as-deposited and RbF PDT samples. The scatter in the experimental (dotted) data is due to experimental noise near J_{sc} .

4.6 Results

To learn more about the effect of defects on device performance, JV curves were simulated over a range of defect concentrations for the $E_V+0.98\text{eV}$ and $E_V+0.58\text{eV}$ defects. The impact of defect concentration on V_{OC} is shown in Figure 4.2. The dashed horizontal line represents the experimentally measured V_{OC} for each device. In both samples the $E_V+0.98\text{eV}$ defect has little effect on V_{OC} until the concentration exceeds $1 \times 10^{17} \text{ cm}^{-3}$. This is significantly higher than the measured values of $2.7 \times 10^{15} \text{ cm}^{-3}$ and $3.3 \times 10^{15} \text{ cm}^{-3}$ for the as-deposited and RbF PDT samples, respectively. For this reason it is likely that the $E_V+0.98\text{eV}$ defect is not a dominant factor in determining V_{OC} in these devices.

At low defect concentrations the $E_V+0.58\text{eV}$ mid-gap trap shows little effect on V_{OC} for both devices. Once the concentration exceeds $1 \times 10^{15} \text{ cm}^{-3}$ there is a significant decline in V_{OC} which continues through the range used in this study. The RbF PDT sample had a measured concentration of $4.3 \times 10^{13} \text{ cm}^{-3}$ for the $E_V+0.58\text{eV}$ defect which is within an order of magnitude of the modeled onset of decline in V_{OC} .

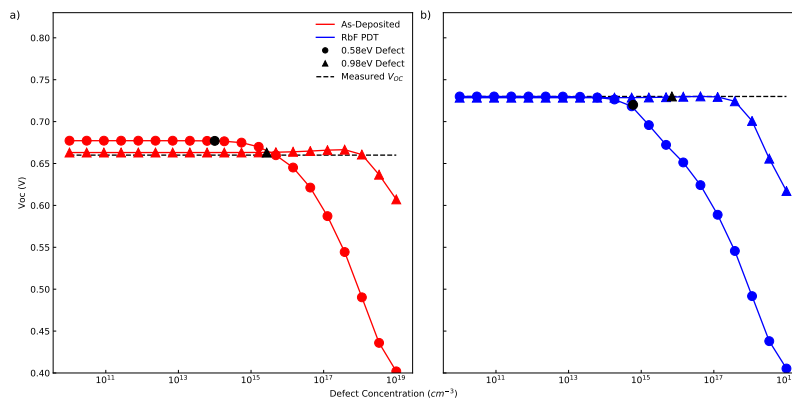


Figure 4.2 SCAPS simulations of V_{OC} as a function of defect concentration for a) as-deposited (shown in red) and b) RbF PDT (shown in blue) samples. Simulated defects include point defects at $E_V+0.58\text{eV}$ (circles) and $E_V+0.98\text{eV}$ (triangles) as well as bandtails (squares). The dotted lines represent the experimentally measured V_{OC} for each device. The black circles and triangles indicate the experimental values of the $E_V+0.58\text{eV}$ and $E_V+0.98\text{eV}$ defects respectively.

In addition to defect concentration the bandtail characteristic energy was also changed to observe the impact on V_{OC} (Figure 4.3). The simulation produces a linear decrease in V_{OC} as the characteristic energy rises and the bandtails extend further from the band edge. Both samples show similar behavior as the bandtail width changes.

The results from this simulation suggest that mid-gap states and bandtails both have a significant role to play in CIGS device behavior. The dominant recombination mechanism may change depending on the specific defect composition of a given sample. In both samples the experimental V_{OC} is already close to the

maximum defect-based limit predicted in the model. Significant gains in V_{OC} may not be possible by reducing the mid-gap defect concentration alone. Therefore bandtails are concluded to be the dominant recombination mechanism in the devices analyzed here.

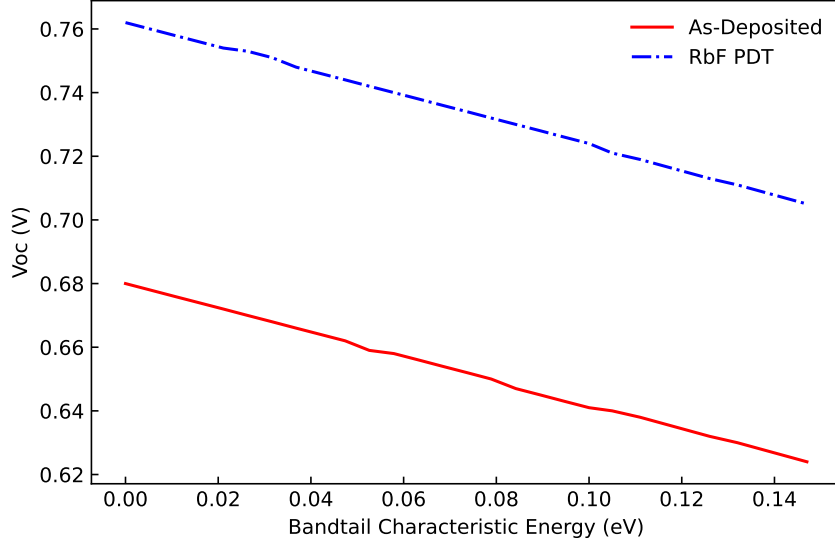


Figure 4.3 SCAPS simulations of V_{OC} as a function of bandtail characteristic energy for as-deposited (red) and RbF PDT (blue) devices.

To investigate the recombination characteristics of the experimental devices, TRPL was performed to measure the minority carrier lifetime. By applying an exponential fit to the tail of the TRPL decays, which are given in Figure 4.4, a tail lifetime improvement from 21.3 ns for the as-deposited device to 47.2 ns with RbF PDT was determined. An approximation of the V_{OC} impact due to increased lifetime can be made by starting with an established equation for V_{OC} [57]:

$$V_{OC} = (kt)/q * \ln((N_A + \Delta n)\Delta n/n_i^2) \quad (4.5)$$

where N_A is the dopant density, Δn is the excess minority carrier concentration, and n_i is the intrinsic carrier concentration. By calculating the difference of (4.5) for the as-deposited and RbF PDT samples it is possible to estimate the portion of V_{OC} increase due to longer lifetime:

$$\Delta V_{OC} = V_{OC,RbF} - V_{OC,As-Dep} \quad (4.6)$$

Simplifying the equation with logarithm rules leads to:

$$\Delta V_{OC} = (kT)/q(\ln(N_{A,RbF} + \Delta n_{RbF}) + \ln(\Delta n_{RbF}) - \ln(N_{A,As-Dep} + \Delta n_{As-Dep}) + \ln(\Delta n_{As-Dep})) \quad (4.7)$$

Assuming $\Delta n \ll N_A$:

$$\Delta V_{OC} = (kT)/q(\ln(N_{A,RbF}) + \ln(\Delta n_{RbF}) - \ln(N_{A,As-Dep}) - \ln(\Delta n_{As-Dep})) \quad (4.8)$$

The excess carrier concentration can be represented by [58]:

$$\Delta n = (J_{SC} * \tau_{eff}) / (q * d) \quad (4.9)$$

where τ_{eff} is the effective minority carrier lifetime and d is the absorber layer thickness. Substituting (4.9) into (4.8) and simplifying terms leads to the final impact of lifetime on V_{OC} :

$$\Delta V_{OC} \propto kT \ln(\tau_{RbF} / \tau_{As-Dep}) \quad (4.10)$$

Using the experimentally measured values gives a ΔV_{OC} of 21 mV. This means that 21mV of the 70mV improvement after RbF PDT can be explained by an increase in carrier lifetime.

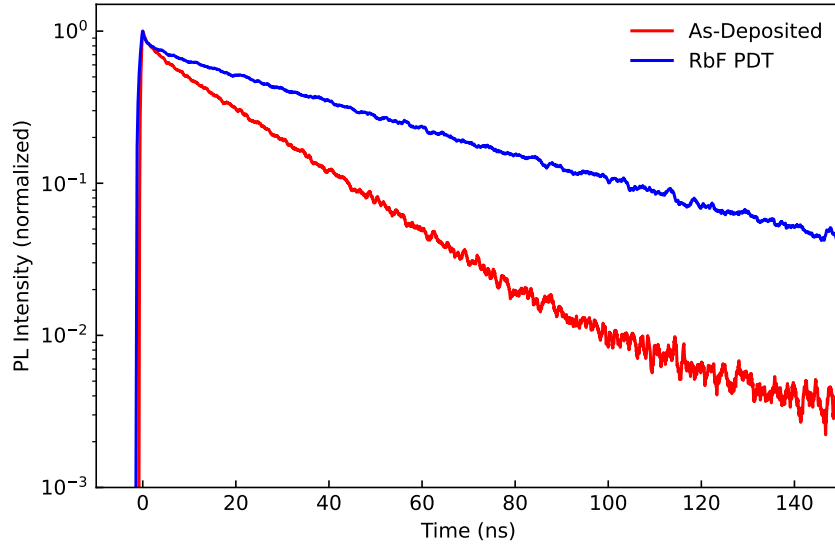


Figure 4.4 TRPL measurements demonstrating the increased lifetime of the RbF PDT sample (blue) compared to the as-deposited sample (red).

JVT data were analyzed to further investigate the dominant recombination mechanism in the experimental devices: V_{OC} is plotted as a function of temperature and extrapolated to 0 K in Figure 4.5. The V_{OC} of the as-deposited sample extrapolates to 1.15 V compared to 1.12 V for the RbF PDT sample. These values are close to the bandgap of 1.15 eV as measured by EQE which suggests bulk recombination in the space-charge region is the dominant mechanism in both devices. It is worth noting that the RbF sample extrapolates to a lower value despite having better overall device performance. This could hint that RbF has some impact at the interface even if the devices perform better, although the effect seen here would be small.

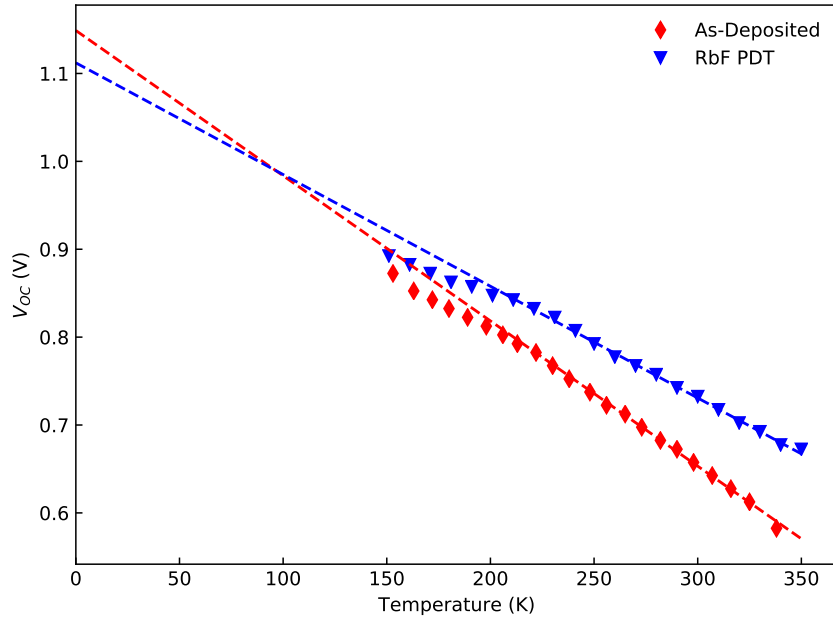


Figure 4.5 V_{OC} vs temperature plots with linear extrapolation to 0 K. The linear extrapolations are taken from the linear region above 230 K.

Significant differences between the two samples appear in the reverse saturation current density (J_0) as seen in Figure 4.6. The as-deposited sample shows J_0 values that are approximately two orders of magnitude higher than those seen in the RbF PDT sample. This is indicative of higher recombination rates which explains some of the V_{OC} deficit observed in JV measurements.

The samples also display differences in ideality factor as a function of temperature which are highlighted in the plot of n^{-1} vs T in Figure 4.7. The as-deposited sample has a higher ideality factor over the entire temperature range, particularly at lower temperatures. Below 280 K the ideality factor in the as-deposited sample rises above two indicating that Shockley-Read-Hall recombination is not the only mechanism at play. The ideality factor in the RbF PDT sample also rises above two but at a lower temperature of 180 K. This may imply that the mechanism which causes high ideality factors is less influential after RbF PDT.

Further analysis was performed by fitting the JVT data with the tunneling enhanced recombination model described by (4.3). Fitting the data shows the as-deposited sample has a tunneling energy of 17 meV while that of the RbF PDT sample is 13 meV. These results suggest that the RbF PDT reduces the impact of tunneling on carrier recombination in the bulk. The decreased tunneling recombination may help explain why the ideality factor is improved for the RbF PDT device. Ideality factor in the RbF PDT device remains between one and two over a wider range of temperatures suggesting purely radiative and SRH recombination are more influential without the effects of tunneling. The dotted line in Figure 4.7 is

the inverse ideality factor calculated with the tunneling term removed from (4.3). This more clearly shows the increased impact of tunneling on the as-deposited sample. In addition, (4.3) predicts the characteristic energy of the trap distribution is 112 meV and 57 meV for the as-deposited and RbF PDT samples respectively. This means that the bandtail width is much higher for the as-deposited sample which could increase recombination. This model suggests that tunneling via bandtail states may be a leading recombination mechanism within the devices.

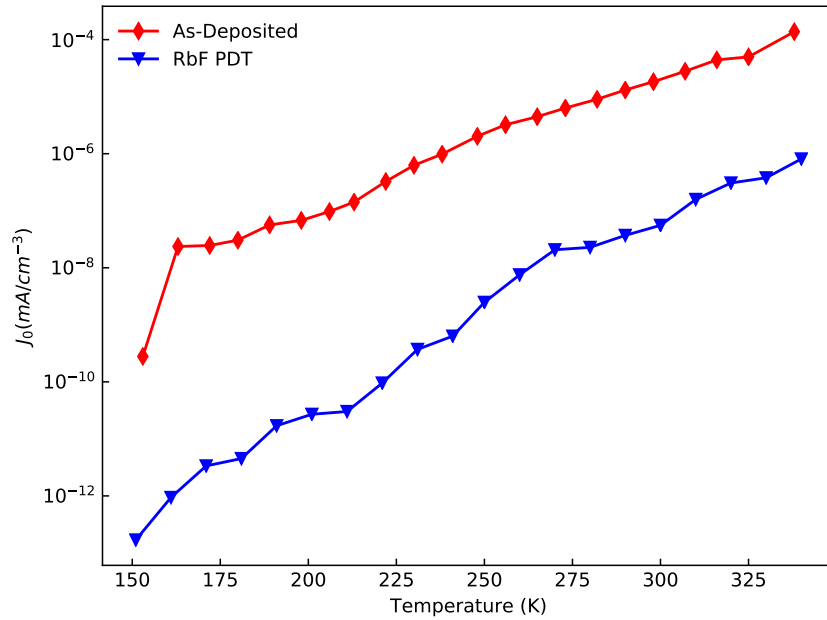


Figure 4.6 J_0 as a function of temperature highlighting the decrease in recombination after RbF PDT.

4.7 Conclusion

In this study the performance of CIGS devices with and without RbF PDT were compared to investigate the source of V_{OC} deficits. SCAPS modeling showed that both point defects and bandtails can present significant factors in performance loss depending on their concentrations. Different processing methods may change the defect concentration and therefore, whether point defects or bandtails are more influential is very process dependent. For this particular set of samples, the simulations propose that reducing the bandtail characteristic energy will improve V_{OC} more than further reductions in point defect concentration.

Additionally, JVT and TRPL experiments provided valuable insight into real devices with and without RbF PDT. TRPL showed an improvement in minority carrier lifetime after RbF PDT which accounts for 21 mV of V_{OC} improvement. While V_{OC} vs T plots suggest both devices are dominated by bulk

recombination, the J_0 values pointed to reduced recombination after PDT. To explain the ideality factor as a function of temperature a tunneling enhanced recombination model was used to fit the data. The fitting parameters imply that the impact of tunneling is reduced with RbF PDT along with the characteristic energy of the bandtails. This result supports previous studies which have found RbF to reduce bandtails and therefore recombination within the bulk.

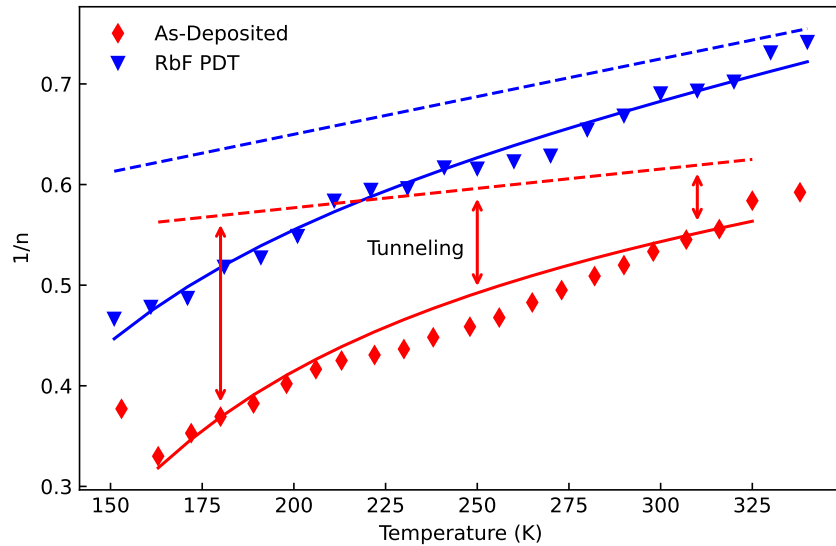


Figure 4.7 Inverse ideality factor vs temperature with the tunneling enhanced recombination model represented by the solid lines. The dotted lines represent the same model with the effect of tunneling removed to highlight the impact of tunneling on recombination.

4.8 Acknowledgment

This research was supported by the U.S. Department of Energy’s Office of Energy Efficiency and Renewable Energy (EERE) under Solar Energy Technologies Office (SETO) Award Number DE-EE0008755. The authors acknowledge German Federal Ministry for Economic Affairs and Energy under Project Number 03EE1078 (ODINCIGS). This work was authored in part by the National Renewable Energy Laboratory, operated by Alliance for Sustainable Energy, LLC, for the U.S. Department of Energy (DOE) under Contract No. DE-AC36-08GO28308. Funding provided by U.S. Department of Energy Office of Energy Efficiency and Renewable Energy Solar Energy Technologies Office. The views expressed in the article do not necessarily represent the views of the DOE or the U.S. Government. The U.S. Government retains and the publisher, by accepting the article for publication, acknowledges that the U.S. Government retains a nonexclusive, paid-up, irrevocable, worldwide license to publish or reproduce the published form of this work, or allow others to do so, for U.S. Government purposes. The authors

thank Dr. Steve Johnston for providing support with the JVT measurement technique. The authors would like to acknowledge Mark Burgelman and the University of Ghent for the SCAPS modelling software.

4.9 Appendix

Table 4.2 SCAPS parameters used to simulate the reference devices.

	CIS	CGS	CdS	ZnO	AlZnO
E_g (eV)	1.04	1.68	2.40	3.30	3.30
χ (eV)	4.56	3.95	4.50	4.45	4.55
ϵ_r	13.6	13.6	10.0	9.0	9.0
N_C (cm ⁻³)	6.2E+17	1.3E+18	2.2E+18	2.2E+18	2.2E+18
N_V (cm ⁻³)	1.5E+19	2.9E+19	1.8E+19	1.8E+19	1.8E+19
$\nu_{t,e}$ (cm/s)	1.0E+07	1.0E+07	1.0E+07	1.0E+07	1.0E+07
$\nu_{t,h}$ (cm/s)	1.0E+07	1.0E+07	1.0E+07	1.0E+07	1.0E+07
μ_e (cm ² /Vs)	100	100	10	0.8	8.4
μ_h (cm ² /Vs)	25	25	10	0.8	8.4
N_a/N_d (cm ⁻³)	3.0E+16	3.0E+16	8.0E+17	1.0E+19	3.4E+20

Table 4.3 SCAPS parameters used to simulate the RbF PDT devices.

	CIS	CGS	CdS	ZnO	AlZnO
E_g (eV)	1.04	1.68	2.40	3.30	3.30
χ (eV)	4.56	3.95	4.50	4.45	4.55
ϵ_r	13.6	13.6	10.0	9.0	9.0
N_C (cm ⁻³)	6.2E+17	1.3E+18	2.2E+18	2.2E+18	2.2E+18
N_V (cm ⁻³)	1.5E+19	2.9E+19	1.8E+19	1.8E+19	1.8E+19
$\nu_{t,e}$ (cm/s)	1.0E+07	1.0E+07	1.0E+07	1.0E+07	1.0E+07
$\nu_{t,h}$ (cm/s)	1.0E+07	1.0E+07	1.0E+07	1.0E+07	1.0E+07
μ_e (cm ² /Vs)	100	100	10	0.8	8.4
μ_h (cm ² /Vs)	25	25	10	0.8	8.4
N_a/N_d (cm ⁻³)	5.0E+16	5.0E+16	8.0E+17	1.0E+19	3.4E+20

Table 4.4 Additional SCAPS parameters. Values for the reference device are shown without parenthesis while RbF PDT values are within parenthesis.

	$E_V+0.58\text{eV}$	$E_V+0.98\text{eV}$	Bandtails
σ_e (cm ²)	1.0E-13 (1.0E-13)	1.0E-14 (1.0E-14)	1.0E-14 (1.0E-14)
σ_h (cm ²)	6.0E-17 (6.0E-17)	1.0E-14 (1.0E-14)	1.0E-14 (1.0E-14)
E_t (eV)	$E_V+0.58$ ($E_V+0.58$)	$E_V+0.98$ ($E_V+0.98$)	NA
kT^* (eV)	NA	NA	0.112 (0.057)
N_t (cm ⁻³)	1.0E+14 (6.0E+14)	2.7E+15 (7.0E+15)	5.0E+16 (3.0E+16)

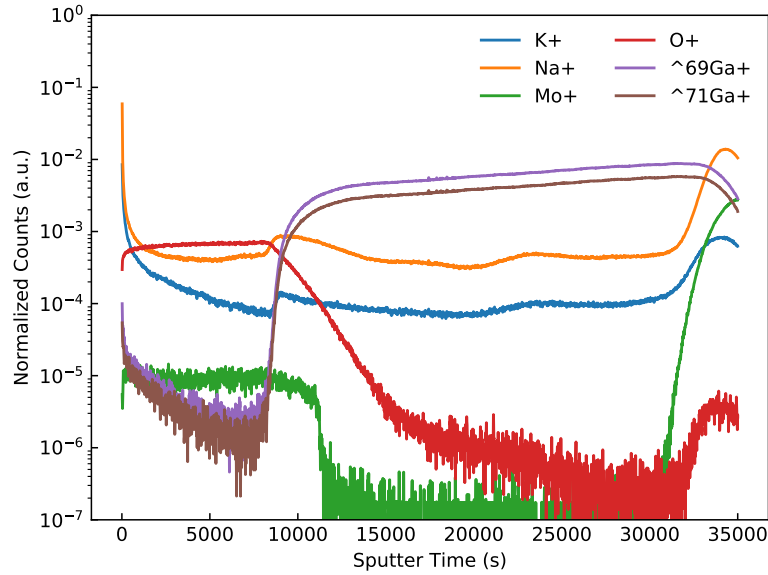


Figure 4.8 TOF-SIMS depth profiles for the as-deposited sample. O+ and Mo+ signals are included to provide boundaries for the absorber layer. Notice the two Ga isotopes track each other closely.

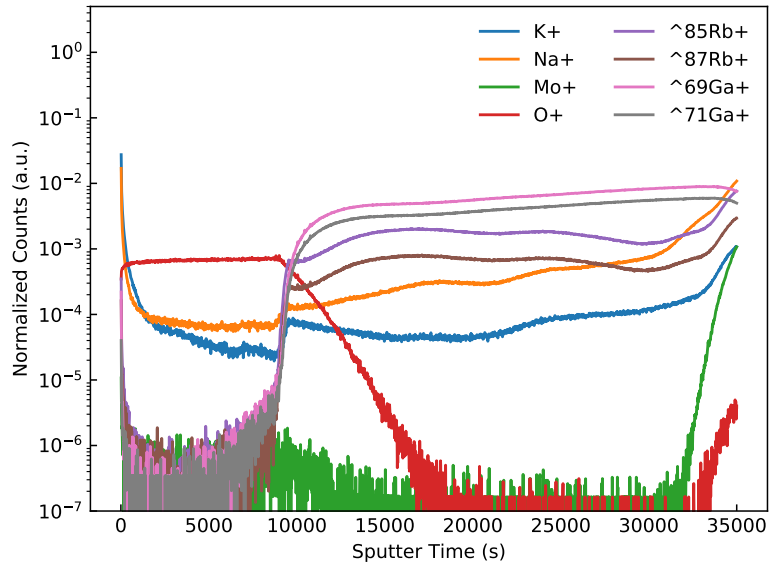


Figure 4.9 TOF-SIMS depth profiles for the RbF PDT sample. The Rb isotopes track each other well and have a different shape than the Ga signal. This indicates that the signal truly is Rb and not the possible GaO mass interference.

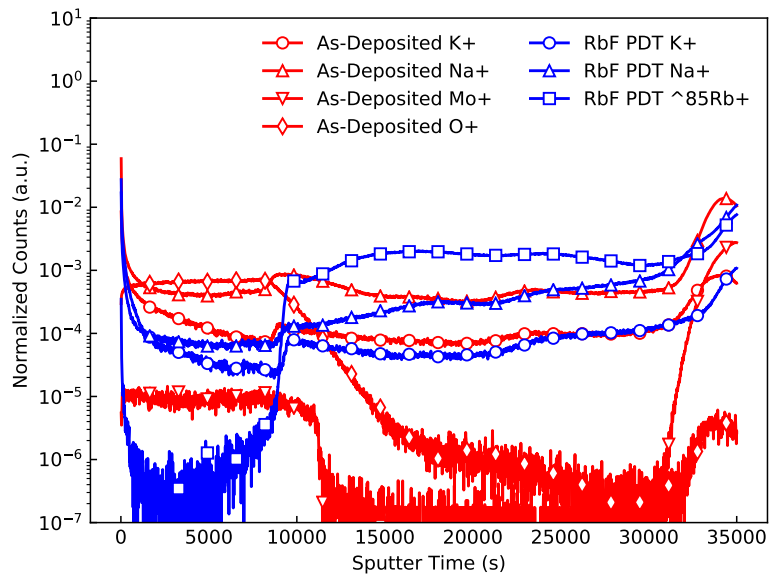


Figure 4.10 Comparison of the TOF-SIMS profiles for the as-deposited (red) and RbF PDT (blue) samples. Na appears to be partially displaced by Rb near the junction while K is relatively untouched.

CHAPTER 5

STABILITY OF $\text{Cu}(\text{In}_x\text{Ga}_{1-x})\text{Se}_2$ SOLAR CELLS UTILIZING RbF POST-DEPOSITION TREATMENT UNDER A SULFUR ATMOSPHERE

Paper Submitted to *Advanced Energy and Sustainability Research*

Jake Wands¹, Alexandra Bothwell³, Polyxeni Tsoulka⁵, Thomas Lepetit⁵, Nicolas Barreau⁵, Angus Rockett¹

5.1 Abstract

Alkali halide post-deposition treatments (PDTs) have become a key tool to maximize device efficiency in $\text{Cu}(\text{In}_x\text{Ga}_{1-x})\text{Se}_2$ (CIGS) photovoltaics. RbF PDTs have emerged as a potential alternative to the more common Na- and K-based techniques. This study utilizes temperature-dependent current voltage (JVT) measurements to study the impacts of a unique RbF PDT performed in a S atmosphere. In addition, the samples were measured before and after six months of storage in a desiccator to study device stability. A reference sample and a RbF+S PDT sample both showed the development of a rear contact barrier after aging. The barrier height of the contact barrier was higher for the RbF+S PDT sample leading to decreased current in forward bias. Series resistance was also higher in the RbF+S PDT device which led to lower fill factor. However, after aging the reference sample had a larger decrease in open-circuit voltage (V_{OC}). Ideality factor measurements suggest Shockley-Read-Hall recombination dominates both samples. V_{OC} vs temperature and a temperature-dependent activation energy model were used to calculate diode activation energies for each sample condition. Both techniques produced similar values that indicate recombination primarily occurs within the bulk absorber.

5.2 Introduction

$\text{Cu}(\text{In}_x\text{Ga}_{1-x})\text{Se}_2$ (CIGS) photovoltaics are one of the most successful thin-film technologies, with a record cell efficiency of 23.4% [26]. Key to the performance of modern CIGS devices is the use of alkali halide post-deposition treatments (PDTs) [59]. These treatments most commonly utilize Na or K as the alkali metal, however Rb and Cs have also shown potential benefits [35, 48]. RbF has received increased attention in recent years due to potential open-circuit voltage (V_{OC}) improvements over Na and K [25]. However, there are still questions about the stability of RbF PDT devices which need to be addressed before commercial use. In addition, PDT treatments are often performed in a Se atmosphere and little study into the influence of other chalcogens on device performance has been conducted [60].

⁵Nantes Université, CNRS, Institut des Matériaux de Nantes Jean Rouxel, IMN, F-44000 Nantes, France

In this work we report the aging effects of a device with RbF PDT performed in a S atmosphere compared to an untreated reference, investigated using temperature-dependent current-voltage (JVT) measurements. Series resistance was found to contribute to reduced fill factor (FF), and the effect grew larger over time. A back barrier, modeled as a second diode with reverse polarity, was shown to form in both devices, although the barrier height was greater in the RbS PDT sample. Each sample indicates that bulk recombination via a Shockley-Read-Hall (SRH) mechanism dominated recombination. The PDT proved to be an effective method of improving V_{OC} , however the efficiency suffered after aging. Improving the long-term stability will be necessary for the commercial viability of this technique.

5.3 Experimental Methods

The samples used in this study were complete solar cell devices with a layer stack consisting of: soda-lime glass/Mo/CIGS/PDT/CdS/ZnO/ZnO:Al/metallic grids, where PDT refers to a post-deposition treatment step performed between the CIGS and CdS depositions. The reference device received no PDT step while a RbF+S PDT was used in the second device. For the remainder of this paper these samples will be referred to as Ref and RbS PDT, respectively. The CIGS absorber layer was deposited by a three-stage co-evaporation process and designed to achieve a graded bandgap, higher at the front and rear. The final film composition was copper poor with a ratio of copper to group III elements of 0.95. The PDT was performed by co-evaporation of elemental sulfur (120 nm/min) and RbF (3 nm/min) at a substrate temperature of 350 °C to achieve a 15 nm thick layer. CdS was added by chemical bath deposition and the ZnO/ZnO:Al bilayer was rf-sputtered. Finally, electron beam evaporation was used to deposit the metallic grids through a shadow mask. More details on the device fabrication process can be found in [60]. Device measurements were performed on the samples shortly after deposition (referred to as fresh) as well as after six months storage in a desiccator in the dark (referred to as aged). No light soaking procedure was used.

External quantum efficiency (EQE) spectra were measured from 300-1400 nm using an Oriel 200 system with no external illumination or voltage bias applied. JVT experiments were performed from 350 K to 180 K in 10 K increments. The voltage was swept from -0.5 V to 2 V with the current limited to 800 mA. A solar simulator producing a simulated AM1.5 spectrum calibrated to 100 mW cm⁻² was used for illuminated measurements. Light and dark data were compared to detect light-dependent changes in the device and bias-dependent collection. JVT measurements were taken on each device immediately after manufacture and six months later after storage in a desiccator.

To extract the J_0 and n values, the impacts of R_{SH} and R_S resistance must be accounted for. This was done by first calculating the differential resistance (dV/dJ) for each JV curve. The region of the dV/dJ curve with a linear, negative slope on a semi-log plot is dominated by the resistance of the main diode.

Without including these, the ideality factor is overestimated with a corresponding error in reverse saturation current. It is important where this region covers a narrow voltage and current range to account simultaneously for the series and shunt resistances. An example dV/dJ curve is presented in Appendix Figure 5.10. A linear equation was fit to the main diode region of the dV/dJ curve and used to calculate dV/dJ as a function of voltage. The voltage step between data points, dV , was divided by dV/dJ to calculate the dJ curve for the main diode. Finally, the dJ values were integrated over the desired voltage range to produce the main diode JV curve. J_0 and n parameters were calculated from the intercept and slope, respectively, of a linear curve fit to the data on a semi-log plot [4].

5.4 Results and Discussion

Device performance parameters at 300 K are provided in Table 5.1 along with the change in value after the six-month period. When the samples were fresh V_{OC} improved after RbF+S PDT in agreement with many existing studies on RbF PDTs, indicating that the presence of S did not negate this beneficial outcome [25, 31, 35, 60]. Short-circuit current (J_{SC}) was similar between the two samples with the RbS PDT experiencing a minor drop. FF declined slightly in the fresh RbS PDT device relative to the Ref sample. The impact of RbF PDT on FF is unclear in the literature, with some results showing little effect or small increases [25, 31, 35]. A previous study on the RbS PDT also showed a small decrease in FF, but further investigations may be necessary to be definitive [60].

Table 5.1 JV parameters, R_s , and its impact on FF before and after aging for each device.

		V_{OC} (mV)	J_{SC} (mA/cm ²)	FF (%)	η (%)	R_s ($\Omega \cdot \text{cm}^2$)	FF ₀ (%)	FF Deficit (abs.%)
Ref	Fresh	678	32.8	74.4	16.5	0.92	77.8	3.5
	Aged	622	32.7	69.3	14.1	1.42	74.9	5.6
	Change	-56	-0.1	-5	-2.4	+0.5		+2.1
RbS PDT	Fresh	712	32.2	72.5	16.6	1.40	77.4	4.9
	Aged	679	30.0	63.1	12.9	2.30	70.2	7.1
	Change	-33	-2.2	-9	-3.7	+0.9		+2.2

While each device saw a drop in overall efficiency after aging, the source of decline was different. The Ref sample degraded most in V_{OC} relative to the PDT sample. A modest decline in J_{SC} was seen in the Ref sample while the RbS PDT device had a more noticeable decrease. External quantum efficiency (EQE) measurements before and after aging show that the Ref device experienced relatively small declines across the measurement range (Figure 5.1). The RbS PDT device lost current primarily at higher energies, which may indicate reduced collection near the junction.

The Ref sample lost 5 abs.% of FF, which is significant but less than the 9 abs.% drop in the RbS PDT sample. R_S had a notable impact on the FF of each device, particularly after aging and at low temperatures. The effect of series resistance can be deconvoluted from FF using Equation 5.1 where FF_0 is the FF with series resistance removed and FF_S is the measured FF [61]:

$$FF_0 = FF_S(1 - (J_{SC}/V_{OC})R_S)^{-1} \quad (5.1)$$

The difference between these two values is referred to here as the FF deficit. FF deficits for each device can be found in Table 5.1 and show a notable increase after aging. Since the RbS PDT device had a larger increase in R_S after aging, it also saw a larger increase in FF deficit. Similar calculations were performed for the effect of R_{SH} on FF, but the R_{SH} values for each device were large enough to make the impact negligible.

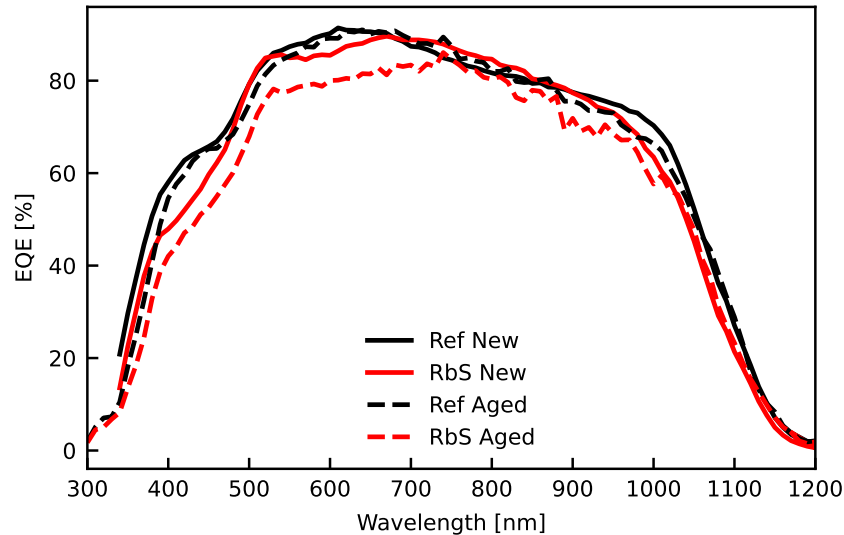


Figure 5.1 EQE measurements show reduction at low energies (Ref) and high energies (RbS PDT), respectively after aging.

Semi-log JV plots at 200 K and 300 K in the dark are shown in Figure 5.2 (for complete JVT plots see Appendix Figure 5.11). A notable development was the formation of a low-temperature blocking contact after aging which was not present in the fresh samples. This is most obvious in the 200 K plots where the current at forward bias voltages above 1 V was reduced after aging, indicating a barrier had developed.

A roll-over effect in CIGS solar cells has previously been attributed to a Schottky diode forming at the back contact with opposite polarity to the main junction [17, 21, 50]. The applied bias is therefore split between the two diodes and the series resistance, as depicted in the equivalent circuit diagram in Figure 5.3a. Since the current through both diodes must be the same, the main diode bias, V_m , can be

estimated using the full device current, and the main diode JV curve calculated with the dV/dJ analysis. The bias across the back diode can then be calculated by [62]:

$$V_b = V_{applied} - V_m - JR_S \quad (5.2)$$

where $V_{applied}$ is the bias across the whole device and R_S is the series resistance.

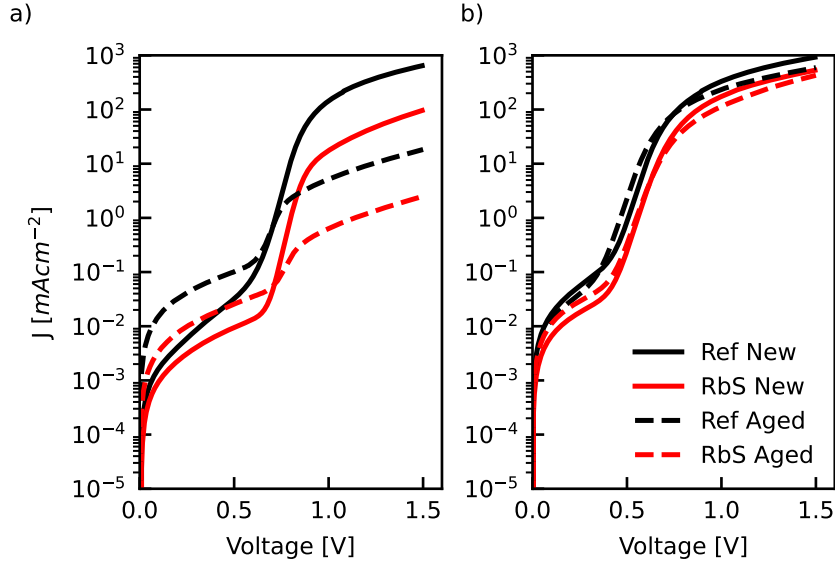


Figure 5.2 Semi-log JV curves measured at a) 200 K and b) 300 K for each device before and after aging.

The voltage split between V_m and V_b can be found in Appendix Figure 5.12. Now the JV curve of the back diode can be plotted as J vs V_b as seen in Figure 5.3b. Because the back diode has opposite polarity the plot depicts reverse leakage current when the net current is positive (first quadrant of the JV plot).

The Ref device exhibited higher leakage current in the blocking diode compared to the RbS PDT sample. Since the back diode blocks current flow, the high leakage current in the Ref sample was beneficial. In other words, the aging process produced a stronger blocking diode in the RbS PDT device.

The back barrier height for each device can be estimated using [21]:

$$J_{limit} = A^*T^2 \exp(-q\Phi_b/(kT)) \quad (5.3)$$

Where J_{limit} is the current density at which roll-over begins, T is temperature, q is the electronic charge, k is the Boltzmann constant, Φ_b is the back barrier height, and A^* is the Richardson constant described by:

$$A^* = (4\pi qm^*k^2)/h^3 \quad (5.4)$$

In this case m^* is the effective mass of holes and h is Planck's constant. The barrier height was calculated to be 381 meV and 402 meV for the Ref and RbS PDT devices, respectively.

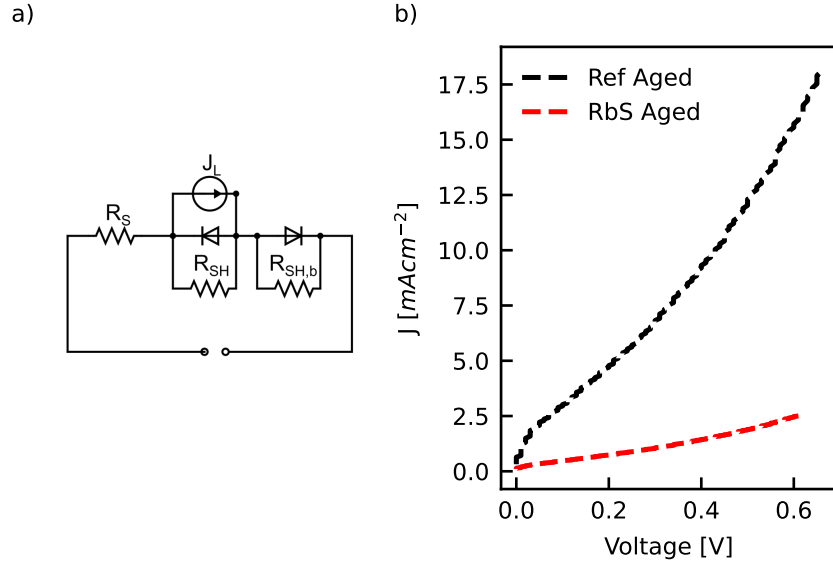


Figure 5.3 a) Equivalent circuit diagram depicting the reverse polarity rear diode and b) JV curves for the reverse polarity back diode in the aged devices at 200 K.

Although the cause of this increased barrier in the RbS PDT device is not known, time-of-flight secondary ion mass spectroscopy (TOF-SIMS) depth profiles of the aged samples (included in Appendix) showed a spike in alkali elements at the back contact. The Ref sample had a large increase in Na and K at the rear contact, while the increase in the RbS PDT device was reduced. The Na and K likely diffused into the sample from the glass substrate. The RbS PDT device had a significant spike in Rb at the back contact which appears to have excluded Na and K ions from the region. This ion exchange has been observed previously and is confirmed in the samples studied here [31, 33].

Ideality factor vs temperature is shown for each device in Figure 5.4 extracted after accounting for the series and shunt resistances. The fresh devices both showed ideality factors in the range of 1.4-1.5 at temperatures above 250 K. These values are indicative of SRH recombination through states that are located between the band-edge and mid-gap [4]. Before aging there was a gradual rise in ideality factor at low temperatures, which was more pronounced in the Ref sample than the RbS PDT sample. The ideality factor rise above two in the Ref sample could result from tunneling recombination or interface effects [4, 52]. The aging process had relatively small impacts on ideality factor of the Ref device and suggests SRH recombination still dominated for $T > 250$ K. In the RbS PDT device the ideality factor was consistently higher after aging, although the values remained under two for most of the temperature range.

JVT data can be further analyzed to calculate the diode activation energy (E_a) using the reverse saturation current density (J_0) as a function of temperature [63].

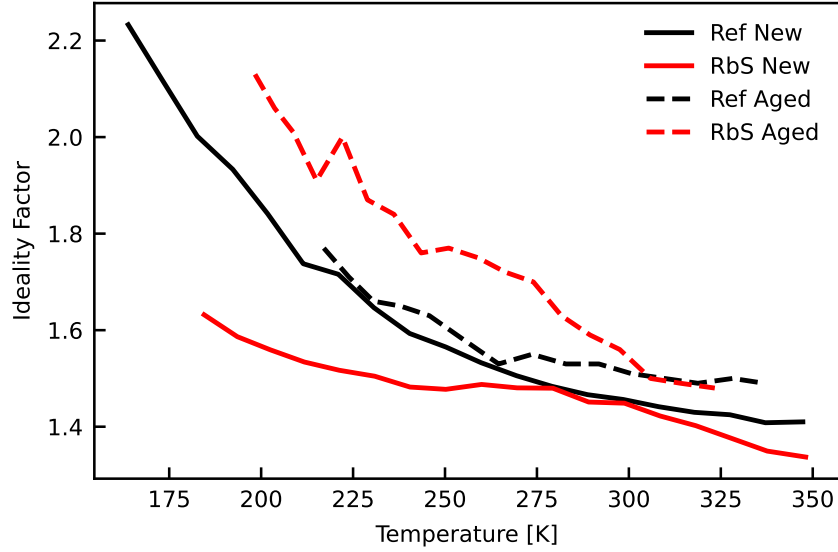


Figure 5.4 Ideality factor as a function of temperature for each device.

The activation energy provides information about the dominant recombination mechanism in a device. If $E_a \approx E_g$, recombination primarily occurs within the bulk absorber, while $E_a < E_g$ occurs when interface recombination is dominant. While this technique is common in literature, activation energy is typically calculated from the slope of a $\ln(J_0)$ vs $1/kT$ or $\ln(J_0/T^{2.5})$ vs $1/kT$ plot. These models may be appropriate in some samples, but they assume that ideality factor and activation energy are temperature independent. As seen in Figure 5.4, the ideality factor in these devices has a moderate temperature dependence which needs to be accounted for.

A more robust analysis of J_0 can be performed by considering temperature dependent ideality factors [5].

$$J_0 = J_{00} \exp(-E_a / (n(T)kT)) \quad (5.5)$$

and

$$n(T) \ln(J_0 / J_{00}) = -E_a / (kT) \quad (5.6)$$

Based on Equation 5.6 a plot of $n(T) \ln(J_0 / J_{00})$ vs $1/kT$ will yield the activation energy, as seen in Figure 5.5. The activation energy values are listed in Table 5.2. Each activation energy was close to the CIGS bandgap (≈ 1.15 eV), which generally indicates that recombination in the bulk dominates current flow rather than at interfaces. This may indicate that the ideality factor values above two at low temperature were related to tunneling effects rather than interface recombination. The slight decrease in activation energy after aging for the Ref device may suggest that interface recombination begins to have

more influence after aging.

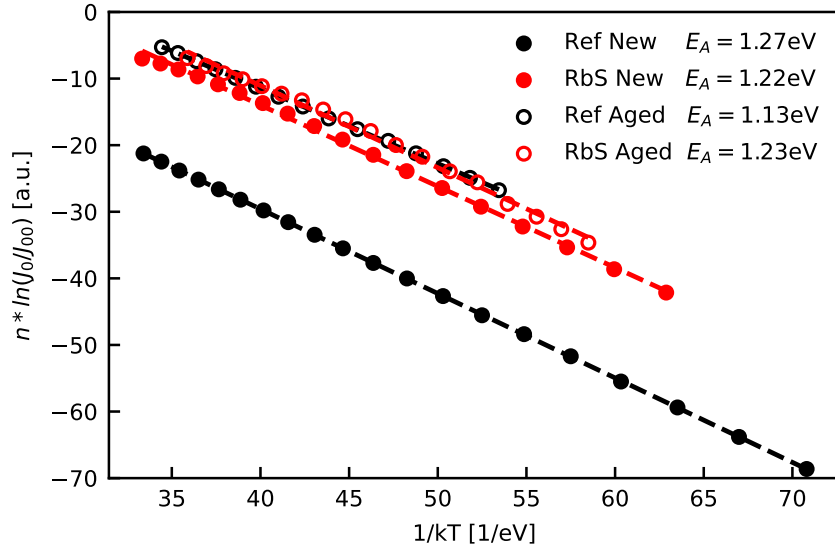


Figure 5.5 Arrhenius plot of $n \cdot \ln(J_0/J_{00})$ vs $1/kT$ with linear fits to the data. The activation energy is calculated from the slope of the fit (dashed lines).

To verify that the ideality factor is the only additional temperature dependent variable, Equation 5.6 can be rearranged:

$$\ln(J_0/J_{00}) = -E_a/(n(T)kT) \quad (5.7)$$

Using Equation 5.7, an additional plot of $\ln(J_0/J_{00})$ vs $1/n(T)kT$ can be used which should yield the same activation energy if $n(T)$ is the only temperature dependent term.

As seen in Figure 5.6 this method did not produce the same activation energies, which suggests that there is an additional temperature dependence which impacts the analysis. This can be accounted for by introducing a temperature dependent activation energy [5, 64]:

$$E_a(T) = E_{a,0} - \alpha T \quad (5.8)$$

Where $E_{a,0}$ is the 0 K activation energy and α is the temperature coefficient. By substituting Equation 5.8 into Equation 5.5 a new formula can be used for analysis:

$$\ln(J_0/J_{00}) = -E_{a,0}/(n(T)kT) + \alpha/(n(T)k) \quad (5.9)$$

Now a plot of $\ln(J_0/J_{00}) - \alpha/n(T)k$ vs $1/n(T)kT$ will provide the 0 K activation energy which should match the value found using Equation 5.6. To create this plot the values of α and J_{00} must be calculated through

an iterative process using two more equations:

$$\ln(J_0) - \alpha/(n(T)k) = -E_{a,0}/(n(T)kT) + \ln(J_{00}) \quad (5.10)$$

and

$$n(T) * \ln(J_0/J_{00}) = -E_{a,0}/(kT) + \alpha/k \quad (5.11)$$

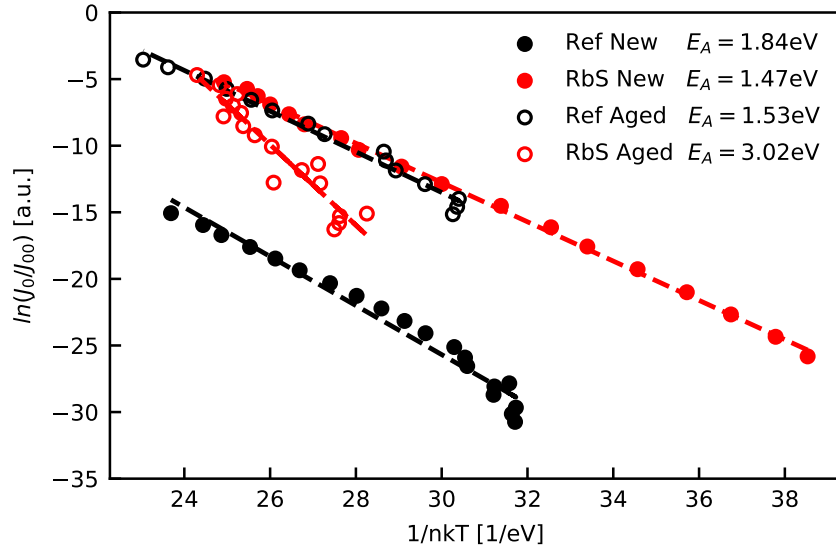


Figure 5.6 Modified Arrhenius plot to determine whether ideality factor is the only temperature-dependent variable. The slope of the linear fits results in activation energies that don't match those of Figure 5.5.

Using Equation 5.10 a plot of $\ln(J_0) - \alpha/n(T)k$ vs $1/n(T)kT$ can be created with an initial guess of α . The intercept is then used to calculate an estimate of J_{00} which can be inserted into Equation 5.11. Plotting $n(T) * \ln(J_0/J_{00})$ vs $1/kT$ from Equation 5.11 will then provide a new value of α from the intercept. This process is repeated until both $E_{a,0}$ and α are consistent between the two plots, at which point the values of J_{00} and α can be used for further calculations.

Using the calculated values of α and J_{00} with Equation 5.9, the 0 K activation energy was determined for each sample (Figure 5.7). The activation energies were in good agreement with those found from Figure 5.5, improving confidence in the temperature dependent activation energy model. The values for J_{00} , α , and E_a are listed in Table 5.2. Two primary mechanisms are identified as the sources of α in the literature: potential fluctuations and temperature-dependent bandgaps [5, 64]. If band-to-band recombination in the bulk is a dominant mechanism, changes in the bandgap will necessarily affect the activation energy. CIGS has been shown to have a temperature dependent bandgap, likely contributing to

α in these samples. Potential fluctuations can arise from sources such as variations in alloy composition, lattice strain, and compensating defects. They have been shown to affect α particularly when the magnitude of fluctuations is greater than kT [65]. Assuming that the temperature dependence of the bandgap did not change significantly after aging, the changes in α after aging were likely due to increased potential fluctuations. Several studies have shown potential fluctuations to have negative impacts on device performance, particularly V_{OC} [35, 38]. Since α had a greater increase in the Ref sample this is a possible contributor to its larger decline in V_{OC} after aging.

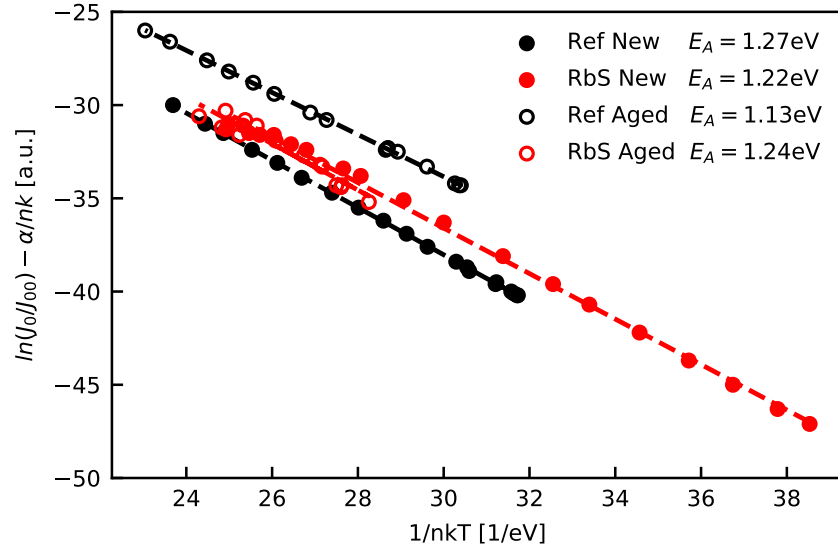


Figure 5.7 Arrhenius plot using the temperature-dependent activation energy model. Activation energies calculated from the slope of the linear fits agree well with Figure 5.5.

Table 5.2 Calculated values from the temperature-dependent activation energy model.

		J_{00} (mA/cm ²)	α (meV/K)	E_a (eV)
Ref	Fresh	3.36×10^2	1.82	1.27
	Aged	5.03×10^{-3}	2.90	1.13
RbS PDT	Fresh	1.56×10^{-3}	3.00	1.22
	Aged	7.23×10^{-4}	3.30	1.23

Using data from Table 5.2, J_0 values were calculated from Equation 5.9 and plotted along with the experimentally determined J_0 data (Figure 5.8). Because J_0 is associated with the magnitude of recombination, some conclusions about recombination in the devices can be inferred from Figure 5.8.

While the J_0 values are close for each condition at most temperatures, the fresh RbS PDT device had the

lowest J_0 , particularly at low temperature. This indicates that recombination was lowest in that device, and that the PDT was effective in reducing recombination initially. This is also consistent with the increased V_{OC} value in the fresh RbS PDT vs. fresh Ref device. The reduction in J_0 may be related to reduced trap density which has been reported in several defect studies of RbF treated CIGS. Karki et al. used deep-level optical spectroscopy (DLOS) to find that the concentration of a $E_V+0.99$ eV trap to be 1.3x higher in untreated CIGS compared to RbF PDT [31]. Helder et al. employed deep-level transient spectroscopy (DLTS) to observe that RbF PDT reduced the concentration of an $E_V+0.4$ eV trap by a factor of 3-4x [66]. After aging the J_0 vs T curves converged and there was less separation between the two devices. Defect studies are needed to determine whether increased J_0 after aging is related to an increase in defect concentration.

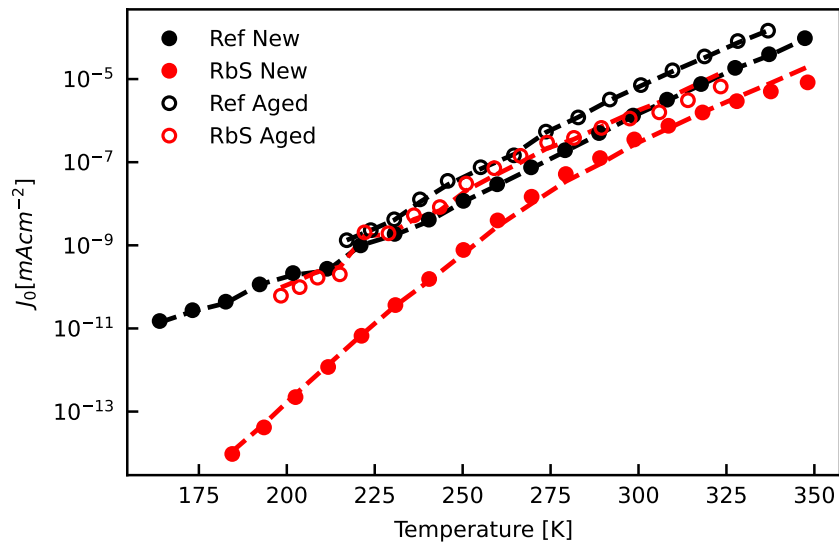


Figure 5.8 Comparison of experimental data (dots) with modeled (dashed lines) J_0 vs T plots using Eq. 9 and data from Table 5.2. The modeled data agrees well with experimental results.

Activation energy can also be calculated from the interpolated value of V_{OC} at $T=0$ K from the V_{OC} vs T plot (Figure 5.9). Using this method, all samples had activation energies near the values calculated using the J_0 data. Agreement between multiple analysis techniques of activation energies augments confidence in these results and supports the conclusion that bulk recombination is the dominant mechanism at play in these devices.

5.5 Conclusion

A unique RbF+S post-deposition treatment for CIGS thin-film photovoltaics was tested for performance and stability against a standard reference device. After six months in a desiccator both

devices showed the formation of a back contact barrier. The barrier is theorized to be a Schottky diode in reverse polarity with respect to the main diode, and the barrier height was calculated to be higher in the RbS PDT device. Each device also demonstrated an increase in series resistance, which reduced FF. However, the effect was much more significant in the RbS PDT device. EQE measurements also showed greater decline in bulk collection in the RbS PDT device after aging, primarily for carriers generated by higher energy photons. JVT measurements were used to analyze the ideality factor and J_0 . The ideality factor values in both devices suggested SRH recombination is the dominant mechanism, particularly at normal operating temperatures. A J_0 model which accounts for temperature-dependent ideality factors and activation energies was used to calculate the diode activation energy. The diode activation energies were all near the CIGS bandgap which suggests that recombination primarily occurred in the bulk absorber. These values were supported by similar results from V_{OC} vs temperature plots. The J_0 analysis indicates that recombination was initially reduced after PDT, but after aging the benefits became negligible. Overall, while the RbS PDT provides improved V_{OC} and initial efficiency, the long-term performance requires further study before becoming a commercially viable option.

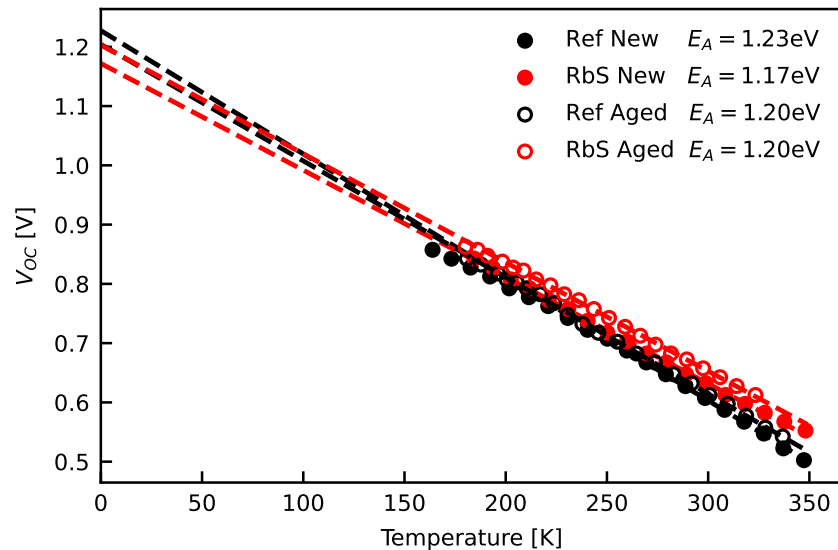


Figure 5.9 V_{OC} vs T plots with linear extrapolation to 0 K to calculate the activation energy. Linear fits were applied to data above 250 K to account for the low-temperature roll-over effect.

5.6 Acknowledgements

This work was supported in part by the U.S. Department of Energy's Office of Energy Efficiency and Renewable Energy (EERE) under Solar Energy Technologies Office (SETO) Award Number DE-EE0008755 and in part by the National Renewable Energy Laboratory, operated by Alliance for

Sustainable Energy, LLC, for the U.S. Department of Energy (DOE) under Contract DE-AC36-08GO28308, in part by the U.S. Department of Energy Office of Energy Efficiency and Renewable Energy Solar Energy Technologies Office. The views expressed in the article do not necessarily represent the views of the DOE or the U.S. Government. The U.S. Government retains and the publisher, by accepting the article for publication, acknowledges that the U.S. Government retains a nonexclusive, paid-up, irrevocable, worldwide license to publish or reproduce the published form of this work, or allow others to do so, for U.S. Government purposes. This material makes use of the TOF-SIMS system at the Colorado School of Mines, which was supported by the National Science Foundation under Grant No. 1726898.

5.7 Appendix

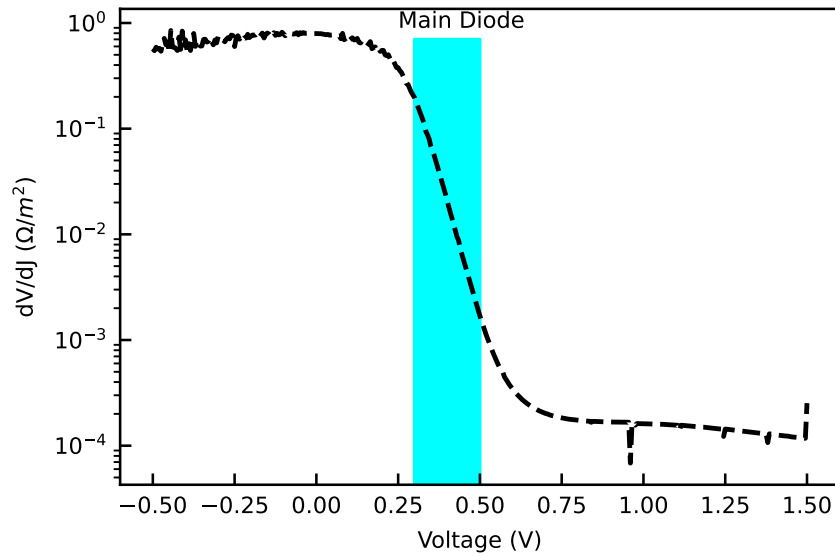


Figure 5.10 Example dV/dJ curve for the Ref device at 300 K. The highlighted portion of the curve is the linear region which was fit to produce the dV/dJ behavior of the main diode.

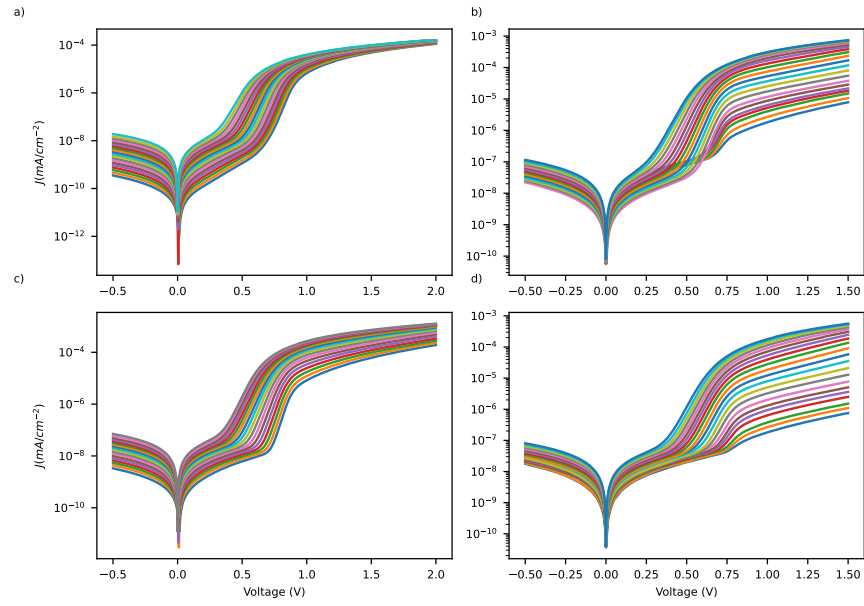


Figure 5.11 Dark JVT curves from 180 K to 350 K for the a) fresh Ref, b) aged Ref, c) fresh RbS PDT, and d) aged RbS PDT devices.

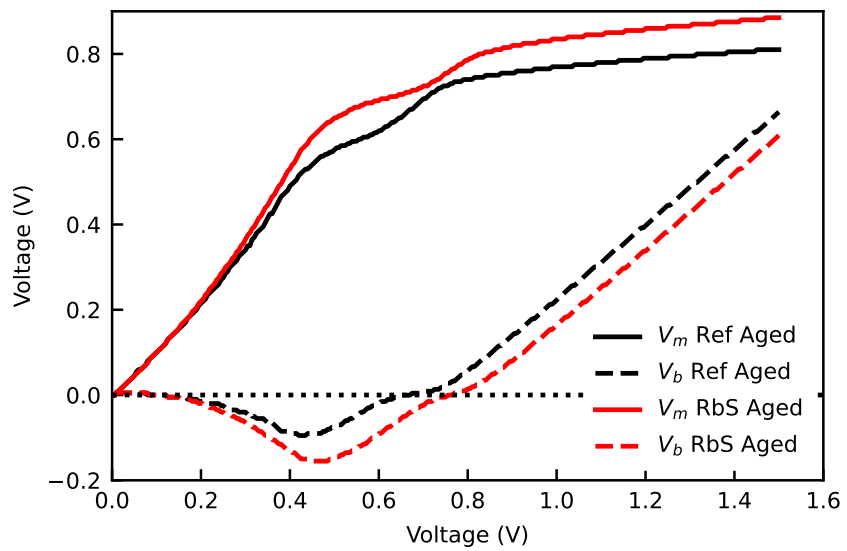


Figure 5.12 Voltage split between the main diode and the reverse polarity back diode for each aged device.

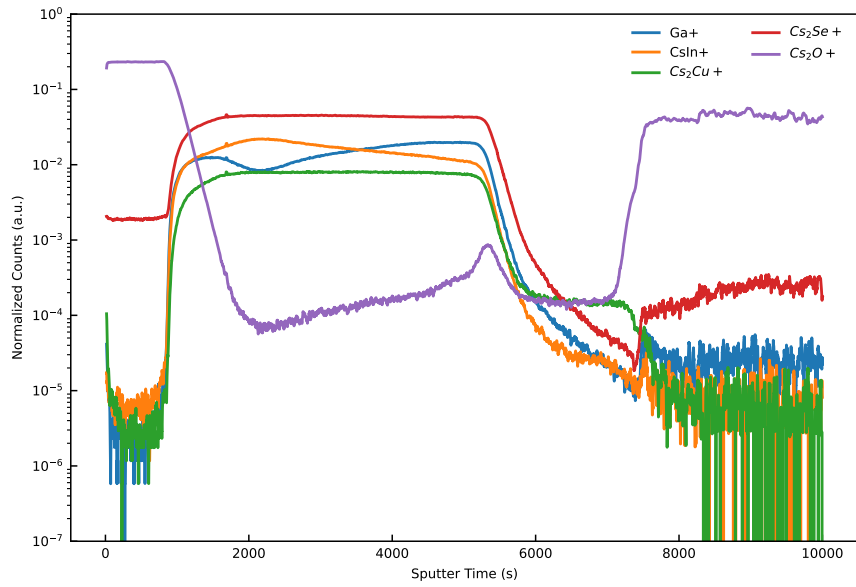


Figure 5.13 TOF-SIMS depth profiles for the Ref device. All measurements used a 1 keV Cs sputter beam was used at 90 nA of current along with a 30 keV Bi₃ primary beam run at 0.7 pA.

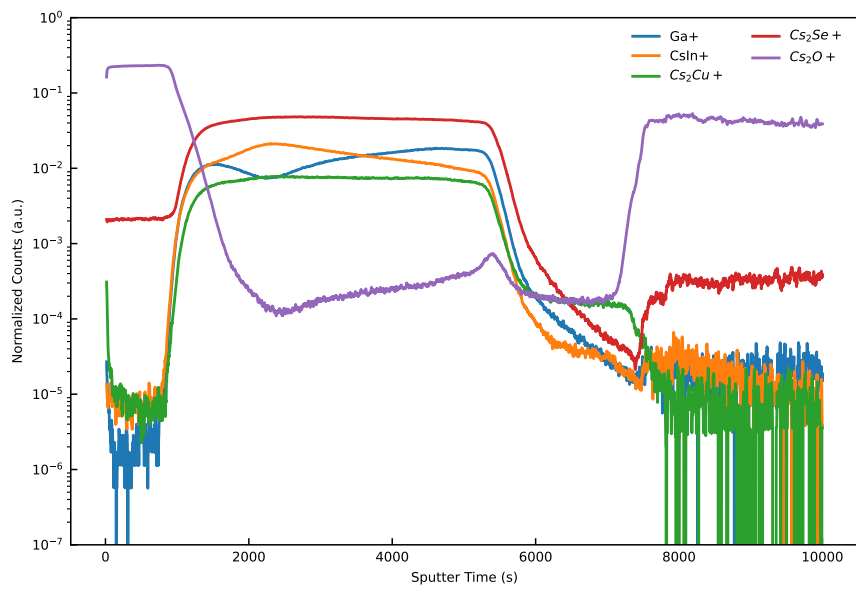


Figure 5.14 TOF-SIMS depth profiles for the RbS PDT device.

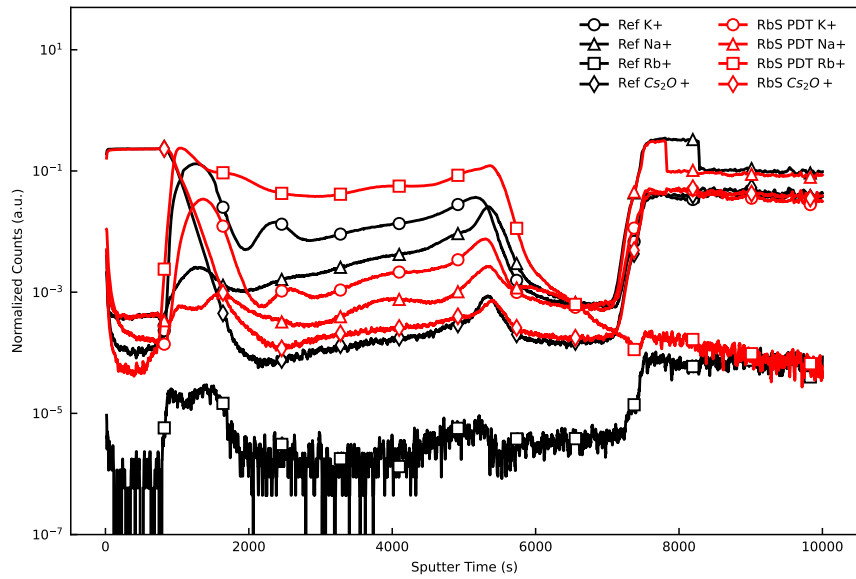


Figure 5.15 TOF-SIMS comparison of alkali elements between the two devices. There is a noticeable drop in Na^+ and K^+ signal in the RbS PDT sample suggesting that Rb is reducing the concentration of other alkalis.

CHAPTER 6

VOLTAGE-DEPENDENT COLLECTION EFFICIENCY LOSSES IN RbF TREATED $\text{Cu}(\text{In}_x\text{Ga}_{1-x})\text{Se}_2$

Paper Submitted to *Progress in Photovoltaics: Research and Applications*

Jake Wands¹, Alexandra Bothwell³, Polyxeni Tsoulka⁵, Thomas Lepetit⁵, Nicolas Barreau⁵, Angus Rockett¹

6.1 Abstract

$\text{Cu}(\text{In}_x\text{Ga}_{1-x})\text{Se}_2$ (CIGS) thin-film photovoltaics commonly use RbF-based post deposition treatments (PDTs) to increase efficiency. This study analyzes the effects of voltage-dependent collection efficiency (η_C) on the performance of two unique RbF PDTs. A standard reference (Ref) sample was compared to samples treated with RbF+S (RbS PDT) and RbF+In+S (RIS PDT). The PDT devices demonstrated improved open-circuit voltage (V_{OC}) compared to the Ref sample. η_C was lower at V_{mp} in the PDT devices which led to greater losses in V_{OC} , fill factor, and maximum power. A variety of measurements were used to investigate the cause of η_C losses. While several factors likely contributed, reduced depletion width provided the best explanation of the loss trends. High Ga/(Ga+In) gradients near the heterojunction, which are used to reduce interface recombination, may also contribute to η_C . This presents a trade-off between collection efficiency and interface recombination—which requires the gradient—that must be optimized for maximum power output.

6.2 Introduction

Optimizing performance of photovoltaic (PV) devices requires effective collection of photogenerated carriers. For polycrystalline thin-film PV technologies carrier collection can suffer significant loss due to relatively short carrier diffusion lengths [67–69]. The electric field in the depletion region is vital in separating electron-hole pairs and ensuring that carriers reach the contacts. As forward bias increases, the depletion region narrows, decreasing the effectiveness of charge separation and collection. This results in lower current density under forward bias than the measured short-circuit current density (J_{SC}), and therefore a reduction in fill factor (FF) and device efficiency. In current density-voltage (JV) curve analysis, voltage-dependent collection efficiency (η_C) losses have similar characteristics to shunt resistance (R_{SH}) losses. The primary difference is that R_{SH} losses are also present in dark JV curves, while voltage-dependent collection only appears under illumination [4, 67]. Identification of how dominant the voltage-dependent collection losses mechanism is can provide guidance for improving performance in thin-film PV devices.

Despite being a leading thin-film PV technology with a record efficiency of 23.4%, $\text{Cu}(\text{In}_x\text{Ga}_{1-x})\text{Se}_2$ (CIGS) solar cells are not immune to voltage-dependent collection losses [18, 26, 70–72]. Further study into this loss mechanism is beneficial for devices with novel alkali-halide post-deposition treatments (PDTs). PDTs utilizing RbF have become popular due to the increased open-circuit voltage (V_{OC}) measured in many studies [25, 31, 34, 35, 39]. In this work two unique RbF-based PDTs are analyzed for voltage-dependent collection efficiency losses and compared to a reference device with no PDT. The first PDT uses RbF deposited under a sulfur atmosphere as opposed to the more typical selenium atmosphere. The second PDT is RbF+In, also deposited under a sulfur atmosphere [60]. While the PDT devices had greater V_{OC} than the reference sample, they also had lower η_C . This led to greater FF losses in the PDT devices. Several possible causes were explored with low depletion width providing the best explanation.

6.3 Experimental Methods

CIGS absorbers were grown by a co-evaporation technique from elemental sources following a 3-stage sequential process. During the first stage, In and Ga were co-evaporated under selenium excess flux onto the soda lime glass/Mo substrate heated to 375 °C. The composition of the resulting $(\text{In,Ga})_2\text{Se}_3$ films corresponded to a $\text{Ga}/(\text{Ga}+\text{In})$ ratio (GGI) of 0.4. During the second stage, Cu was supplied in Se excess while the substrate temperature was increased to 575 °C. This second stage ended when the growing film became over-stoichiometric in Cu (i.e. Cu-rich). Finally, In and Ga were supplied again in excess Se until the film turned Cu-poor. From this process, polycrystalline CIGS films with large grains and a V-shaped GGI profile throughout the absorber were formed [60].

The RbF+S PDT was performed by evaporating 15 nm of RbF at 3 nm/min in sulfur excess (120 nm/min) onto the surface of the CIGS film. The RbF+In+S PDT evaporated 15 nm of RbF at 3 nm/min and 20 nm of In at 4 nm/min under sulfur excess. Both treatments used a substrate temperature of 350 °C. All samples were then coated with a CdS layer using chemical bath deposition followed by an rf-sputtered ZnO/ZnO:Al window layer. Further information on device manufacture can be found in [60]. The reference, RbF+S PDT, and RbF+In+S PDT devices will be referred to as Ref, RbS PDT, and RIS PDT respectively.

JV measurements were performed on each device to analyze voltage-dependent collection efficiency. The current was limited to 800 mA as the voltage was swept from -0.5 V to 2 V. Illuminated measurements were performed using a solar simulator which produced a simulated AM1.5 spectrum calibrated to 100 mW/cm^2 with neutral density filters that reduced intensity to 50%. Using light levels below 1 sun decreases curvature induced by photocurrent (J_L) and aids analysis [67]. Previous work has shown η_C to be independent of illumination intensity, so the conclusions drawn in this study apply at 1 sun as well [67].

Series resistance (R_S) was calculated using the methods outlined in [4].

Capacitance-voltage (C-V) profiles were measured using an Agilent 4294A precision impedance analyzer. A measurement frequency of 40 kHz across a voltage range of -1.0 to +0.5 V was used.

Time-resolved photoluminescence (TRPL) was measured using pulsed laser excitation with 0.3-ps pulses and a 1.1 MHz repetition rate. An optical parametric amplifier-controlled excitation wavelength of 640 nm and a fluence of $1.3 \times 10^{12} - 1 \times 10^{14}$ photons/(cm²pulse) was used. Time-correlated single photon counting was utilized for data collection.

Time-of-flight secondary ion mass spectroscopy (TOF-SIMS) depth profiles were used to calculate GGI profiles. A 1 keV Cs sputter beam at 90 nA of current along with a 30 keV Bi₃ primary beam run at 0.7 pA was employed for analysis. The Ga and In profiles used for GGI calculations were measured in counts/second in the absence of an implant standard for calibrated concentrations. This is a reasonable approximation of the GGI ratio since the ionization energy for Ga and In are close and should result in similar ion yields [73, 74].

6.4 Results and Discussion

To illustrate the behavior of voltage-dependent collection, Figure 6.1 displays the illuminated JV curve and the dark curve shifted downward by J_{SC} ($J_{dark} - J_{SC}$) for the RbS PDT device. A device without voltage-dependent collection efficiency losses will follow the superposition principle which predicts that the two curves perfectly overlap. In the RbS PDT device a clear separation forms as the forward bias increases, indicating lost photocurrent. The illuminated curve has lower FF and V_{OC} than $J_{dark} - J_{SC}$ which will be quantified in the following analysis.

To properly calculate η_C , the JV curves must first be corrected for R_S by calculating the voltage across the junction [4, 67]:

$$V' = V - R_S J \quad (6.1)$$

where V' is the junction voltage, R_S is the series resistance, and J is the current density. A plot of current density vs junction voltage will now represent the JV curve without the influence of series resistance. Once V' has been determined η_C can be calculated as [18, 67, 70]:

$$\eta_C(V') = (J_2(V') - J_1(V')) / (J_{L01} - J_{L02}) \quad (6.2)$$

where J_1 and J_2 are the current densities at the two illumination conditions. J_{L01} and J_{L02} are the maximum photocurrents if perfect collection is achieved. J_{SC} values will be used as J_{L0} for all calculations in this study as there was little additional carrier collection in reverse bias and the light JV curves are consistent with the dark curves at low voltages and currents (c.f. Figure 6.1).

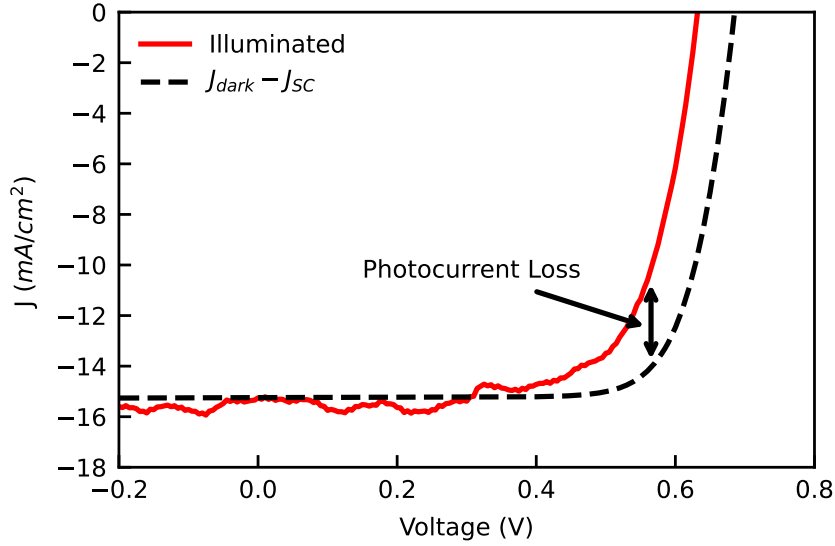


Figure 6.1 Illuminated and $J_{\text{dark}} - J_{\text{SC}}$ JV curves for the RbS PDT device demonstrates that the superposition principle is not followed. Noise is present in the illuminated curve although it does not affect the following analysis.

Figure 6.2 shows η_C as a function of voltage for each of the three devices. At the maximum power point the reference sample had an η_C of 95%, meaning that 5% of photogenerated current was not collected from the device. The RbS and RIS devices had η_C of 90% and 88% at the maximum power point, respectively. The significant decrease in collection efficiency in both PDT devices can help explain the FF loss in each device.

The JV curves can be corrected for η_C to quantify the impact on device performance. This can be done using two equations [67]:

$$J_m = J_{\text{dark}} - J_{L0}\eta_C \quad (6.3)$$

$$J_{\text{ideal}} = J_{\text{dark}} - J_{L0} \quad (6.4)$$

where J_m is the measured current, J_{dark} is the dark current, and J_{ideal} is the η_C corrected current. By solving Equation 6.3 for J_{dark} and substituting into Equation 6.4 the relationship becomes [67]:

$$J_{\text{ideal}} = J_m + J_{L0}\eta_C - J_{L0} = J_m + J_{L0}(\eta_C - 1) \quad (6.5)$$

Using Equation 6.5 the η_C corrected current can be calculated for each device and compared to $J_{\text{dark}} - J_{\text{SC}}$. Figure 6.3 compares the measured JV curve to the R_S corrected, η_C and R_S corrected, and $J_{\text{dark}} - J_{\text{SC}}$ curves for each sample. It is apparent in each sample that R_S had a small, yet noticeable, negative impact on the FF. However, this effect was overshadowed, particularly in the PDT devices, by the

large effect of η_C on FF. After correcting for η_C there was a dramatic increase in FF as well as a small increase in V_{OC} for all three devices with negligible effect on J_{SC} .

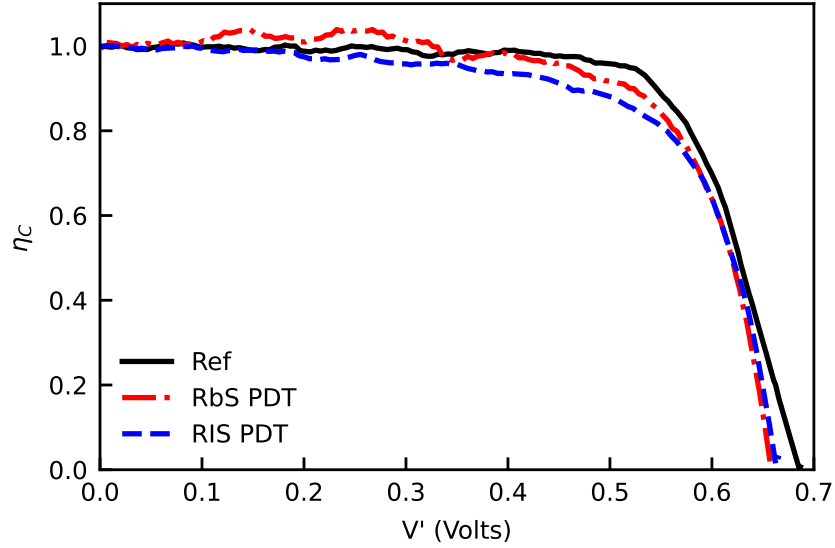


Figure 6.2 Voltage-dependent collection efficiency (η_C) as a function of junction voltage (V').

Table 1 lists the device performance parameters for each curve as well as the FF and V_{OC} losses due to R_S and η_C . Both PDT devices displayed improved V_{OC} over the Ref sample which is a common observation for CIGS subjected to a RbF PDT [25, 31, 34, 35, 39]. Despite having higher V_{OC} , the PDT devices also had greater ΔV_{OC} , which represents losses due to low η_C . Another way to state this is that the PDT processes improved the dark JV behavior more than the light behavior. While each device had a similar FF loss of 2% due to R_S , large differences emerged when correcting for η_C . The $\eta_C + R_S$ corrected FF was 4.9% higher in the Ref sample while the RbS PDT and RIS PDT sample fill factors increased 11% each. The RbS device, in particular, would have a FF of 81% based on the above corrections, which highlights the magnitude of losses which occurred in the PDT devices. It is clear that η_C is an important loss mechanism in these devices, and that the PDT devices experienced greater losses due to lower η_C .

Power vs voltage plots can also be used to observe the losses caused by R_S and η_C which are included in Table 1. Figure 6.4 shows the power plots for each device and emphasizes the impact on device performance. Maximum power in the $\eta_C + R_S$ corrected data was significantly higher in all three devices, although the PDT samples demonstrated a much larger increase.

To improve this loss mechanism, it is necessary to identify possible causes of low collection efficiency. Several sources can lead to voltage-dependent collection efficiency losses including low carrier lifetime, high recombination, composition gradients, and narrow depletion width [18, 67, 68, 70].

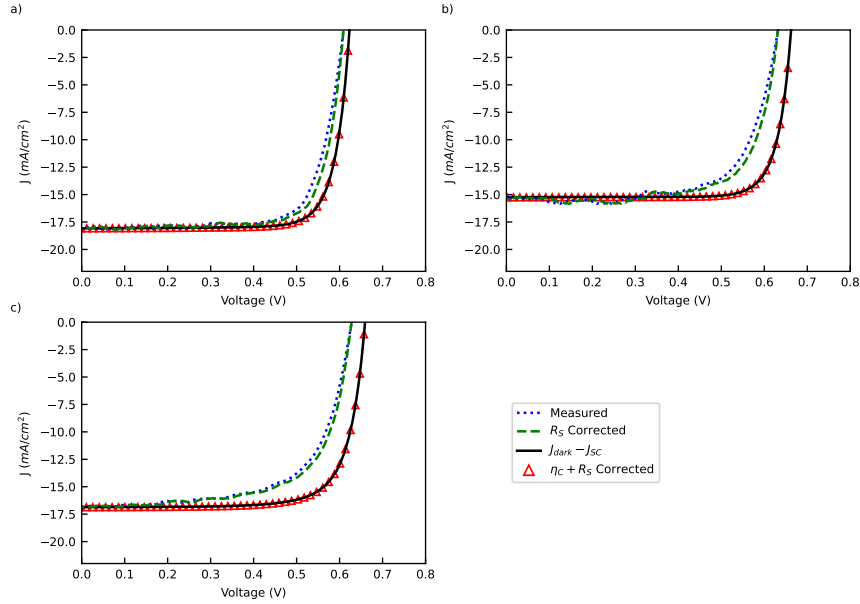


Figure 6.3 Measured and corrected JV curves for the a) Ref, b) RbS PDT, and c) RIS PDT devices.

TRPL measurements were performed to determine whether carrier lifetime influenced the loss mechanism. Figure 6.5 shows that the carrier lifetime increased in both PDT devices compared to the Ref. Bulk minority carrier lifetimes were calculated to be 8 ns, 122 ns, and 147 ns for the Ref, RbS PDT, and RIS PDT devices respectively. Longer carrier lifetime leads to longer diffusion length. This would allow carriers generated in the neutral region to reach the space charge region more easily, resulting in charge separation and collection. Since the PDT devices showed inferior collection efficiency despite longer carrier lifetimes, carrier lifetime does not appear to be the root cause.

Table 6.1 Device performance parameters for the measured and corrected JV curves. The change in V_{OC} , FF, and P_{max} after corrections is also included.

Device	Analysis	V_{OC} (mV)	ΔV_{OC} (mV)	FF (%)	ΔFF (abs.%)	ΔP_{max}
Ref	Measured	609		74.4		
	R_S Corrected	609		76.2	1.8	3.0
	$\eta_C + R_S$ Corrected	623	14	79.3	4.9	9.0
RbS PDT	Measured	632		70.4		
	R_S Corrected	632		72.7	2.2	3.7
	$\eta_C + R_S$ Corrected	660	28	81.0	11	20
RIS PDT	Measured	628		65.2		
	R_S Corrected	628		67.3	2.0	2.7
	$\eta_C + R_S$ Corrected	653	25	76.1	11	23

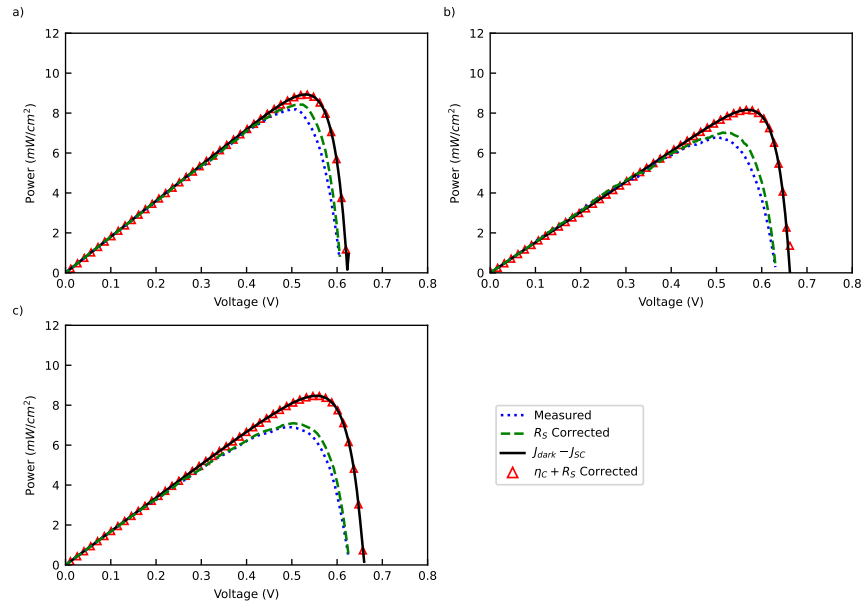


Figure 6.4 Measured and corrected power vs voltage curves for the a) Ref, b) RbS PDT, and c) RIS PDT devices.

To estimate the impact of recombination, reverse saturation current density (J_0) was calculated for each device. J_0 values are proportional to recombination and can be compared between samples [75]. Higher recombination rates can prevent carriers from reaching the space charge region where they are separated and collected. The calculated J_0 values were 1.3×10^{-6} mA/cm², 3.5×10^{-7} mA/cm², and 7.2×10^{-5} mA/cm² for the Ref, RbS PDT, and RIS PDT devices, respectively. While the RIS PDT sample had higher J_0 than the Ref device, indicative of increased recombination, the RbS PDT sample had the lowest J_0 . Since both PDT devices had worse collection efficiency, recombination may contribute, but was not the dominant cause.

The common 3-stage co-evaporation deposition technique used in this sample set creates a gradient in the GGI ratio near the front of the absorber. This feature, often referred to as a “V-notch” has been proposed as an influence on voltage-dependent collection [70]. To explore this, TOF-SIMS depth profiles were measured to compare the three samples. Figure 6.6 depicts the depth profiles of the GGI ratio. The GGI ratios for the Ref and RbS PDT devices had similar depth profiles while the RIS PDT device had a lower gradient near the heterojunction. The lower gradient in the RIS PDT device was due to the addition of In to the PDT, resulting in a lower GGI ratio. This feature can’t account for all of the voltage-dependent collection losses since the RbS PDT had similar losses to the RIS PDT.

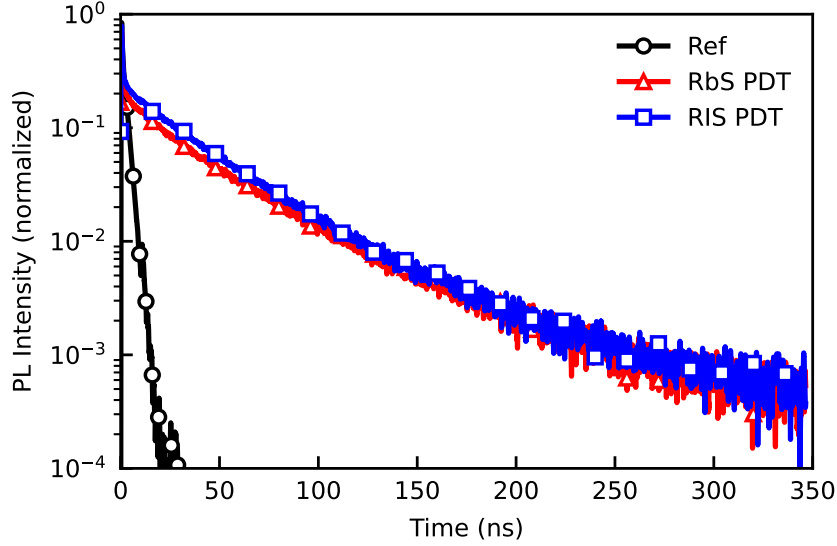


Figure 6.5 TRPL decay curves for each device displaying increased lifetime after PDT.

While the GGI profiles do not explain the voltage loss differences between the three devices it does provide an interesting comparison to the results presented by Poplavskyy et al. [70]. The GGI gradient presented in this study correlates well with several of the test devices in Poplavskyy et al. They found a FF loss due to η_C of 10 abs.% in samples with similar GGI gradients, which is close to the 11 abs.% drop in the PDT devices used in this study. Their results showed that increasing the GGI ratio at the heterojunction resulted in greater voltage-dependent collection losses. It is suggested that the steep gradient produces an electric field that opposes the collection field of the depletion region, leading to increased recombination. This comes as a trade-off since the steep gradient reduces interface recombination and leads to higher V_{OC} . The results from Poplavskyy et al. would predict the RIS PDT device to have lower FF losses, which suggests that the GGI gradient is not the only contributing factor. Still, optimizing the trade-off between interface recombination and voltage-dependent collection is an essential step in maximizing the performance of CIGS devices.

Figure 6.7a displays the carrier density vs depletion width plots calculated using variable C-V measurements. Aside from a steep increase in the RbS PDT device at low depletion width, the carrier density is within an order of magnitude for each sample across the depletion width range. Low depletion widths are another potential source of poor voltage-dependent collection efficiency. To test this, the C-V measurements were used to calculate the depletion width as a function of voltage (Figure 6.7b). The depletion widths at V_{mp} for the Ref, RbS PDT, and RIS PDT devices were $0.26 \mu\text{m}$, $0.07 \mu\text{m}$, and $0.16 \mu\text{m}$ respectively.

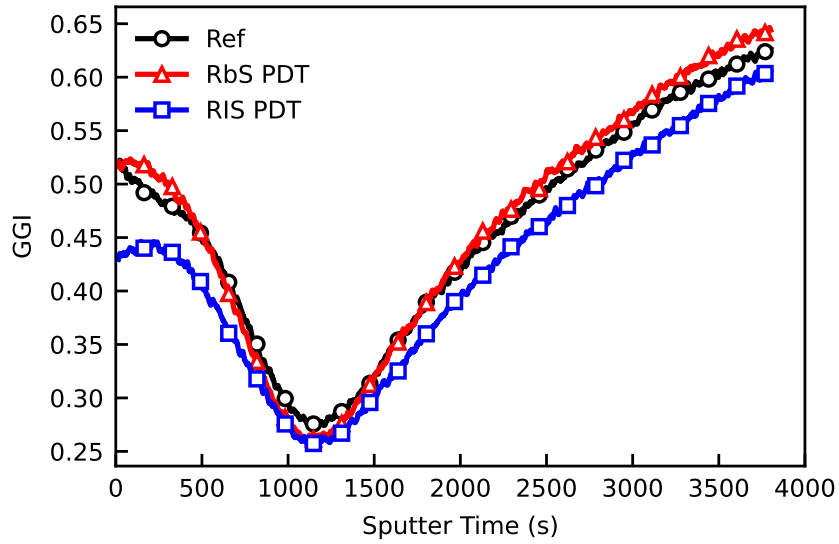


Figure 6.6 TOF-SIMS depth profiles showing the relative difference in GGI ratio within the CIGS absorber layer.

These results provide a potential mechanism for low collection efficiency as the PDT devices both have lower depletion widths than the Ref sample. Electron-hole pairs are less likely to reach a narrower depletion region where they can be separated. From the available experimental data, this mechanism fits the results most closely.

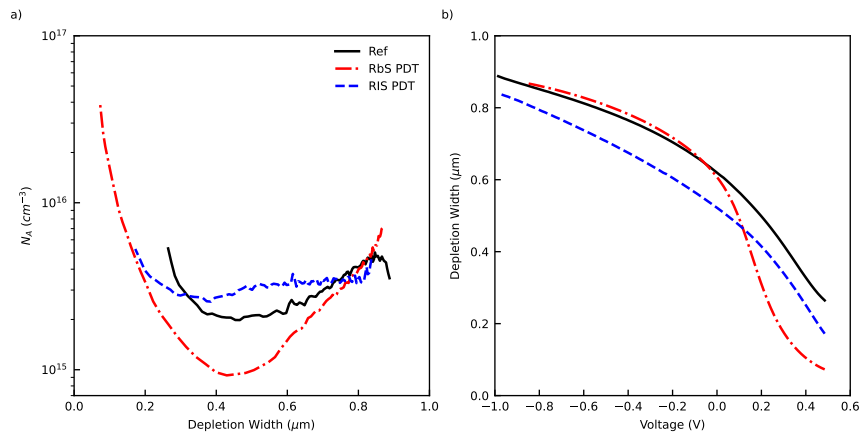


Figure 6.7 Variable C-V measurements providing a) carrier concentration vs depletion width and b) depletion width vs voltage for each device.

6.5 Conclusions

Two unique post-deposition treatments were analyzed for voltage-dependent collection efficiency (η_C) losses and compared to a standard reference (Ref) sample. The RbF+S (RbS) and RbF+In+S (RIS) PDTs both demonstrated lower collection efficiency at V_{mp} than the Ref device. V_{OC} losses due to η_C were 14 mV, 28 mV, and 25 mV in the Ref, RbS PDT, and RIS PDT devices respectively. Despite the increased V_{OC} loss due to η_C , the PDT devices still had higher overall V_{OC} than the Ref device. Additionally, FF loss due to R_S and η_C was 4.9 abs.% in the Ref sample and 11 abs.% in both PDT devices. This culminated in a maximum power loss of 9%, 20%, and 23% for the Ref, RbS PDT, and RIS PDT devices respectively. Several theories of the origin of η_C were tested to identify strategies for reducing losses. The best description was reduced depletion width in the PDT samples, although η_C likely depends on several factors. Improvements may also be possible by reducing the GGI gradient at the heterojunction. This comes at a trade-off with increased interface recombination, emphasizing the benefits of optimizing the GGI profile in CIGS photovoltaics. RbF PDTs show promising results for improving CIGS photovoltaics, and the analysis presented in this study identifies improving η_C as an important factor in optimizing device performance.

6.6 Acknowledgments

This work was supported in part by the U.S. Department of Energy's Office of Energy Efficiency and Renewable Energy (EERE) under Solar Energy Technologies Office (SETO) Award Number DE-EE0008755 and in part by the National Renewable Energy Laboratory, operated by Alliance for Sustainable Energy, LLC, for the U.S. Department of Energy (DOE) under Contract DE-AC36-08GO28308, in part by the U.S. Department of Energy Office of Energy Efficiency and Renewable Energy Solar Energy Technologies Office. The views expressed in the article do not necessarily represent the views of the DOE or the U.S. Government. The U.S. Government retains and the publisher, by accepting the article for publication, acknowledges that the U.S. Government retains a nonexclusive, paid-up, irrevocable, worldwide license to publish or reproduce the published form of this work, or allow others to do so, for U.S. Government purposes. This material makes use of the TOF-SIMS system at the Colorado School of Mines, which was supported by the National Science Foundation under Grant No. 1726898.

CHAPTER 7

DEFECT ANALYSIS OF RbF BASED POST-DEPOSITION TREATMENTS IN $\text{Cu}(\text{In}_x\text{Ga}_{1-x})\text{Se}_2$ SOLAR CELLS

This chapter presents preliminary work on defect characterization of RbF treated CIGS solar cells. Transient photocapacitance and deep-level transient spectroscopy were used to compare three CIGS devices.

7.1 Introduction

One of the most effective techniques for identifying defects in semiconductor devices is the capacitance transient. Complete explanations of capacitance transients can be found elsewhere, however a brief description will be provided here for context [3]. Capacitance transients are created by applying voltage pulses to a diode and measuring the capacitance response due to changes in the depletion width. Typically, the voltage begins in reverse bias to establish an equilibrium state with a junction capacitance of C_0 . Then, a 0 V or forward bias pulse is applied which shrinks the depletion width and causes a spike in capacitance. As the depletion width shrinks charge carriers can populate defect levels in the previously depleted zone. The voltage is then returned to reverse bias which allows the depletion region to reach equilibrium once again, but the traps remain occupied. Excess charge remains in the depletion region due to the occupied traps, resulting in a non-equilibrium capacitance. If the traps are filled with majority carriers the non-equilibrium value will be less than C_0 , and for minority traps the non-equilibrium value is greater than C_0 . Finally, the traps depopulate through thermal or other excitation sources and the capacitance returns to equilibrium following an exponential curve. Characteristic decay curves are shown for majority and minority carrier emission in Figure 7.1.

Transient photocapacitance (TPC) is a technique used to identify defect levels within the bandgap of a semiconductor device [76]. A TPC measurement is performed by recording a capacitance transient in the dark followed by an additional transient performed with low intensity, monochromatic light. The dark transient is subtracted from the illuminated transient to remove the effect of thermal excitation. The resulting curve represents carrier excitation due to the photonic flux at the wavelength used. This curve is integrated over the desired time window and the resulting value plotted on a graph of TPC signal vs photon energy. By sweeping the photon energy used for illumination a TPC measurement is completed. Any defects that were excited by the photonic flux will appear as a Gaussian curve. The band-edge will also appear in the graph since photons with energy above the bandgap will excite carriers during the transient.

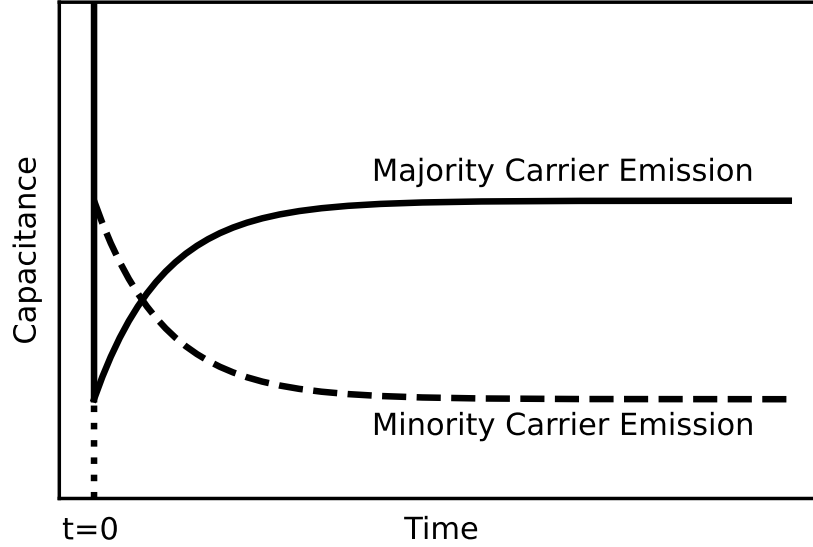


Figure 7.1 Exponential decay curves for capacitance transients featuring majority carrier emission (solid line) and minority carrier emission (dotted line). $t=0$ represents the point when the sample is put into reverse bias and the traps begin to depopulate. This figure is inspired by Fig. 5.8 in [3].

7.2 Experimental Methods

TPC measurements were performed on a home-built instrument at the National Renewable Energy Laboratory. A Stanford Research SR570 current pre-amplifier and a SR830 lock-in amplifier were used to measure sample capacitance. A Digikrom DK240 monochromator was used to select the desired wavelength from a halogen light source. A Linkam LTS420 was used for temperature control. Custom LabView software was used to collect data. Measurements were performed at 300 K using a reverse bias pulse of -0.5 V and a forward bias pulse of 0.2 V. The wavelength was swept from 1.30 eV to 0.5 eV.

Deep level transient spectroscopy (DLTS) measurements were performed on the same instrument. The bias pulse parameters were the same as those used in TPC. The temperature of the Ref and RIS PDT samples was swept from 150 K to 400 K in 1 K steps while the RbS PDT device was swept from 150 K to 350 K in 1 K steps. The upper limit of the temperature sweep was chosen to capture the major DLTS peak while limiting thermal load.

DLTS rate windows were calculated as $\Delta C = C_{t_1} - C_{t_2}$ with $t_2/t_1 = 2.5$. By keeping the ratio of t_2/t_1 constant the DLTS peaks should maintain the same shape and amplitude at each rate window, and only the peak temperature changes [3]. The maximum emission rate used for Arrhenius plots was calculated as [3]:

$$e = \ln((t_1/t_2)/(t_1 - t_2)) \quad (7.1)$$

7.3 Results and Discussion

Figure 7.2 shows TPC spectra for the three devices outlined in Chapter 6. The band edge can be seen near 1.20 eV and a defect level is present at 0.8 eV. Each spectrum has been normalized to the intensity at 1.30 eV which assumes that the conduction band density of states does not change between samples. Thin-film interference fringes are clearly visible in the defect band region, an observation seen in other studies. The magnitude of the TPC signal at 0.8 eV decreases after the RbF-based post-deposition treatments (PDTs). This suggests that the concentration of a defect at $E_V+0.8$ eV is reduced by the RbF PDT.

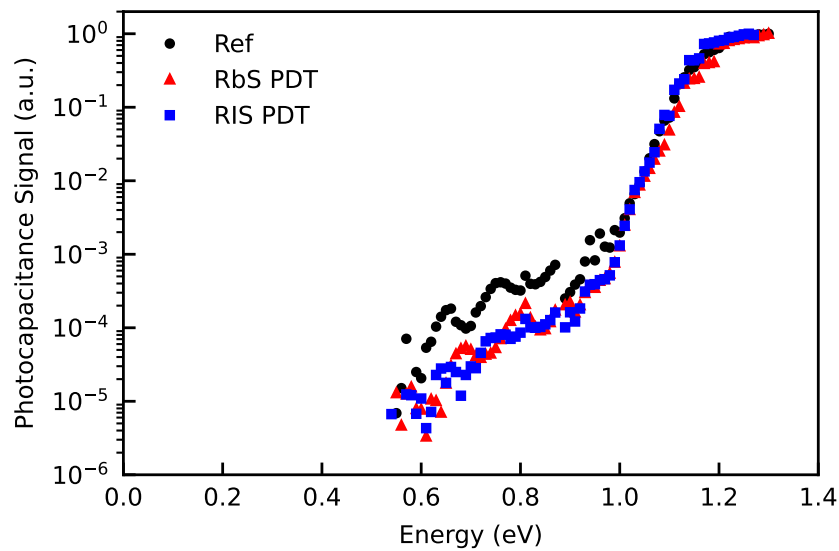


Figure 7.2 TPC spectra normalized to the intensity at 1.30 eV. A defect centered at 0.8 eV is present in all samples with reduced intensity in the RbF PDT samples.

The $E_V+0.8$ eV defect has been reported previously in TPC studies of CIGS devices [77–80]. Although the identity of the defect is not certain, it has been proposed to represent the $V_{Cu}+V_{Se}$ divacancy complex. If this is the case, the results presented here would agree with the findings published by Karki et al. which found a decrease in the divacancy complex concentration after RbF PDT [31].

Due to the process used to calculate TPC data points, valuable information about the shape of the capacitance transients is lost. There is a missed opportunity to gain additional understanding about the defect composition of diodes when the transients are replaced with a single value. Figure 7.3 displays the dark and light transients for the same sample set using a photon energy of 1.30 eV. Despite the TPC spectra having similar shapes, the transients are quite different and provide additional information. The Ref sample transients show behavior that is characteristic of majority carrier emission. This represents a

majority carrier trap that is occupied during the filling pulse and empties during the transient. The RIS PDT device fits better to minority carrier emission. The RbS PDT device has mixed behavior with the beginning of the transient representative of minority carrier emission, which is overtaken by majority carrier emission as the transient evolves. The light transients also show that photons enhance majority carrier emission more than minority carrier emission. This explains why the TPC signal in Figure 7.2 is positive in all three samples.

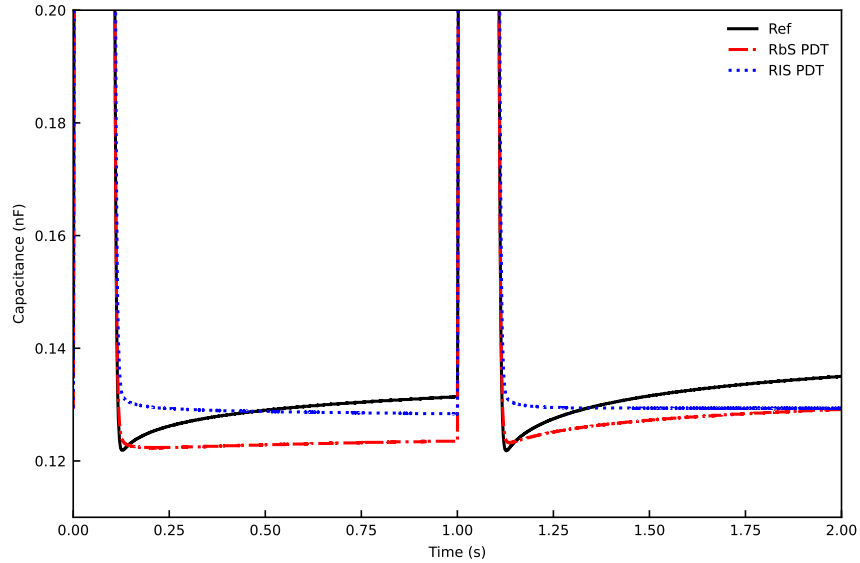


Figure 7.3 Dark (left) and light (right) capacitance transients for each sample. 1.30 eV light was used in the illuminated transients.

The specific source of the behavior seen in the capacitance transients is not known, however some conclusions can be drawn. From the dark transient of the RbS PDT sample there appears to be at least two active trap states. The RbF PDT also appears to change the trap signature which may influence device behavior. Previous work from Karki et al. found RbF PDT to decrease the concentration of an $E_V+0.98$ eV trap state while having no effect on an $E_V+0.56$ eV majority carrier trap [31]. Helder et al. observed a minority trap at $E_V+0.45$ eV in addition to a majority trap at $E_V+0.6$ eV [66]. They found that RbF PDT had little effect on the majority trap while decreasing the concentration of the minority trap. The behavior reported here appears to be different than either of these cases as the minority trap becomes more prominent after PDT. Further research is needed to identify the trap mechanism present in these samples, however this analysis displays the benefits of considering the capacitance transients during TPC experiments. With the addition of a temperature-controlled chamber, a single TPC experiment can provide temperature-dependent TPC along with dark and light DLTS. To learn more about the defect

structure of the sample set capacitance spectra were collected and DLTS analysis performed.

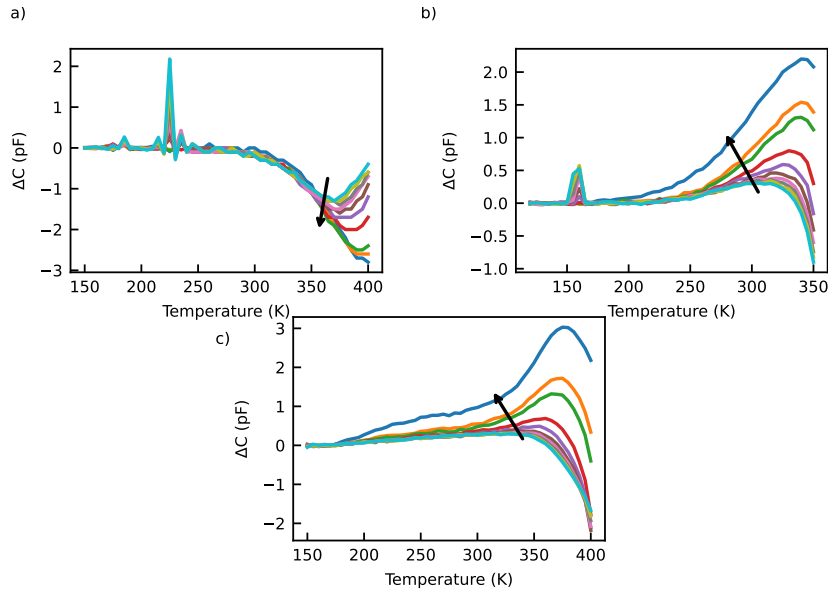


Figure 7.4 DLTS spectra for a) Ref, b) RbS PDT, and c) RIS PDT at rate windows from 1.9 Hz to 25.5 Hz. The arrows indicate increasing rate window frequency. The PDT samples show the formation of a possible shoulder peak at high frequencies.

DLTS spectra for each sample are shown in Figure 7.4 and shows a negative peak for the Ref sample and positive peaks in the PDT samples. A negative peak indicates a majority carrier trap while a positive peak indicates minority carrier traps [3]. The peak trends are similar to those seen in the TPC transients, although the RbS PDT sample does not show a majority carrier peak. The RIS PDT device may also be developing a second minority carrier shoulder peak, although longer rate windows are needed to further study this signal.

The peak emission frequency for each sample was calculated for several rate windows and plotted on an Arrhenius plot (Figure 7.5). Based on the slope of each curve the trap energy was calculated to be $E_V+0.97$ eV, $E_C-0.99$ eV, $E_C-0.81$ eV for the Ref, RbS PDT, and RIS PDT devices respectively. DLTS typically is not used to probe traps this deep due to the slow thermal emission rates [3]. Additionally, the DLTS peaks should not experience a change in shape or magnitude at different rate windows. The peaks should simply shift in temperature [3]. This is not the case in the samples measured here which suggests that a more complicated process is occurring. A potential factor could be the presence of multiple defects resulting in exponential emissions that overlap. At this time, it is not understood what is causing these effects and further research is needed to gain better understanding.

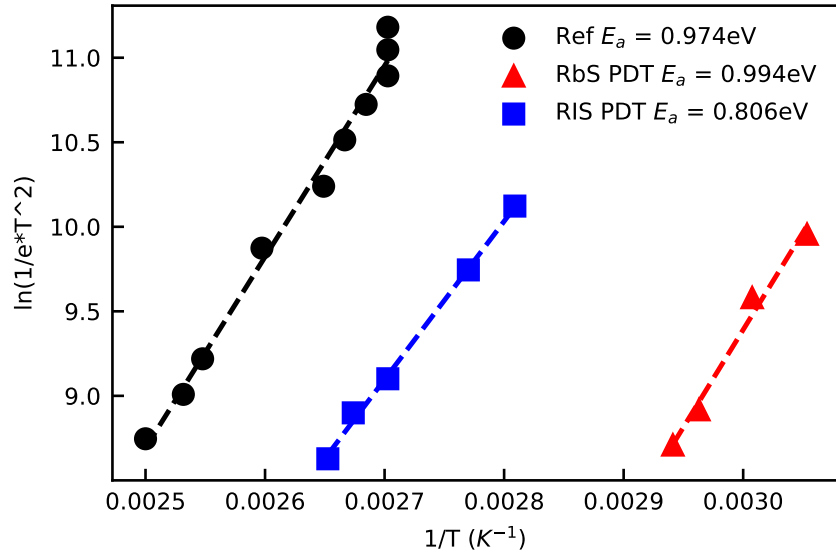


Figure 7.5 Arrhenius plots calculating the activation energy of the DLTS peaks. The activation energies are higher than typical DLTS measurements and may indicate non-ideal behavior.

7.4 Conclusions

In this preliminary research two capacitance based techniques were used to study the effect of RbF-based PDTs on CIGS solar cells. Transient photocapacitance (TPC) showed the existence of a 0.8 eV trap state which has been linked to the $V_{Cu}+V_{Se}$ divacancy complex. Additionally, the concentration of the defect was found to be reduced after PDT. It was also shown that information about the defect chemistry of a device can be lost during TPC measurements. Individual capacitance transients revealed that multiple defects are active, and that the RbF PDT changed which trap state is dominant. Researchers using the TPC technique should monitor the individual transients to ensure that no information is lost. DLTS was also used to study the traps and revealed the Ref device had a majority carrier trap while the PDT devices had a minority carrier trap. Arrhenius plots calculated the activation energy of the trap states to be much higher than typical DLTS experiments. The DLTS spectra also displayed non-ideal behavior. Additional research will be needed to understand the origins of the identified trap states.

CHAPTER 8

CONCLUSIONS

8.1 Conclusions

This thesis presents an analysis of the effects of several RbF PDTs on the electronic properties of CIGS solar cells. All RbF PDT devices experienced an increase in V_{OC} relative to reference samples. Chapter 4 provided evidence that point defects and bandtails are both influential in determining V_{OC} . The specific defect concentration and bandtail characteristic energy were found to influence which source was the dominant factor. Therefore, processing conditions are essential to determining how these factors impact V_{OC} . The RbF PDT device studied in Chapter 4 was found to have reduced bandtail width and increased minority carrier lifetime, which contributes to the V_{OC} improvement. Increased V_{OC} , and resulting increased device efficiency, provide motivation to optimize the RbF PDT process in the future.

The effect of RbF PDT is less clear when it comes to FF. Although the devices presented in Chapter 4 demonstrated an increase in FF after PDT, the opposite result was found for the devices in Chapters 5 and 6. The key loss mechanisms were found to be series resistance and voltage-dependent collection. Evidence suggests that voltage-dependent collection may originate from reduced depletion width as well as the bandgap gradient near the heterojunction.

Another consideration is the long-term stability of RbF PDT devices. Results in Chapter 5 showed that a RbF PDT device experienced more degradation than a reference sample after six months in a desiccator. The reference device as well as the RbF PDT device developed a blocking contact, although the barrier height of the blocking contact was greater in the RbF PDT sample. In addition, the RbF PDT initially benefited from reduced J_0 , but after aging the J_0 values were similar to the reference.

Overall, RbF PDT shows promising results for improving CIGS solar cells. Maximizing benefits will require careful optimization of processing conditions and consideration of trade-offs. More work is also needed to improve long-term stability if this technique is to be used in a commercial setting.

8.2 Future Work

Improving V_{OC} is an important consideration to make CIGS a commercially successful technology. RbF PDTs consistently increase V_{OC} and have the potential to improve conversion efficiency in CIGS PV. Further research is still needed to maximize the performance of RbF treated CIGS. This thesis highlights several areas where additional work is needed to understand the mechanisms involved with RbF PDTs.

The sample set manufactured by the Université de Nantes provided valuable insight into the effect of two unique RbF-based PDTs. However, additional understanding could be gained by including a RbF PDT performed under a Se atmosphere. By including this additional device, the impact of the chalcogen can be isolated from RbF. This would improve upon the current work which combines the effects of the chalcogen and RbF into a single device.

Another essential area of study is in device stability. There is relatively little published research on the long-term device stability of RbF PDT devices, and Chapter 5 highlighted the decline in performance over time. This work focused on the decline in performance over time, but there are still questions about the cause of these declines. TOF-SIMS or transmission electron microscopy experiments before and after aging may provide valuable information into atomic migration over time. TOF-SIMS experiments presented in Chapters 4 and 5 showed that Rb tends to displace other alkali elements and concentrates at interfaces. The high mobility of alkali elements in CIGS could result in the distribution changing over time. It may also provide insight into the formation of a back contact barrier seen in Chapter 5. Understanding how elements have moved to form this barrier could provide valuable information to mitigate the effect.

Further work on defect analysis of RbF treated CIGS would also be valuable. While there has been a significant number of high-quality papers published on the subject, the defect mechanisms are still not certain. Chapter 7 discussed some unique challenges in analyzing defects in RbF PDT CIGS and identified a potential change in defect behavior after PDT. The non-ideal DLTS behavior shown in Chapter 7 made it difficult to extract activation energies. A potential explanation is the existence of multiple defects with similar emission rates that are overlapping. Attempting to decompose the capacitance transients into the individual trap signals may be a method of extracting the trap behavior.

As discussed earlier in this thesis, the commercial market for CIGS PV has declined in recent years. However, there is emerging research that takes advantage of the tunable bandgap found in CIGS to make tandem solar cells. CIGS tandem devices have been made with silicon and perovskite partner materials. This research could be important to the future of CIGS PV, and understanding how RbF PDTs behave in tandem devices is important. Using the techniques shown in this thesis, such as JVT, on tandem devices treated with RbF would be valuable going forward. TOF-SIMS would also be helpful to monitor how the alkali elements move in a tandem device and whether or not they remain within the CIGS layer.

REFERENCES

- [1] Angus Rockett. *The Materials Science of Semiconductors*. Springer, 2007. ISBN 0-387-25653-9.
- [2] Jenny Nelson. *The Physics of Solar Cells*. ICP, 2003. ISBN 978-1-86094-349-2.
- [3] DIETER K. SCHRODER. *SEMICONDUCTOR MATERIAL AND DEVICE CHARACTERIZATION*. Wiley-Interscience, third edition, 2006. ISBN 0-471-73906-5.
- [4] Steven S. Hegedus and William N. Shafarman. Thin-film solar cells: device measurements and analysis. *Progress in Photovoltaics: Research and Applications*, 12(2-3):155–176, 2004. ISSN 1099-159X. doi: <https://doi.org/10.1002/pip.518>. URL <http://onlinelibrary.wiley.com/doi/abs/10.1002/pip.518>. eprint: <https://onlinelibrary.wiley.com/doi/pdf/10.1002/pip.518>.
- [5] Charles J. Hages, Nathaniel J. Carter, Rakesh Agrawal, and Thomas Unold. Generalized current-voltage analysis and efficiency limitations in non-ideal solar cells: Case of $\text{Cu}_2\text{ZnSn}(\text{S}_x\text{Se}_{1-x})_4$ and $\text{Cu}_2\text{Zn}(\text{Sn}_y\text{Ge}_{1-y})(\text{S}_x\text{Se}_{1-x})_4$. *Journal of Applied Physics*, 115(23):234504, June 2014. ISSN 0021-8979, 1089-7550. doi: 10.1063/1.4882119. URL <http://aip.scitation.org/doi/10.1063/1.4882119>.
- [6] Steven Simon. *The Oxford Solid State Basics*. Oxford University Press, 2013. ISBN 0-19-968077-9.
- [7] S. M. Wasim, C. Rincón, G. Marín, P. Bocaranda, E. Hernández, Ismardo Bonalde, and Ernesto Medina. Effect of structural disorder on the Urbach energy in Cu ternaries. *Phys. Rev. B*, 64(19):195101, October 2001. doi: 10.1103/PhysRevB.64.195101. URL <https://link.aps.org/doi/10.1103/PhysRevB.64.195101>. Publisher: American Physical Society.
- [8] M. Souilah, A. Lafond, Catherine Guillot-Deudon, Sylvie Harel, and Michel Evain. Structural investigation of the $\text{Cu}_2\text{Se-In}_2\text{Se}_3\text{-Ga}_2\text{Se}_3$ phase diagram, X-ray photoemission and optical properties of the $\text{Cu}_{1-z}(\text{In}_{0.5}\text{Ga}_{0.5})_{1+z}\text{Se}_{-z/3(2)}$ compounds. *Journal of Solid State Chemistry*, 183(10):2274, 2010. doi: 10.1016/j.jssc.2010.08.014. URL <https://hal.science/hal-00849310>.
- [9] (IUCr) VESTA3 for three-dimensional visualization of crystal, volumetric and morphology data, . URL <https://onlinelibrary.wiley.com/iucr/doi/10.1107/S0021889811038970>.
- [10] William Shockley and Hans J. Queisser. Detailed Balance Limit of Efficiency of p-n Junction Solar Cells. *Journal of Applied Physics*, 32(3):510–519, March 1961. ISSN 0021-8979. doi: 10.1063/1.1736034. URL <https://aip.scitation.org/doi/10.1063/1.1736034>. Publisher: American Institute of Physics.
- [11] Su-Huai Wei and Alex Zunger. Band offsets and optical bowings of chalcopyrites and Zn-based II-VI alloys. *Journal of Applied Physics*, 78(6):3846–3856, September 1995. ISSN 0021-8979, 1089-7550. doi: 10.1063/1.359901. URL <http://aip.scitation.org/doi/10.1063/1.359901>.
- [12] Chia-Hua Huang. Effects of Ga content on $\text{Cu}(\text{In},\text{Ga})\text{Se}_2$ solar cells studied by numerical modeling. *Journal of Physics and Chemistry of Solids*, 69(2):330–334, February 2008. ISSN 0022-3697. doi: 10.1016/j.jpcs.2007.07.093. URL <https://www.sciencedirect.com/science/article/pii/S0022369707003332>.

- [13] Andriy Zakutayev, Christopher M. Caskey, Angela N. Fioretti, David S. Ginley, Julien Vidal, Vladan Stevanovic, Eric Tea, and Stephan Lany. Defect Tolerant Semiconductors for Solar Energy Conversion. *J. Phys. Chem. Lett.*, 5(7):1117–1125, April 2014. doi: 10.1021/jz5001787. URL <https://doi.org/10.1021/jz5001787>. Publisher: American Chemical Society.
- [14] S B Zhang, Su-Huai Wei, Alex Zunger, and H Katayama-Yoshida. Defect physics of the CuInSe₂ chalcopyrite semiconductor. page 15.
- [15] Arturo Morales-Acevedo. Effective absorption coefficient for graded band-gap semiconductors and the expected photocurrent density in solar cells. *Solar Energy Materials and Solar Cells*, 93(1):41–44, January 2009. ISSN 0927-0248. doi: 10.1016/j.solmat.2008.02.015. URL <https://www.sciencedirect.com/science/article/pii/S092702480800069X>.
- [16] Patrick Reinhard, Adrian Chirilă, Patrick Blösch, Fabian Pianezzi, Shiro Nishiwaki, Stephan Buechelers, and Ayodhya N. Tiwari. Review of progress toward 20% efficiency flexible CIGS solar cells and manufacturing issues of solar modules. In *2012 IEEE 38th Photovoltaic Specialists Conference (PVSC) PART 2*, pages 1–9, June 2012. doi: 10.1109/PVSC-Vol2.2012.6656789.
- [17] Takuya Kato, Kimihiko Kitani, Kong Fai Tai, Rui Kamada, Homare Hiroi, and Hiroki Sugimoto. *Characterization of the Back Contact of CIGS Solar Cell as the Origin of "Rollover" Effect*. June 2016. doi: 10.4229/EUPVSEC20162016-3AO.5.3.
- [18] Lorelle M. Mansfield, Rebekah L. Garris, Kahl D. Counts, James R. Sites, Christopher P. Thompson, William N. Shafarman, and Kannan Ramanathan. Comparison of CIGS Solar Cells Made With Different Structures and Fabrication Techniques. *IEEE Journal of Photovoltaics*, 7(1):286–293, January 2017. ISSN 2156-3403. doi: 10.1109/JPHOTOV.2016.2616188. Conference Name: IEEE Journal of Photovoltaics.
- [19] S. Raud and M. A. Nicolet. Study of the CuInSe₂/Mo thin film contact stability. *Thin Solid Films*, 201(2):361–371, June 1991. ISSN 0040-6090. doi: 10.1016/0040-6090(91)90124-G. URL <https://www.sciencedirect.com/science/article/pii/004060909190124G>.
- [20] Ellen Moons, Tina Engelhard, and David Cahen. Ohmic contacts to p-CuInSe₂ crystals. *J. Electron. Mater.*, 22(3):275–280, March 1993. ISSN 1543-186X. doi: 10.1007/BF02661377. URL <https://doi.org/10.1007/BF02661377>.
- [21] Kuo-Jui Hsiao, Jing-Da Liu, Hsing-Hua Hsieh, and Ting-Shiuan Jiang. Electrical impact of MoSe₂ on CIGS thin-film solar cells. *Physical Chemistry Chemical Physics*, 15(41):18174–18178, 2013. doi: 10.1039/C3CP53310G. URL <https://pubs.rsc.org/en/content/articlelanding/2013/cp/c3cp53310g>. Publisher: Royal Society of Chemistry.
- [22] T Wada, N Kohara, S Nishiwaki, and T Negami. Characterization of the Cu(In,Ga)Se₂/Mo interface in CIGS solar cells. *Thin Solid Films*, 387(1):118–122, May 2001. ISSN 0040-6090. doi: 10.1016/S0040-6090(00)01846-0. URL <https://www.sciencedirect.com/science/article/pii/S0040609000018460>.
- [23] T Dullweber, G. H. Anna, U Rau, and H. W. Schock. A new approach to high-efficiency solar cells by band gap grading in Cu(In,Ga)Se₂ chalcopyrite semiconductors. *Solar Energy Materials and Solar Cells*, 67(1):145–150, March 2001. ISSN 0927-0248. doi: 10.1016/S0927-0248(00)00274-9. URL <https://www.sciencedirect.com/science/article/pii/S0927024800002749>.

- [24] Wolfram Witte, Stefanie Spiering, and Dimitrios Hariskos. Substitution of the CdS buffer layer in CIGS thin-film solar cells. *Vakuum in Forschung und Praxis*, 26(1):23–27, 2014. ISSN 1522-2454. doi: 10.1002/vipr.201400546. URL <https://onlinelibrary.wiley.com/doi/abs/10.1002/vipr.201400546>. eprint: <https://onlinelibrary.wiley.com/doi/pdf/10.1002/vipr.201400546>.
- [25] Ana Kanevce, Stefan Paetel, Dimitrios Hariskos, and Theresa Magorian Friedlmeier. Impact of RbF-PDT on Cu(In,Ga)Se₂ solar cells with CdS and Zn(O,S) buffer layers. *EPJ Photovolt.*, 11:8, 2020. ISSN 2105-0716. doi: 10.1051/epjpv/2020005. URL <https://www.epj-pv.org/10.1051/epjpv/2020005>.
- [26] Motoshi Nakamura, Koji Yamaguchi, Yoshinori Kimoto, Yusuke Yasaki, Takuya Kato, and Hiroki Sugimoto. Cd-Free Cu(In,Ga)(Se,S)₂ Thin-Film Solar Cell With Record Efficiency of 23.35%. *IEEE Journal of Photovoltaics*, 9(6):1863–1867, November 2019. ISSN 2156-3403. doi: 10.1109/JPHOTOV.2019.2937218. Conference Name: IEEE Journal of Photovoltaics.
- [27] V. Probst, J. Rimmasch, W. Riedl, W. Stetter, J. Holz, H. Harms, F. Karg, and H.W. Schock. The impact of controlled sodium incorporation on rapid thermal processed Cu(InGa)Se/sub 2/-thin films and devices. In *Proceedings of 1994 IEEE 1st World Conference on Photovoltaic Energy Conversion - WCPEC (A Joint Conference of PVSC, PVSEC and PSEC)*, volume 1, pages 144–147 vol.1, December 1994. doi: 10.1109/WCPEC.1994.519828.
- [28] M.A. Contreras, B. Egaas, P. Dippo, J. Webb, J. Granata, K. Ramanathan, S. Asher, A. Swartzlander, and R. Noufi. On the role of Na and modifications to Cu(In,Ga)Se/sub 2/ absorber materials using thin-MF (M=Na, K, Cs) precursor layers [solar cells]. In *Conference Record of the Twenty Sixth IEEE Photovoltaic Specialists Conference - 1997*, pages 359–362, September 1997. doi: 10.1109/PVSC.1997.654102. ISSN: 0160-8371.
- [29] Su-Huai Wei, S. B. Zhang, and Alex Zunger. Effects of Na on the electrical and structural properties of CuInSe₂. *Journal of Applied Physics*, 85(10):7214–7218, May 1999. ISSN 0021-8979, 1089-7550. doi: 10.1063/1.370534. URL <http://aip.scitation.org/doi/10.1063/1.370534>.
- [30] D. Rudmann, G. Bilger, M. Kaelin, F. J. Haug, H. Zogg, and A. N. Tiwari. Effects of NaF coevaporation on structural properties of Cu(In,Ga)Se₂ thin films. *Thin Solid Films*, 431-432:37–40, May 2003. ISSN 0040-6090. doi: 10.1016/S0040-6090(03)00246-3. URL <http://www.sciencedirect.com/science/article/pii/S0040609003002463>.
- [31] S. Karki, P. Paul, G. Rajan, B. Belfore, D. Poudel, A. Rockett, E. Danilov, F. Castellano, A. Arehart, and S. Marsillac. Analysis of Recombination Mechanisms in RbF-Treated CIGS Solar Cells. *IEEE Journal of Photovoltaics*, 9(1):313–318, January 2019. ISSN 2156-3403. doi: 10.1109/JPHOTOV.2018.2877596. Conference Name: IEEE Journal of Photovoltaics.
- [32] Lorelle M. Mansfield, Stephen Glynn, Steve Johnston, Craig Marshall, Christopher P. Muzzillo, Bart Stevens, and Matthew R. Young. Setting boundaries on the recipe for a successful RbF post-deposition treatment of CIGS. *Solar Energy Materials and Solar Cells*, 245:111862, September 2022. ISSN 0927-0248. doi: 10.1016/j.solmat.2022.111862. URL <https://www.sciencedirect.com/science/article/pii/S0927024822002823>.
- [33] Tim Kodalle, Marc D. Heinemann, Dieter Greiner, Hasan A. Yetkin, Michael Klupsch, Chen Li, Peter A. van Aken, Iver Lauermann, Rutger Schlattmann, and Christian A. Kaufmann. Elucidating the Mechanism of an RbF Post Deposition Treatment in CIGS Thin Film Solar Cells. *Solar RRL*, 2(9):1800156, 2018. ISSN 2367-198X. doi: 10.1002/solr.201800156. URL <https://onlinelibrary.wiley.com/doi/abs/10.1002/solr.201800156>. eprint: <https://onlinelibrary.wiley.com/doi/pdf/10.1002/solr.201800156>.

- [34] Jake Wands, Ana Kanevce, Alexandra Bothwell, Michael F. Miller, Stefan Paetel, Aaron R. Arehart, and Angus Rockett. Evaluating Recombination Mechanisms in RbF Treated $\text{Cu}(\text{In}_{1-x}\text{Ga}_x)\text{Se}_2$ Solar Cells. *IEEE Journal of Photovoltaics*, pages 1–6, 2022. ISSN 2156-3403. doi: 10.1109/JPHOTOV.2022.3197926. Conference Name: IEEE Journal of Photovoltaics.
- [35] Susanne Siebentritt, Enrico Avancini, Marcus Bär, Jakob Bombsch, Emilie Bourgeois, Stephan Buecheler, Romain Carron, Celia Castro, Sebastien Duguay, Roberto Félix, Evelyn Handick, Dimitrios Hariskos, Ville Havu, Philip Jackson, Hannu-Pekka Komsa, Thomas Kunze, Maria Malitckaya, Roberto Menozzi, Milos Nesladek, Nicoleta Nicoara, Martti Puska, Mohit Raghuvanshi, Philippe Pareige, Sascha Sadewasser, Giovanna Sozzi, Ayodhya Nath Tiwari, Shigenori Ueda, Arantxa Vilalta-Clemente, Thomas Paul Weiss, Florian Werner, Regan G. Wilks, Wolfram Witte, and Max Hilaire Wolter. Heavy Alkali Treatment of $\text{Cu}(\text{In,Ga})\text{Se}_2$ Solar Cells: Surface versus Bulk Effects. *Advanced Energy Materials*, 10(8):1903752, 2020. ISSN 1614-6840. doi: <https://doi.org/10.1002/aenm.201903752>. URL <https://onlinelibrary.wiley.com/doi/abs/10.1002/aenm.201903752>. eprint: <https://onlinelibrary.wiley.com/doi/pdf/10.1002/aenm.201903752>.
- [36] Philipp Schöppe, Sven Schönherr, Philip Jackson, Roland Wuerz, Wolfgang Wisniewski, Maurizio Ritzer, Maximilian Zapf, Andreas Johannes, Claudia S. Schnohr, and Carsten Ronning. Overall Distribution of Rubidium in Highly Efficient $\text{Cu}(\text{In,Ga})\text{Se}_2$ Solar Cells. *ACS Appl. Mater. Interfaces*, 10(47):40592–40598, November 2018. ISSN 1944-8244, 1944-8252. doi: 10.1021/acsami.8b16040. URL <https://pubs.acs.org/doi/10.1021/acsami.8b16040>.
- [37] Arantxa Vilalta-Clemente, Mohit Raghuvanshi, Sébastien Duguay, Celia Castro, Emmanuel Cadel, Philippe Pareige, Philip Jackson, Roland Wuerz, Dimitrios Hariskos, and Wolfram Witte. Rubidium distribution at atomic scale in high efficient $\text{Cu}(\text{In,Ga})\text{Se}_2$ thin-film solar cells. *Appl. Phys. Lett.*, 112(10):103105, March 2018. ISSN 0003-6951, 1077-3118. doi: 10.1063/1.5020805. URL <http://aip.scitation.org/doi/10.1063/1.5020805>.
- [38] Max Hilaire Wolter, Romain Carron, Enrico Avancini, Benjamin Bissig, Thomas Paul Weiss, Shiro Nishiwaki, Thomas Feurer, Stephan Buecheler, Philip Jackson, Wolfram Witte, and Susanne Siebentritt. How band tail recombination influences the open-circuit voltage of solar cells. *Progress in Photovoltaics: Research and Applications*, n/a(n/a). ISSN 1099-159X. doi: 10.1002/pip.3449. URL <https://onlinelibrary.wiley.com/doi/abs/10.1002/pip.3449>. eprint: <https://onlinelibrary.wiley.com/doi/pdf/10.1002/pip.3449>.
- [39] M. H. Wolter, B. Bissig, E. Avancini, R. Carron, S. Buecheler, P. Jackson, and S. Siebentritt. Influence of Sodium and Rubidium Postdeposition Treatment on the Quasi-Fermi Level Splitting of $\text{Cu}(\text{In,Ga})\text{Se}_2$ Thin Films. *IEEE Journal of Photovoltaics*, 8(5):1320–1325, September 2018. ISSN 2156-3403. doi: 10.1109/JPHOTOV.2018.2855113. Conference Name: IEEE Journal of Photovoltaics.
- [40] D. Hauschild, D. Kreikemeyer-Lorenzo, P. Jackson, T. Magorian Friedlmeier, D. Hariskos, F. Reinert, M. Powalla, C. Heske, and L. Weinhardt. Impact of a RbF Postdeposition Treatment on the Electronic Structure of the $\text{CdS}/\text{Cu}(\text{In,Ga})\text{Se}_2$ Heterojunction in High-Efficiency Thin-Film Solar Cells. *ACS Energy Lett.*, 2(10):2383–2387, October 2017. ISSN 2380-8195, 2380-8195. doi: 10.1021/acsenerylett.7b00720. URL <https://pubs.acs.org/doi/10.1021/acsenerylett.7b00720>.
- [41] Noboru Taguchi, Shingo Tanaka, and Shogo Ishizuka. Direct insights into RbInSe_2 formation at $\text{Cu}(\text{In,Ga})\text{Se}_2$ thin film surface with RbF postdeposition treatment. *Appl. Phys. Lett.*, 113(11): 113903, September 2018. ISSN 0003-6951, 1077-3118. doi: 10.1063/1.5044244. URL <http://aip.scitation.org/doi/10.1063/1.5044244>.

- [42] Fu Qiang Huang, Bin Deng, Donald E. Ellis, and James A. Ibers. Preparation, structures, and band gaps of RbInS₂ and RbInSe₂. *Journal of Solid State Chemistry*, 178(6):2128–2132, June 2005. ISSN 0022-4596. doi: 10.1016/j.jssc.2005.04.007. URL <https://www.sciencedirect.com/science/article/pii/S0022459605001581>.
- [43] Marko Topič, Russell M. Geisthardt, and James R. Sites. Performance Limits and Status of Single-Junction Solar Cells With Emphasis on CIGS. *IEEE Journal of Photovoltaics*, 5(1):360–365, January 2015. ISSN 2156-3403. doi: 10.1109/JPHOTOV.2014.2359135. Conference Name: IEEE Journal of Photovoltaics.
- [44] P. K. Paul, T. Jarmar, L. Stolt, A. Rockett, and A. R. Arehart. Role of Ev+0.98 Ev trap in light soaking-induced short circuit current instability in CIGS solar cells. In *2017 IEEE 44th Photovoltaic Specialist Conference (PVSC)*, pages 30–32, June 2017. doi: 10.1109/PVSC.2017.8366748.
- [45] Julia I. Deitz, Pran K. Paul, Rouin Farshchi, Dmitry Poplavskyy, Jeff Bailey, Aaron R. Arehart, David W. McComb, and Tyler J. Grassman. Direct Nanoscale Characterization of Deep Levels in AgCuInGaSe₂ Using Electron Energy-Loss Spectroscopy in the Scanning Transmission Electron Microscope. *Advanced Energy Materials*, 9(35):1901612, 2019. ISSN 1614-6840. doi: 10.1002/aenm.201901612. URL <https://onlinelibrary.wiley.com/doi/abs/10.1002/aenm.201901612>.
- [46] U. Rau and J. H. Werner. Radiative efficiency limits of solar cells with lateral band-gap fluctuations. *Appl. Phys. Lett.*, 84(19):3735–3737, May 2004. ISSN 0003-6951, 1077-3118. doi: 10.1063/1.1737071. URL <http://aip.scitation.org/doi/10.1063/1.1737071>.
- [47] Susanne Siebentritt. What limits the efficiency of chalcopyrite solar cells? *Solar Energy Materials and Solar Cells*, 95(6):1471–1476, June 2011. ISSN 0927-0248. doi: 10.1016/j.solmat.2010.12.014. URL <https://www.sciencedirect.com/science/article/pii/S0927024810006914>.
- [48] Philip Jackson, Roland Wuerz, Dimitrios Hariskos, Erwin Lotter, Wolfram Witte, and Michael Powalla. Effects of heavy alkali elements in Cu(In,Ga)Se₂ solar cells with efficiencies up to 22.6%. *physica status solidi (RRL) – Rapid Research Letters*, 10(8):583–586, 2016. ISSN 1862-6270. doi: 10.1002/pssr.201600199. URL <https://onlinelibrary.wiley.com/doi/abs/10.1002/pssr.201600199>. eprint: <https://onlinelibrary.wiley.com/doi/pdf/10.1002/pssr.201600199>.
- [49] Marc Daniel Heinemann, Tim Kodalle, Charles Hages, Michael Klupsch, Dieter Greiner, Lars Korte, Sergej Levcenco, Thomas Unold, Rutger Schlatmann, and Christian A. Kaufmann. Evaluation of recombination losses in thin film solar cells using an LED sun simulator the effect of RbF post-deposition on CIGS solar cells. *EPJ Photovolt.*, 9:9, 2018. ISSN 2105-0716. doi: 10.1051/epjpv/2018006. URL <https://www.epj-pv.org/articles/epjpv/abs/2018/01/pv180002/pv180002.html>. Publisher: EDP Sciences.
- [50] Fabian Pianezzi, Patrick Reinhard, Adrian Chirilă, Benjamin Bissig, Shiro Nishiwaki, Stephan Buecheler, and Ayodhya N. Tiwari. Unveiling the effects of post-deposition treatment with different alkaline elements on the electronic properties of CIGS thin film solar cells. *Phys. Chem. Chem. Phys.*, 16(19):8843, 2014. ISSN 1463-9076, 1463-9084. doi: 10.1039/c4cp00614c. URL <http://xlink.rsc.org/?DOI=c4cp00614c>.
- [51] T. Walter, R. Herberholz, and H.-W. Schock. Distribution of Defects in Polycrystalline Chalcopyrite Thin Films. *SSP*, 51-52:309–316, May 1996. ISSN 1662-9779. doi: 10.4028/www.scientific.net/SSP.51-52.309. URL <https://www.scientific.net/SSP.51-52.309>.

- [52] U. Rau. Tunneling-enhanced recombination in Cu(In,Ga)Se₂ heterojunction solar cells. *Appl. Phys. Lett.*, 74(1):111–113, December 1998. ISSN 0003-6951. doi: 10.1063/1.122967. URL <https://aip-scitation-org.mines.idm.oclc.org/doi/10.1063/1.122967>. Publisher: American Institute of Physics.
- [53] A. R. Arehart, A. A. Allerman, and S. A. Ringel. Electrical characterization of n-type Al_{0.30}Ga_{0.70}N Schottky diodes. *Journal of Applied Physics*, 109(11):114506, June 2011. ISSN 0021-8979. doi: 10.1063/1.3592284. URL <https://aip.scitation.org/doi/full/10.1063/1.3592284>. Publisher: American Institute of Physics.
- [54] Blood, P. and Orton, J.W. *The Electrical Characterization Of Semiconductors: Majority Carriers And Electron States*, volume 14 of *Techniques of Physics*. Academic Press, August 1992. ISBN 978-0-12-528627-5.
- [55] M Burgelman, P Nollet, and S Degrave. Modelling polycrystalline semiconductor solar cells. *Thin Solid Films*, 361-362:527–532, February 2000. ISSN 0040-6090. doi: 10.1016/S0040-6090(99)00825-1. URL <https://www.sciencedirect.com/science/article/pii/S0040609099008251>.
- [56] Shankar Karki, Pran K. Paul, Grace Rajan, Tasnuva Ashrafee, Krishna Aryal, Puja Pradhan, Robert Warren Collins, Angus Rockett, Tyler J. Grassman, Steven A. Ringel, Aaron R. Arehart, and Sylvain Marsillac. In Situ and Ex Situ Investigations of KF Postdeposition Treatment Effects on CIGS Solar Cells. *IEEE Journal of Photovoltaics*, 7(2):665–669, March 2017. ISSN 2156-3403. doi: 10.1109/JPHOTOV.2016.2637659. Conference Name: IEEE Journal of Photovoltaics.
- [57] Ronald A. Sinton and Andres Cuevas. Contactless determination of current–voltage characteristics and minority-carrier lifetimes in semiconductors from quasi-steady-state photoconductance data. *Appl. Phys. Lett.*, 69(17):2510–2512, October 1996. ISSN 0003-6951, 1077-3118. doi: 10.1063/1.117723. URL <http://aip.scitation.org/doi/10.1063/1.117723>.
- [58] Houqiang Fu and Yuji Zhao. 9 - Efficiency droop in GaInN/GaN LEDs. In JianJang Huang, Hao-Chung Kuo, and Shyh-Chiang Shen, editors, *Nitride Semiconductor Light-Emitting Diodes (LEDs) (Second Edition)*, Woodhead Publishing Series in Electronic and Optical Materials, pages 299–325. Woodhead Publishing, January 2018. ISBN 978-0-08-101942-9. doi: 10.1016/B978-0-08-101942-9.00009-5. URL <https://www.sciencedirect.com/science/article/pii/B9780081019429000095>.
- [59] S. A. Jensen, S. Glynn, A. Kanevce, P. Dippo, J. V. Li, D. H. Levi, and D. Kuciauskas. Beneficial effect of post-deposition treatment in high-efficiency Cu(In,Ga)Se₂ solar cells through reduced potential fluctuations. *Journal of Applied Physics*, 120(6):063106, August 2016. ISSN 0021-8979. doi: 10.1063/1.4960344. URL <https://aip-scitation-org.mines.idm.oclc.org/doi/full/10.1063/1.4960344>. Publisher: American Institute of Physics.
- [60] Polyxeni Tsoulka, Alexandre Crossay, Ludovic Arzel, Sylvie Harel, and Nicolas Barreau. Alternative alkali fluoride post-deposition treatment under elemental sulfur atmosphere for high-efficiency Cu(In,Ga)Se₂-based solar cells. *Progress in Photovoltaics: Research and Applications*, n/a(n/a). ISSN 1099-159X. doi: 10.1002/pip.3508. URL <http://onlinelibrary.wiley.com/doi/abs/10.1002/pip.3508>. eprint: <https://onlinelibrary.wiley.com/doi/pdf/10.1002/pip.3508>.
- [61] Series Resistance | PVEducation, . URL <https://www.pveducation.org/pvcdrom/solar-cell-operation/series-resistance>.
- [62] S. H. Demtsu and J. R. Sites. Effect of back-contact barrier on thin-film CdTe solar cells. *Thin Solid Films*, 510(1):320–324, July 2006. ISSN 0040-6090. doi: 10.1016/j.tsf.2006.01.004. URL <https://www.sciencedirect.com/science/article/pii/S0040609006000472>.

- [63] S. A. Ringel, A. W. Smith, M. H. MacDougal, and A. Rohatgi. The effects of CdCl_2 on the electronic properties of molecular-beam epitaxially grown CdTe/CdS heterojunction solar cells. *Journal of Applied Physics*, 70(2):881–889, July 1991. ISSN 0021-8979, 1089-7550. doi: 10.1063/1.349652. URL <http://aip.scitation.org/doi/10.1063/1.349652>.
- [64] U. Malm, J. Malmström, C. Platzter-Björkman, and L. Stolt. Determination of dominant recombination paths in Cu(In,Ga)Se_2 thin-film solar cells with ALD- ZnO buffer layers. *Thin Solid Films*, 480-481:208–212, June 2005. ISSN 0040-6090. doi: 10.1016/j.tsf.2004.11.008. URL <https://www.sciencedirect.com/science/article/pii/S0040609004015603>.
- [65] Jürgen H. Werner, Julian Mattheis, and Uwe Rau. Efficiency limitations of polycrystalline thin film solar cells: case of Cu(In,Ga)Se_2 . *Thin Solid Films*, 480-481:399–409, June 2005. ISSN 0040-6090. doi: 10.1016/j.tsf.2004.11.052. URL <https://www.sciencedirect.com/science/article/pii/S0040609004016128>.
- [66] Tim Helder, Ana Kanevce, Andreas Bauer, Mario Zinßer, Stefan Paetel, Theresa Magorian Friedlmeier, and Michael Powalla. DLTS investigations on CIGS solar cells from an inline co-evaporation system with RbF post-deposition treatment. *EPJ Photovolt.*, 13:7, 2022. ISSN 2105-0716. doi: 10.1051/epjpv/2022003. URL <https://www.epj-pv.org/10.1051/epjpv/2022003>.
- [67] Steven Hegedus, Darshini Desai, and Chris Thompson. Voltage dependent photocurrent collection in CdTe/CdS solar cells. *Progress in Photovoltaics: Research and Applications*, 15(7):587–602, 2007. ISSN 1099-159X. doi: 10.1002/pip.767. URL <https://onlinelibrary.wiley.com/doi/abs/10.1002/pip.767>. eprint: <https://onlinelibrary.wiley.com/doi/pdf/10.1002/pip.767>.
- [68] X. X. Liu and J. R. Sites. Solar-cell collection efficiency and its variation with voltage. *Journal of Applied Physics*, 75(1):577–581, January 1994. ISSN 0021-8979, 1089-7550. doi: 10.1063/1.355842. URL <http://aip.scitation.org/doi/10.1063/1.355842>.
- [69] M. Eron and A. Rothwarf. Effects of a voltage-dependent light-generated current on solar cell measurements: $\text{CuInSe}_2/\text{Cd(Zn)S}$. *Appl. Phys. Lett.*, 44(1):131–133, January 1984. ISSN 0003-6951, 1077-3118. doi: 10.1063/1.94577. URL <http://aip.scitation.org/doi/10.1063/1.94577>.
- [70] Dmitry Poplavskyy, Jeff Bailey, Rouin Farshchi, and David Spaulding. Impact of Ga/III Profile on Voltage-dependent Collection Losses in CIGS Solar Cells. In *2017 IEEE 44th Photovoltaic Specialist Conference (PVSC)*, pages 1686–1690, June 2017. doi: 10.1109/PVSC.2017.8366715.
- [71] Chien-Yao Huang, Wen-Chin Lee, and Albert Lin. A flatter gallium profile for high-efficiency Cu(In,Ga)(Se,S)_2 solar cell and improved robustness against sulfur-gradient variation. *Journal of Applied Physics*, 120(9):094502, September 2016. ISSN 0021-8979, 1089-7550. doi: 10.1063/1.4961605. URL <http://aip.scitation.org/doi/10.1063/1.4961605>.
- [72] Alban Lafuente-Sampietro, Jingdong Chen, Shenghao Wang, Xia Hao, Muhammad Monirul Islam, Takuya Kato, Hiroki Sugimoto, Katsuhiko Akimoto, and Takeaki Sakurai. Wavelength-dependent J–V characteristics of $\text{CuIn}_{1-x}\text{Ga}_x(\text{S,Se})_2$ solar cells and carrier recombination. *Appl. Phys. Express*, 12(6):061001, May 2019. ISSN 1882-0786. doi: 10.7567/1882-0786/ab1ad8. URL <https://dx.doi.org/10.7567/1882-0786/ab1ad8>. Publisher: IOP Publishing.
- [73] John Emsley. *The Elements*. Clarendon Press, 3rd edition edition, 1998. ISBN 0-19-855819-8.
- [74] Secondary Ion Mass Spectrometry Theory Tutorial, . URL <https://pprco.tripod.com/SIMS/Theory.htm>.

- [75] Pierre J. Verlinden. Chapter I-4-C - High-Efficiency Back-Contact Silicon Solar Cells for One-Sun and Concentrator Applications. In Soteris A. Kalogirou, editor, *McEvoy's Handbook of Photovoltaics (Third Edition)*, pages 473–499. Academic Press, January 2018. ISBN 978-0-12-809921-6. doi: 10.1016/B978-0-12-809921-6.00013-6. URL <https://www.sciencedirect.com/science/article/pii/B9780128099216000136>.
- [76] J.D. Cohen, J.T. Heath, and W.N. Shafarman. Photocapacitance Spectroscopy in Copper Indium Diselenide Alloys. In *Wide-Gap Chalcopyrites*. Springer Berlin, Heidelberg, 2006. ISBN 978-3-540-31293-2.
- [77] Xiaobo Hu, Takeaki Sakurai, Akimasa Yamada, Shogo Ishizuka, Sigeru Niki, and Katsuhiro Akimoto. Investigation of deep-level defects in Cu(In,Ga)Se₂ thin films by a steady-state photocapacitance method. *J. Appl. Phys.*, page 6, 2014.
- [78] T. Sakurai, H. Uehigashi, M. M. Islam, T. Miyazaki, S. Ishizuka, K. Sakurai, A. Yamada, K. Matsubara, S. Niki, and K. Akimoto. Temperature dependence of photocapacitance spectrum of CIGS thin-film solar cell. *Thin Solid Films*, 517(7):2403–2406, February 2009. ISSN 0040-6090. doi: 10.1016/j.tsf.2008.11.051. URL <https://www.sciencedirect.com/science/article/pii/S0040609008013837>.
- [79] Peter T. Erslev, Jin Woo Lee, William N. Shafarman, and J. David Cohen. The influence of Na on metastable defect kinetics in CIGS materials. *Thin Solid Films*, 517(7):2277–2281, February 2009. ISSN 0040-6090. doi: 10.1016/j.tsf.2008.10.140. URL <http://www.sciencedirect.com/science/article/pii/S0040609008013497>.
- [80] J. T. Heath, J. D. Cohen, W. N. Shafarman, D. X. Liao, and A. A. Rockett. Effect of Ga content on defect states in CuIn_{1-x}Ga_xSe₂ photovoltaic devices. *Appl. Phys. Lett.*, 80(24):4540–4542, June 2002. ISSN 0003-6951, 1077-3118. doi: 10.1063/1.1485301. URL <http://aip.scitation.org/doi/10.1063/1.1485301>.

APPENDIX A
AUTOMATED JVT ANALYSIS CODE

The following github link provides a Python code for automated processing of JVT data as outlined in Chapter 5.

<https://github.com/jakewands/Automated-JVT-Analysis>

APPENDIX B

COPYRIGHT PERMISSIONS

B.1 Figure 1.1 Copyright Permission

Figure 1.1 was reprinted from the U.S. Energy Information Administration's "International Energy Outlook 2021" report. The copyright policy of the U.S. EIA is as follows:

Public domain and use of EIA content: U.S. government publications are in the public domain and are not subject to copyright protection. You may use and/or distribute any of our data, files, databases, reports, graphs, charts, and other information products that are on our website or that you receive through our email distribution service. However, if you use or reproduce any of our information products, you should use an acknowledgment, which includes the publication date, such as: "Source: U.S. Energy Information Administration (Oct 2008)."

B.2 Figure 1.2 Copyright Permission

Figure 1.2 was reprinted from the International Panel on Climate Change's Working Group III contribution to the Sixth Assessment Report report. The copyright policy of the IPCC is as follows:

Unless otherwise stated, the information available on this website, including text, logos, graphics, maps, images and electronic downloads is the property of the IPCC and is protected by intellectual property laws.

You may freely download and copy the material contained on this website for your personal, non-commercial use, without any right to resell or redistribute it or to compile or create derivative works there from, subject to more specific restrictions that may apply to specific materials.

For such personal, non-commercial usages, reproduction of limited number of figures or short excerpts of IPCC material is authorized free of charge and without formal written permission provided that the original source is properly acknowledged, with mention of the complete name of the report, the publisher and the numbering of the page(s) or the figure(s). Permission can only be granted to use the material exactly as it is in the report. Please be aware that figures cannot be altered in any way, including the full caption. For media reporting purposes, it is sufficient to cite the source material as long as the appropriate credit is given with use of the original graphic or figure and the IPCC is advised. In line with established Internet usage, any external website may provide a hyperlink to the IPCC website or to any of its pages without requesting permission.

For any other use, permission is required. To obtain permission, please email a scanned copy of a letter on official letterhead addressed to the Secretary of the IPCC with all relevant details. Responses may take

up to four weeks. Please consider this timing when submitting your request. All communications by mail should be addressed to:

IPCC Secretariat World Meteorological Organization 7bis Avenue de la Paix, P.O. Box No. 2300
CH-1211 Geneva 2, Switzerland

All e-mail communications should be addressed to ipcc-sec@wmo.int.

B.3 Chapter 4 Copyright Permission

The IEEE does not require individuals working on a thesis to obtain a formal reuse license, however, you may print out this statement to be used as a permission grant:

Requirements to be followed when using any portion (e.g., figure, graph, table, or textual material) of an IEEE copyrighted paper in a thesis:

1) In the case of textual material (e.g., using short quotes or referring to the work within these papers) users must give full credit to the original source (author, paper, publication) followed by the IEEE copyright line ©2011 IEEE. 2) In the case of illustrations or tabular material, we require that the copyright line ©2022 IEEE appear prominently with each reprinted figure and/or table. 3) If a substantial portion of the original paper is to be used, and if you are not the senior author, also obtain the senior author's approval.

Requirements to be followed when using an entire IEEE copyrighted paper in a thesis:

1) The following IEEE copyright/ credit notice should be placed prominently in the references: ©2022 IEEE. Reprinted, with permission, from J. Wands, A. Kanevce, A. Bothwell, M. Miller, S. Paetel, A. Arehart, A. Rockett, Evaluating Recombination Mechanisms in RbF Treated Cu(In_xGa_{1-x})Se₂ Solar Cells, IEEE Journal of Photovoltaics, Nov. 2022. 2) Only the accepted version of an IEEE copyrighted paper can be used when posting the paper or your thesis on-line. 3) In placing the thesis on the author's university website, please display the following message in a prominent place on the website: In reference to IEEE copyrighted material which is used with permission in this thesis, the IEEE does not endorse any of Colorado School of Mines' products or services. Internal or personal use of this material is permitted. If interested in reprinting/republishing IEEE copyrighted material for advertising or promotional purposes or for creating new collective works for resale or redistribution, please go to http://www.ieee.org/publications_standards/publications/rights/rightslink.html to learn how to obtain a License from RightsL

If applicable, University Microfilms and/or ProQuest Library, or the Archives of Canada may supply single copies of the dissertation.

B.4 Chapter 5 and 6 Copyright Permission

Permission was requested and granted from the co-authors for the submitted publications "Stability of Cu(In_xGa_{1-x})Se₂ Solar Cells Utilizing RbF Post-Deposition Treatment Under a Sulfur Atmosphere" and "Voltage-Dependent Collection Efficiency Losses in RbF Treated Cu(In_xGa_{1-x})Se₂" which have not yet been accepted or rejected from Advanced Energy and Sustainability Research respectively and Progress in Photovoltaics: Research respectively. Proof of approval is available upon request. The following email was sent to all co-authors:

Hello Co-Authors,

I am also planning on including the papers "Stability of Cu(In_xGa_{1-x})Se₂ Solar Cells Utilizing RbF Post-Deposition Treatment Under a Sulfur Atmosphere" submitted to Advanced Energy and Sustainability Research and "Voltage-Dependent Collection Efficiency Losses in RbF Treated Cu(In_xGa_{1-x})Se₂" submitted to Progress in Photovoltaics: Research and Applications as chapters in my thesis. I need to request copyright permission from the authors in order to include them. If you could reply "I agree" to this email I would greatly appreciate it.

Thanks again, Jake Wands